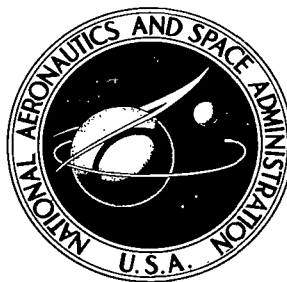


NASA TECHNICAL  
TRANSLATION



NASA TT F-688

2.1

NASA TT F-688

LOAN COPY: RET  
AFWL (DO  
KIRTLAND AFB

0069177



TECH LIBRARY KAFB, NM

# MORPHOLOGY OF THE QUIET AND DISTURBED IONOSPHERE

*Edited by M. P. Rudina*

*"Nauka" Press of Kazakh SSR*

*Alma Ata, 1970*

NATIONAL AERONAUTICS AND SPACE ADMINISTRATION • WASHINGTON, D. C. • MAY 1972



0069177

# MORPHOLOGY OF THE QUIET AND DISTURBED IONOSPHERE

Edited by M. P. Rudina

Translation of "Morfologiya Spokoynoy i Vozmushchennoy Ionosfery"  
"Nauka" Press of Kazakh SSR, Alma Ata, 1970

NATIONAL AERONAUTICS AND SPACE ADMINISTRATION

---

For sale by the National Technical Information Service, Springfield, Virginia 22151  
\$3.00



## TABLE OF CONTENTS

M.P. Rudina and N.F. Solonitsyna, The State of the Ionosphere Above Alma-Ata. . . . .	1
V.I. Drobzhev, On the Selection of a Vertical Base in the Ionosphere. . . . .	7
V.I. Drobzhev, Influence of Vertical Drift of Small-Scale Ionization Inhomogeneities on the Diurnal Variation of $f_0F_2$	13
M.P. Rudina and N.F. Solonitsyna, Ionospheric Magnetic Phenomena Associated with Proton Flares. . . . .	17
V.I. Drobzhev, Parameters of Small-Scale Ionization Inhomogeneities in the F-Region of the Ionosphere. . . . .	23
T.K. Yakovets, Radioastronomical Measurement of Absorption . .	30
M.P. Rudina and P.Ye. Kozina, The Ionosphere Above Alma-Ata During a Solar Eclipse. . . . .	35
V.M. Krasnov and A.F. Yakovets, Apparatus for Investigation of the Amplitude-Frequency Response of the Ionospheric-Scattering Channel. . . . .	39
A.F. Yakovets, A Method of Investigating the Phase-Response Characteristic of the Ionospheric-Scattering Communications Channel . . . . .	46
Ya.F. Ashkaliyev and V.I. Bocharov, Radio-Wave Propagation at Frequencies Exceeding MUF-F2 in the Shortwave Band. . . . .	55
Ya.F. Ashkaliyev and V.I. Bocharov, Occupancy of the Radio-Frequency Spectrum in the 16-23 MHz Band. . . . .	60
Ya.F. Ashkaliyev, Receiving-Antenna Installation for Ionospheric Scattering Links. . . . .	65
E.L. Afraymovich, G.M. Kudelin, and G.M. Pelenitsyn, Input of Information Recorded on Magnetic Tape into the BESM-3M Computer . . . . .	69
I.D. Kozin, Cosmic-Ray Variations During "PCA"-Type Absorption	74
L.I. Dorman and I.A. Pimenov, Statistical Accuracy of Cosmic Radiation Neutron Component Recorders . . . . .	78
V.N. Pogrebnoy and M.N. Fatkullin, Estimates of the Electric Fields in the Lower Ionosphere above the Magnetic Equator .	82
V.N. Pogrebnoy, G.I. Gordiyenko, and B.T. Zhumabayev, On the Possibility of Explaining Features of the Latitude Variations of $S_q(H)$ and $S_q(Z)$ in the Equatorial Region by Electrical Modelling. . . . .	90

I.A. Pimenov, On the Resolution of the Standard Algorithm for Cosmic-Ray Stations . . . . .	95
N.A. Korinevskaya, Results of Measurement of Radio-Wave Absorption in the Ionosphere by the AI Method . . . . .	99
I.D. Kozin, Variations of Cosmic Rays Associated with Chromo- spheric Flares on the Sun . . . . .	113

ANNOTATION

/2

This collection reports for the most part on work done by the staff of the Ionosphere Sector of the Academy of Sciences of the Kazakh SSR during 1964-1967.

The articles examine data from ionospheric studies made in Kazakhstan during the International Quiet Sun Year (IQSY) and describe equipment developed by the Sector for study of the mechanism of ionospheric radio-wave propagation and introduction of automation and computer elements into analysis of the experimental information.

A new method is proposed for analysis of cosmic-ray variation data.

Editorial Staff:

M.P. Rudina (Editor-in-Chief)

E.L. Afraymovich

B.V. Troitskiy

I.D. Kozin (Chief Secretary)

## THE STATE OF THE IONOSPHERE ABOVE ALMA-ATA

/3\*

M.P. Rudina and N.F. Solonitsyna

ABSTRACT: The paper describes the basic patterns observed in the behavior of the critical frequencies ( $f_0$ ) and minimum effective (virtual) heights ( $h'$ ) of the ionosphere's reflecting E, F1, and F2 layers according to ionospheric-recorder measurements of  $f_0 = \phi(h')$  over the period from 1943 to 1967. The variations of  $f_0$  and  $h'$  are compared with the relative sunspot numbers (W) and the flux of the sun's radio emission ( $\Phi$ ) at 10.7 cm. With 3 illustrations and 4 source citations.

State of the ionosphere at noon. Critical frequencies. Ionospheric data acquired over the long term are of great importance for investigation of processes that take place in the ionosphere, compilation of long-term frequency forecasts, and ensuring uninterrupted communications in the shortwave band. For this reason, the results of measurements made at the Alma-Ata ionospheric station, which cover more than two cycles of solar activity, are of great interest.

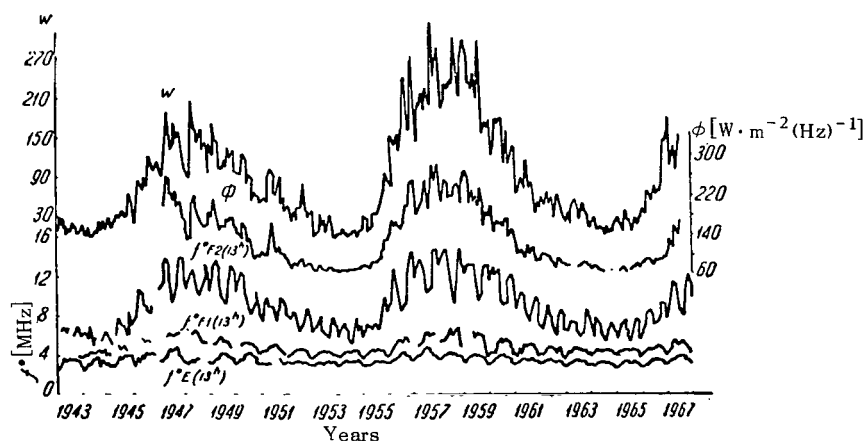


Figure 1. Critical Frequencies  $f_0E$ ,  $f_0F1$ , and  $f_0F2$  in Megahertz at 13 Hours ( $75^\circ E$  Time), Sunspot Numbers (W), and Flux of Solar Radio Emission ( $\Phi$ ) at 10.7 cm.

\*Numbers in the margin indicate pagination in the foreign text.

The behavior of the critical frequencies ( $f_0$ ) and virtual heights ( $h'$ ) of the E, F1, and F2 layers of the ionosphere was compared with solar activity expressed by the relative sunspot number ( $W$ ) [1, 2] and the sun's radio emission flux at 10.7 cm ( $\Phi$ ) (Figs. 1, 2, and 3). The monthly noon and midnight median values were used for analysis, since they are most representative of the quiet state of the ionosphere and the critical-frequency and virtual-height values. The noon and midnight times (75°E time) were selected because the processes taking place in the ionosphere are considered to be steadier at these times of day.

/4

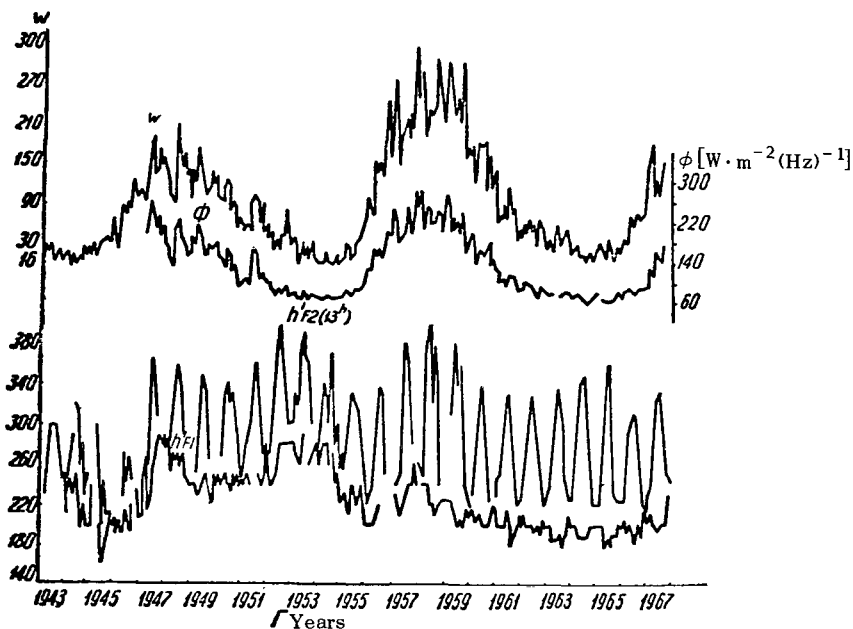


Figure 2. Virtual Heights  $h'F1$  and  $h'F2$  at 13 Hours in Kilometers (75°E Time), ( $W$ ), and ( $\Phi$ ).

The critical frequencies (Fig. 1) varied in conformity to solar activity ( $W$  and  $\Phi$ ). Two eleven-year cycles, three minima (1943-1944, 1953-1954, 1964-1965) and two maxima (1947-1948-1949 and 1957-1958-1959) are clearly evident on the  $f_0E$ ,  $f_0F1$ , and  $f_0F2$  curves. The amplitude of the frequency fluctuations increased, especially for the F2 layer, with rising solar activity. It can be seen from the change in the sunspot numbers that the nineteenth cycle was significantly more intense than the eighteenth. While the monthly average sunspot value was 210 in the eighteenth cycle, it was 330 in the nineteenth. The variation of the radio emission flux  $\Phi_{10.7 \text{ cm}}$  and the critical frequencies from cycle to cycle was less distinct. To judge from the 1966-1967 ascending branch, the twentieth cycle promises to be less

/5



intense than the nineteenth. The patterns brought out here indicate a probable increase in the ionization density at the layer maximum,  $N_m \approx (f_o)^2$ , with increasing ionizing radiation.

A trend to limitation of the critical frequencies and, consequently, limitation of the ionization rise is discerned during years of enhanced solar activity [3]. The median values of  $f_oF2$  were also limited in the years of the nineteenth-cycle minimum. A seasonal variation can be traced in the cyclical variation of the critical frequencies: the frequency values of the E and F1 layers are highest in summer and lowest in winter. The probability of appearance of the F1 layer increases with declining solar activity. In the years of the minimum, the F-region was stratified into F1- and F2-layers above Alma-Ata all year round. This is illustrated in Fig. 1 by the continuous  $f_oF1$  curve. During years of high activity, the F1-layer was observed for the most part only in summer. In the F2-layer, the critical-frequency maxima occur in the spring and autumn months (March, October), one minimum in summer (July), and another much weaker one in winter (December-January). The amplitude of the seasonal critical-frequency variation increases with W. Thus, the values of  $f_oE$  varied from 4.8 to 2.8 MHz in the eighteenth cycle and from 4.8 to 2.6 MHz in the nineteenth; those of  $f_oF1$  varied from 6.7 to 3.6 MHz in the eighteenth and from 7 to 3.6 MHz in the nineteenth. Ionization intensity depends most conspicuously on solar activity in the F2-layer (Fig. 1). The critical frequencies of this layer varied from 14 to 5.3 MHz in the eighteenth cycle and from 14.8 to 5.3 MHz in the nineteenth.

Minimum virtual heights. For the heights, the seasonal variation can be traced easily and the cycle variation somewhat less easily. The minimum effective height of the F1-layer depends on solar activity to a lesser degree than the height of the F2-layer (Fig. 2). Over somewhat more than two solar-activity cycles, the lowest values of  $h'F1$  were reported in 1945 ( $h'F = 160$  km). The heights not only of the F1-layer, but also of the F2-layer increased from 1947 to 1954. This may have been due to some extent to the screening effect of the sporadic E-layer. In years of the minimum,  $h'F1$  varied for the most part through  $\pm 20$  km. During years of the maximum, the variations of the F1-layer height reached  $\pm 45$  km. Its height increased in winter and decreased in summer.

Two minima and two maxima are observed in the variations of the F2-layer heights in each solar-activity cycle (Fig. 2): minima on the ascending branches (1945-1946, 1955-1956) and descending (1949-1950, 1961-1962) branches and maxima of the height  $h'F2$  at higher and lower solar activities. /6

The fluctuations observed on the curve of the F2-layer height in the eighteenth cycle are wider than those of the nineteenth. Thus,  $h'F2 = 320$  km in 1944, and 200 km in 1945, but in

1947,  $h'F_2$  fell from 370 to 250 km and remained at this level until 1954. At this time, the winter values of  $h'F_2$  began a progressive decrease, reaching 220 km by 1965. Like those of the  $F_1$ -layer, the heights of the  $F_2$ -layer showed a general rise during the eighteenth cycle from 1947 through 1954. The upper limit of the  $F_2$ -layer height curve behaved somewhat differently. From 1947 through 1950,  $h'F_2$  fell to 340 km, but from 1950 to 1952, the upper level of the height fluctuation rose to 390 km. Then the upper limit of the  $F_2$ -layer height curve began smooth cyclical variations (summer values of  $h'F_2$ ). The greatest heights of the  $F_2$ -layer were observed in 1952 and 1958.

Greater  $F_2$ -layer heights were observed when the F-region was clearly separated into  $F_1$ - and  $F_2$ -layers. If the ionization minimum of the  $F_2$ -layer is registered in June-July, greater heights are also generally recorded in June-July. It was as though an initial broadening of the layer was followed by a decline in ionization. The  $F_2$ -layer heights were smallest in November-December. It is evident from the trend of the  $F_1$ - and  $F_2$ -layer heights that the height of the  $F_2$ -layer decreased in November and December, while that of  $F_1$  rose. It was as though the F-region had been compressed. Density increased as a result. While the lower boundary of the  $F_2$ -layer heights rose during the maximum in the eighteenth cycle, the lower boundary (winter values) of the  $F_2$ -layer heights remained at the same level during the nineteenth cycle. Thus, the winter  $F_2$ -layer occurred at the 220-km level. While no cyclical pattern was observed for the winter values of the  $F_2$ -layer heights, such a pattern did emerge for the summer values in the nineteenth cycle (Fig. 2).

On analyzing the behavior of the lower boundaries of the ionosphere's  $F_2$ - and  $F_1$ -layers in the eighteenth and nineteenth solar-activity cycles, we note that the thickness of the  $F_1$ -region was much greater during the strong nineteenth cycle than in the eighteenth. It was as though the entire F-region rose at the maximum of the nineteenth cycle and descended at its minimum. The lower boundary of the region occurred at the 180-km level. The F-region descended on the descending part of the solar-activity branch (1960-1962) and rose again during the period of the maximum. Both descent and contraction were observed in 1966-1967. The stronger radiation during the nineteenth cycle as compared with the preceding one naturally increased the temperature of the gas and this, in turn, affected the physical parameters of the ionosphere, including diffusion processes. It has been shown that diffusion has a strong influence on the over-all electron-concentration balance at the maximum of the ionospheric layer [4].

State of the ionosphere at midnight. The nighttime state of the ionosphere can be judged from the trend of the  $f_oF_2$  and  $h'F$  curves (Fig. 3). The ionization varies in the same way at night as it does at midday (in accordance with solar activity). The strongest and weakest ionizations coincide with the solar-activity maxima and minima. Thus, in contrast to the eighteenth cycle,

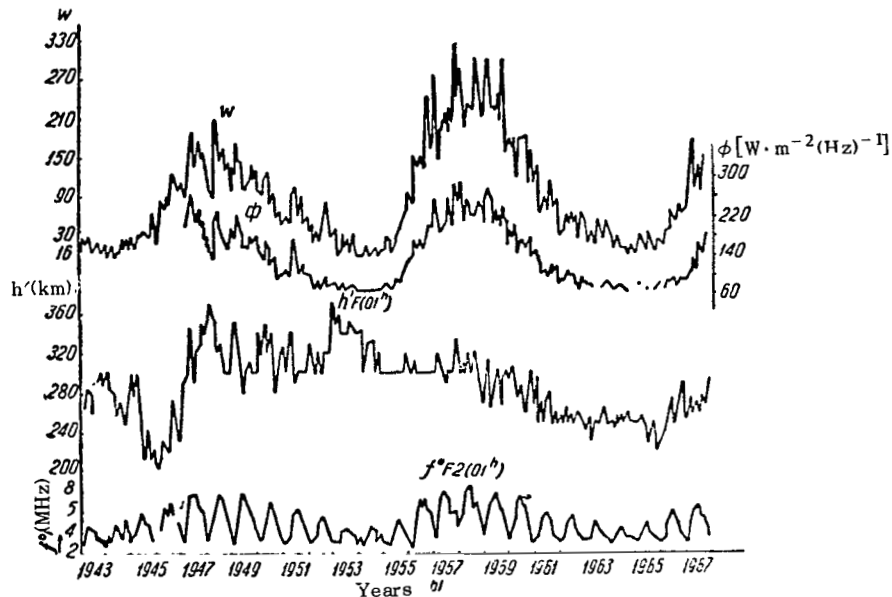


Figure 3. Critical Frequencies  $f_oE2$  in Megahertz and Effective Heights in Kilometers at 01<sup>h</sup> (75°E Time), (W), and ( $\Phi$ ).

the lower frequency limit rose by approximately 2 MHz at the maximum of the nineteenth cycle, while the upper limit reached the eighteenth-cycle level. A rise in the lower critical-frequency level (winter values) is beginning again on the ascending branch of the twentieth solar-activity cycle. A cyclical relationship emerges for the summer values of  $f_oF2$  — something that cannot be said of the winter  $f_oF2$ . The amplitude of the frequency fluctuations during the maximum was approximately  $\pm 3$ ,  $\pm 4$  MHz, but  $\pm 1$ ,  $\pm 2$  MHz during the minimum. In addition to the eleven-year cycle, the seasonal variation is distinctly outlined. The ionization maximum is observed in the summer and the minimum in winter.

The curve of midnight F-region heights (Fig. 3) shows clearly the sharp variations of  $h'F$  during the eighteenth cycle and the smoother ones during the nineteenth. No cyclical relationship is detected. During the eighteenth cycle,  $h'F$  descended from 300 to 200 km from 1944 to 1956. The height of the F-layer rose from 200 to 370 km from 1945 to 1948 and then, during this same year, dropped to 290 km, where it remained until 1958. A brief rise was observed from 1952 through 1953, from 290 to 360 km. In 1958, the height of the region began a progressive decrease, reaching 220 km in 1965; in 1966 and 1967, it rose again slowly. The seasonal variation of the region's nighttime heights was faintly discernible; it was subject to numerous fluctuations. As a rule,

however, a decrease in the heights is observed in summer and an increase in winter.

To account for the patterns traced in the behavior of the critical frequencies and especially in that of the heights of the reflecting ionospheric layers, it must be assumed that the solar cycles differ in respect to the nature of the radiation from various regions on the sun. Like the radio flux at 10.7 cm, the relative sunspot-number index cannot fully reflect the true factors that influence the ionized states of the ionospheric layers. Thus, the decrease in the number of sunspots at the end of 1947 and beginning of 1948 may have been responsible for the disturbance of the seasonal relationships in the variation of the F2-layer critical frequencies and for the disappearance of the daytime spring maximum of  $f_oF_2$ . The questions as to the decreased summer ionization and the causes of ionization limiting during years of high W and  $\Phi$  still remain unclarified. It has been established in recent years that the number and nature of magnetic ionospheric disturbances are different in different solar-activity cycles. Solar flares vary in energy and affect the state of the ionosphere differently. It is therefore necessary to continue study of the sun-geomagnetic field-ionosphere interaction.

#### REFERENCES

/9

1. In: "Solnechnyye dannyye" (Solar Data), Moscow, "Nauka," 1964-1967.
2. In: "Kosmicheskiye dannyye" (Cosmic Data), Moscow, "Nauka," 1953-1963.
3. Likhachev, A.N. The Ionization of the F2-Layer as a Function of Solar Energy Influx to the Atmosphere. "Geomagnetizm i aeronomiya," 1962, No. 3, 2.
4. Polyakov, V.M. Diffusion of Charged Particles in the F-Region of the Ionosphere in Middle Latitudes. "Geomagnetizm i aeronomiya," 1966, No. 2, 6.

ON THE SELECTION OF A VERTICAL BASE IN THE  
IONOSPHERE

/10

V.I. Drobzhev

ABSTRACT: The problem of selecting a vertical base in the ionosphere that permits registration of vertical motions of small-scale ionization inhomogeneities of the ionosphere's F-region is discussed. The accuracy of calculation of the vertical drift-velocity component is estimated. With 2 illustrations and 6 source citations.

It is known that the distance between receiving observation points in space-diversity reception determines system resolution, i.e., the spectrum of the inhomogeneities under study. For example, a ground base from 100 to 1000 m in length is used in study of the horizontal motions of small-scale ionization inhomogeneities (in the hundreds of meters) [1]. Clearly, study of the vertical drift of this inhomogeneity spectrum requires a measurement base of approximately the same order in the ionosphere.

Just as the side length of the measurement triangle (the base) must not greatly exceed the spatial-correlation radius of the diffraction pattern in space-diversity reception, the vertical base must not greatly exceed the radius of frequency correlation between signals at different frequencies. This would result in weak similarity between the traces of a fluctuating signal obtained simultaneously from different heights in the F2-region.

Since the literature offers no theoretical estimates with a bearing on selection of vertical baselength, this problem has been solved by experiment by adjusting the difference between the simultaneously radiated frequencies (with consideration of the fact that radio waves of different lengths are reflected from different layers in the ionosphere) [6].

Figure 1 presents a typical specimen recording showing the amplitude fading of a signal received simultaneously at different frequencies. The photographic record shows the form similarity of the  $R(t)$  fading curves (a similar fading-curve form is obtained on registration of horizontal drifts). Corresponding maxima are shifted with respect to one another by the vertical drift of small-scale inhomogeneities. Analysis of the records indicated that a stable time shift is observed between the  $R(t)$  curves obtained simultaneously from different heights in the ionospheric

/11



Figure 1. Amplitude Fading of Signals Received Simultaneously at Different Frequencies. The Uppermost Trace Corresponds to  $f_1$  (Minimum Frequency), the Second to  $f_2$ , etc. Film Advance Speed 50 mm/min.

F2-region at a frequency diversity of 2 to 60 kHz. If the diversity  $\Delta f > 60$  kHz, there is usually either complete decorrelation of the  $R(t)$  curves or excessively slow fading, evidently due to vertical motion of large-scale inhomogeneities. At the same time, there is a lower limit to the diversity  $\Delta f$ , because the time shift  $\tau_{ij}$  is of the order of 0.1-0.15 second when  $\Delta f = 2-5$  kHz, i.e., within the limits of reading error. Thus, a vertical base that permits registration of the vertical drift of small-scale inhomogeneities is obtained when the simultaneously radiated frequencies are separated by 5 to 60 kHz.

The direction of the vertical drift is determined as follows. If the amplitude maxima or minima corresponding to the  $R(t)$  curve for frequency  $f_1$  lag the amplitude maxima or minima of the  $R(t)$  curves of frequencies  $f_2$ ,  $f_3$ , and  $f_4$ , drift is upward; conversely, if they lead them, it is downward with respect to the plane of the horizon.

To calculate  $V_v$ , it is necessary to know the relative difference between the true heights (vertical base) that corresponds to the simultaneously radiated frequencies. The true heights were computed on a Minsk 1 electronic computer by the method described in [2]. Here the experimental height-frequency curve ( $h'f$ ) was broken up into a series of frequency intervals ( $\Delta f$ ) with  $\Delta f$  at 0.1 MHz, i.e., the true heights were computed at 0.1-MHz intervals. By way of illustration, let us examine the true-height interval corresponding to the frequency difference  $\Delta f = 0.2$  MHz.

It was found that a relative difference  $\Delta h$  from 2 to 10 km corresponds to  $\Delta f = 0.2$  MHz, with a most probable value of 5-6 km. In view of the fact that the work was done simultaneously with pulses of four different frequencies, for the most part with a 10-kHz shift, it is easily seen that a most probable vertical-base value of 0.25-0.3 km corresponds to a  $\Delta f$  of 10 kHz, 0.5-0.6 km to 20 kHz, 0.75-0.9 km to 30 kHz, and 1-1.2 km to 40 kHz. /12

The distribution of the vertical-base values for various seasons in 1965-1966 indicated that for times around the equinox (September 1965 and September and March 1966), the  $\Delta h$  corresponding to  $\Delta f = 20$  kHz varies from 100 to 1100 m. The most probable value of  $\Delta h$  is 400-500 m; for winter (January-February 1966), the most probable vertical-base value is 500-700 m, and for summer (May, June, July 1966), 400-600 m. The vertical base increases by a factor of 1.5 to 2, respectively, for diversities of 30 and 40 kHz.

The most probable values of the time shift are 1.5-2 sec for  $\Delta f = 20$  kHz and 3 sec for 30 kHz. Thus, the most probable value of the vertical drift, defined as  $V_v = \Delta h / \tau_{ij}$ , was found to be approximately 200-300 m/sec. This value of  $V_v$  is virtual, since it is assumed that drift takes place in the vertical plane, just as motion in the horizontal plane is assumed in calculation of the horizontal drift (fading-similarity method) [3].

The accuracy of calculation of the vertical drift-velocity component, which depends primarily on proper determination of the vertical base, and, consequently, the accuracy of the true-height calculation may be questioned. Here, accidental errors may arise out of the following factors: the subjectiveness of the reading taken in compiling the ionospheric records; the pulsed ionospheric-sounding method; instability of the ionospheric sounder's height-marker generator; the nonzero dimensions of the spot on the cathode-ray tube, etc. With consideration of these errors and the details of  $N(h)$ -profile processing in our experiment, the error of vertical-base measurement determined by the formula  $\Delta \epsilon = \pm K \sqrt{\epsilon \Delta^2}$  was  $\pm 3$  km ( $K = 1$ ). On this basis, the most probable value of  $\Delta h = 6$  km corresponding to the frequency interval  $\Delta f = 0.2$  MHz will be  $\pm 3$  km, or the most probable vertical-base value (for  $\Delta f = 20$  kHz) will be  $500-600 \pm 300$  m, i.e., the accuracy of vertical-base calculation in this case is approximately 50%. It is readily noted that the accuracy of calculation of  $\Delta h$  from the segment of the  $h'(f)$  curve corresponding to  $\Delta f = 0.3$  MHz increases to 30%, or to 20-25% for  $\Delta f = 0.4$  MHz. /13

Thus, the vertical component of drift rate can be determined by this method accurate to 20-30%. The principal use made of these results was in construction of the diurnal variation of the magnitude and direction of  $V_v$ , in which no fewer than 20 values of  $V_v$  were averaged for each hour of the day. We know from the theory of accidental errors that in this case the root-mean-square error of the average (independent measurements) is reduced by a factor of  $\sqrt{n}$ , where  $n$  is the number of measurements. Consequently, the accuracy of calculation of  $V_v$  for each hour is increased to 10-15%. If  $K = 2$ , the error of calculation of  $h$  equals  $\pm 6$  km.

A number of other methodological questions arise in study of the vertical drift of small-scale ionization inhomogeneities: whether the vertical base remains constant over the time of drift registration, and the extent to which representation of the true-height segment corresponding to  $\Delta f = 0.3$  MHz by a line segment is justified.

Actually, the ionospheric records from which the base is determined are taken at 15-minute intervals (the time to record a high-frequency characteristic is 20 sec). On the other hand, a drift session runs to 5-10 minutes, with the beginning or end of the session generally coinciding with ionospheric recording. The questions naturally arise as to whether the base remains constant throughout the session and, if it does not, the amount by which it changes. This was investigated on apparatus with which the vertical base could be determined by a phase method. The phase method of investigating the altitude distribution of electron concentration (in accordance with the true-height calculation) that was proposed in [5] and developed in [4] is characterized by high relative height accuracy (of the order of the wavelength of the working frequency), and this makes it possible to evaluate the constancy of  $dh(t)/dt$  as a function of the time of the drift-registration session. It was shown experimentally in [4] that  $dq(h)/dt$  ( $q$  is the phase of the signal reflected from the ionosphere) can be assumed constant to within 5-10% over the time of a session. Figure 2 shows the  $\Delta h$  recorded at a fixed frequency over 11 minutes (upper diagram), 5 minutes (middle diagram), and 17 minutes (lower diagram). In the first case, the value  $\Delta h = 450$  m varies through 25 m as session time increases to 11 minutes (the instability of the base is about 5%); it varies by 15 m in the second case (5-6%) and 50 m in the third (8%).

/14

An analysis performed in this way on a large amount of statistical material (about 150 measurements) showed that the measurement base remains practically constant over the recording time for the vertical drift of small-scale inhomogeneities (5-10 m).

This conclusion is valid for constancy of the radiated-frequency difference  $\Delta f$ , which is determined by the instability of the SP-3's smoothly variable local oscillator and ionospheric sounder. The control voltage (jumping scan) is set by a stabilized power source (0.5%), and its influence on  $\Delta f$  does not exceed 500 Hz (at the maximum 100-V modulation of the 100-kHz local-oscillator frequency). The short-term instability of the SP-3's temperature-stabilized smooth local oscillator does not exceed 1.5 Hz/sec after a two-hour warmup [4]. For a sounding frequency of 30 Hz, the frequency drift on successive switchings to  $f_1$  and  $f_2$  does not exceed 0.5 Hz. Thus, the total instability of the frequency difference is of the order of 0.5 kHz (for the average  $\Delta f = 30$  kHz).

/15



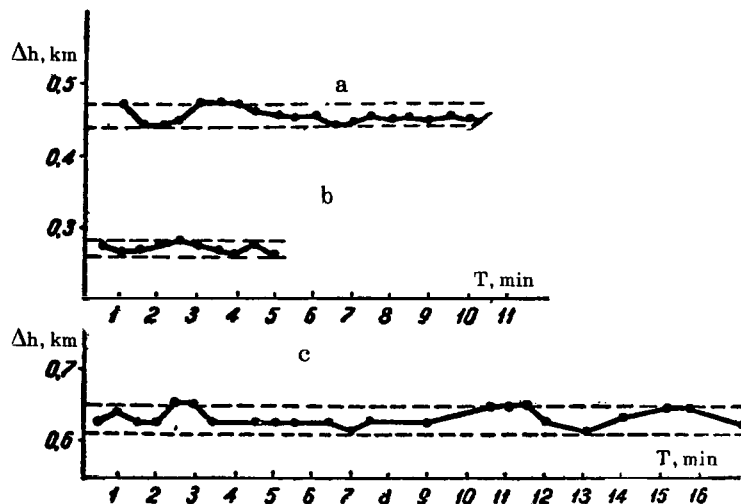


Figure 2. Vertical Base  $\Delta h$  as a Function of Time. Recording: a) 11 minutes; b) 5 minutes; c) 17 minutes.

As a rule, the true-altitude difference  $\Delta h$  corresponding to a 0.3-MHz frequency interval was used in calculating the vertical base. Then, depending on the shift of the simultaneously radiated frequencies,  $\Delta h$  was divided into 10 parts for  $\Delta f = 20$  kHz, 6-7 parts for  $\Delta f = 30$  kHz, and so forth. The justification for using a linear segment to represent this height segment may be questioned. Linearity could be estimated by experimental determination of the phase-frequency characteristic  $dq(f)/df$  for the F-region [4]. The experiment indicates that the deviation from linearity of the recomputed  $h'(f)$  characteristic does not exceed 5-10% in the frequency range all the way down to 0.3-0.5 MHz (with a vertical base of the order of 500-600 m, this amounts to 50-60 m). This conclusion is valid for segments of the  $h'(f)$  characteristic remote from the minimum and critical frequencies of the layer.

For study of small-scale inhomogeneities, the space-diversity observation system consists of a single transmitter and three receiving antennas. Because of the sphericity of the wave, the virtual horizontal drift-rate component of the diffraction pattern at the ground will be twice the drift rate in the ionosphere [3]. Since signals of different frequencies are registered at the same point on the ground in frequency-diversity reception, the apparent rate of the vertical motion measured at the ground will be equal to the rate of the motion in the ionosphere (there is no need to take wave sphericity into account).

## REFERENCES

1. Gusev, V.D., Mirkotan, S.F., Berezin, Yu.V., and Kiyanovskiy, M.P. "Vestn. MGU, seriya fiz.-matem.", 1951, No. 4, 105.
2. Shapiro, B.S. and Kim, K.V. In: "Ionosfernyye issledovaniya" (Ionospheric Research), No. 10, 1962.
3. Mirkotan, S.F. and Kushnerevskiy, Yu.V. In: "Ionosfernyye issledovaniya," No. 12, 1964.
4. Afraymovich, E.L. "Geomagnetizm i aeronomiya," 1968, No. 4.
5. Dnestrovskiy, Yu.N. and Kostomarov, Yu.P. "Geomagnetizm i aeronomiya," 1966, No. 1, 6.
6. Drobzhev, V.I. Author's Abstract of Dissertation, Rostov State University, 1967.

INFLUENCE OF VERTICAL DRIFT OF SMALL-SCALE  
IONIZATION INHOMOGENEITIES ON THE DIURNAL  
VARIATION OF  $f_0F_2$

/16

V.I. Drobzhev

ABSTRACT: The diurnal variations of the critical frequencies of the ionospheric F2 region may be influenced substantially by the 12-hour component of the vertical drift of small-scale ionization inhomogeneities, which enables us to explain a number of characteristic aspects of the diurnal behavior of  $f_0F_2$ : the appearance of the forenoon maximum of  $f_0F_2$  and the evening ionization maximum. With 1 illustration and 6 source citations.

It is known that the ionospheric F2-layer differs substantially from the simple Chapman layer, even on magnetoionospheric-ally quiet days. This phenomenon is usually referred to as the anomaly of the F2-layer. The authors of a number of works have attempted to explain this anomaly in terms of charged-particle drift, which is described by an appropriate term in the ionization-balance equation:

$$\frac{dN}{dt} = Q - \beta N - \operatorname{div} (N\vec{V}),$$

where  $N$  is electron concentration,  $Q$  is the rate of electron formation,  $\beta$  is the recombination coefficient, and  $\vec{V}$  is the drift rate.

In [1, 2], for example, the rapid increase in ionization (or the rapid increase in the critical frequencies) in the F2-region during the morning and the evening ionization maximum were associated with the substantial east-west component of horizontal drift that prevails at these times. V.N. Kessenikh [3] indicates a possible effect of zonal drift on the diurnal variation of electron concentration, suggesting that the real displacements of air masses in the ionosphere at a velocity of 100 m/sec for middle latitudes should introduce quite drastic changes into the pattern of the "mathematical ionosphere."

Such a comparison with consideration of experimental results on the vertical drift of small-scale inhomogeneities will unquestionably be of substantial interest.

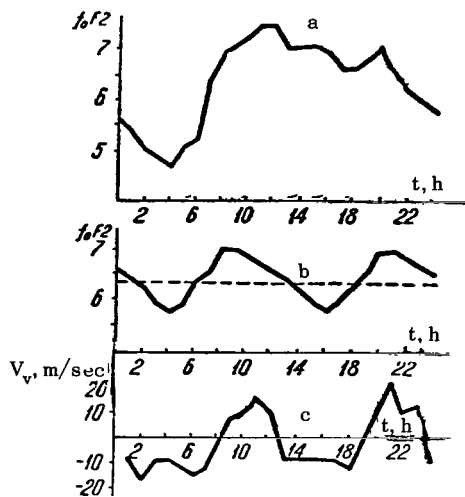


Figure 1. Diurnal Variation of Critical Frequencies  $f_0F2$  Averaged Over May-July 1966 (a); 12-Hour Component of Diurnal Variations of  $f_0F2$  as Resolved by Buys Ballot System (b); Diurnal Variation of Vertical Drift-Rate Component (c).

To judge from curve a (Fig. 1), the critical frequency is 5.5 MHz at midnight; at 4<sup>h</sup>, it reaches a minimum of 4.7 MHz. The critical frequencies increase sharply from 6<sup>h</sup> to 11-12<sup>h</sup>. The largest increase (7.45 MHz) occurs at about 11 hours 13 minutes. A second, early-evening critical-frequency minimum (6.5 MHz) occurs at 18 hours. Also characteristic for this curve is the evening maximum of  $f_0F2$  at 21<sup>h</sup>. Thus, qualitative and quantitative analysis of the diurnal curve indicates that the critical-frequency variations are described for the most part by a 24-hour harmonic and only to an insignificant degree by an indistinct 12-hour component. /17

Since the experimental diurnal curve of the magnitude and direction of the small-scale inhomogeneity drift rate vertical component is described preferentially by the 12-hour periodicity of the motion, it became necessary to isolate the half-day component from the diurnal curve of the critical frequency  $f_0F2$ . The Buys Ballot system, a means of bringing out latent periodicities [4], was

used to permit direct comparison of these curves.

The 12-hour periodicity was brought out more distinctly by analysis of the over-all curve b (Fig. 1). It is easily seen that  $f_0F2$  increases to 6.3 MHz above its median value between 6 and 13 hours and 18 and 1<sup>h</sup>; from 1 to 6<sup>h</sup> and from 13 to 18<sup>h</sup>, it diminishes, with a minimum deviation of 0.65 MHz from the median. The same figure (Fig. 1c) shows the curve of the diurnal changes in the magnitude and direction of the small-scale inhomogeneity drift rate vertical component, also obtained for the summer of 1966 (May, June, July) [6]. From 8 to 13 and from 19 to 24 hours, the drift is upward; from 24 to 8 and from 13 to 19 hours, it is downward with reference to the plane of the horizon (all references are to local zone time). Analysis of these curves indicates that the increase in the critical frequencies  $f_0F2$  coincides basically with the upward direction of drift, and that the decrease corresponds to downward drift. /18

The possible contraction of the ionosphere after daytime warming is regarded as one of the causes of the evening ionization

maximum [5]. However, there is some question as to whether the ionosphere could contract within a comparatively short time — 1-1.5 hours — to such a degree as to bring the critical frequency to the level of the midday value in some cases. With sunset, moreover, the process of electron neutralization is intensified. Thus, it appears to us that an additional mechanism is required to compensate neutralization of the electrons. The occurrence of the evening  $f_0F2$  maximum coincides with the maximum of  $V_v = 20$  m/sec (directed upward) that occurs at this time. It may therefore be assumed that the additional mechanism is vertical transport of ionization from the lower ionosphere. On the other hand, the forenoon and early evening critical-frequency minima appear to result from vertical transfer of ionization downward from the F-region.

According to Chapman's theory, the maximum of the critical frequency  $f_0F2$  should occur at local noon. However, it was found in study of  $f_0F2$  as a function of time of day at the Alma-Ata ionospheric station and at other points that the  $f_0F2$  maximum is shifted away from noon by about 1-2 hours, occurring at 11-12 hours. This departure from the behavior of the hypothetical Chapman F2-layer is known as the diurnal anomaly. The diurnal anomaly can also be explained from the standpoint of allowance for vertical drift. In fact, the maximum of  $f_0F2$  at 11-12 hours coincides with the maximum upward vertical component of the drift rate, which occurs at approximately the same time. The decrease in  $f_0F2$  begins with reversal of the direction of drift (at 12 hours 00 minutes).

Thus, it follows from the above that the diurnal variations of the critical frequencies of the ionospheric F2-region may be substantially influenced by the 12-hour vertical-drift component of the small-scale ionization inhomogeneities, which enables us to explain a number of characteristic features of the diurnal variation of  $f_0F2$ , e.g., the appearance of the forenoon maximum of  $f_0F2$ , the evening ionization maximum, etc.

In our opinion, the significance of the 24-hour component of the diurnal variations of  $V_v$  results not from any real ionization transport, but from peculiarities in the variation of the electron formation rate function  $Q$  and the loss coefficient  $\beta$ .

/19

## REFERENCES

1. Berkeliyev, M. "Izv. AN TurkSSR, seriya FTKh i GN," 1963, 6, p. 15.
2. Hirsch, A.I. and Knecht, R.W. "J. Geoph. Res.," 1962, 67, 2.
3. Kessenikh, V.N. Trudy SFTI, No. 41. Tomsk, 1961, p. 3.
4. Serebrennikov, M.G. and Pervozvanskiy, A.A. Vyyavleniye

- skrytykh periodichnostey (Detection of Latent Periodicities).  
Moscow, "Nauka," 1965.
5. Likhachev, A.I. Trudy SFTI, No. 33, Tomsk, 1954, p. 51.
  6. Drobzhev, V.I. "Geomagnetizm i aeronomiya," 1968, 8, No. 2.

IONOSPHERIC MAGNETIC PHENOMENA ASSOCIATED WITH  
PROTON FLARES

/20

M.P. Rudina and N.F. Solonitsyna

ABSTRACT: The state of the ionosphere above stations in Kazakhstan is examined in connection with the proton flares of 7 July, 28 August, and 2 September, 1966. The experimental data are analyzed and reduced by the customary method. Universal Time (UT) is used. It is established that a proton flare causes increased radio absorption (the ionization of the D-region is enhanced, and the minimum reflected frequencies decrease); magnetic storms and ionospheric disturbances are observed on the earth one-and-a-half to two days after some proton flares.

To ascertain the influence of proton flares on the state of the earth's magnetic field and ionosphere, the periods from 5 through 11 July, 27 August through 6 September, and 18 through 22 September 1966 were studied in data from the combined magnetic-ionospheric stations in Kazakhstan: those at Karaganda, Novo-Kazalinsk, and Alma-Ata. If we accept the convention that flares are proton flares if, in addition to increased intensities in the x-ray and ultraviolet regions of the spectrum, they eject appreciable numbers of protons — no fewer than  $10^2$  protons/cm<sup>3</sup> with energies of  $\sim 100$  MeV — then proton flares were observed on 7 July at 00 hours 22 minutes, on 28 August at 15 hours 26 minutes, and on 2 September at 05 hours 45 minutes [1, 2]. Ordinary chromospheric flares were recorded from 18 through 22 September [3]. We have examined this time segment to compare the effects of proton and nonproton flares.

In most cases, solar flares, and the intense ones in particular, result in changes in the parameters characterizing the state of the earth's magnetic field and ionosphere. In the conventional approach [4], the state of the ionosphere is considered to be disturbed and is evaluated in points on a scale when the F2-layer critical frequencies ( $\Delta f_0 F2$ ) deviate by at least 20% from the median values and departures from the usual structure of the layer are observed for several hours. Magnetograms were inspected to evaluate the state of the earth's magnetic field with the degree of disturbance determined from the K-index; for the ionosphere, the deviations  $\Delta f_0 F2$  were the principal subject of study. In the case of detailed investigation of the ionosphere's structure,





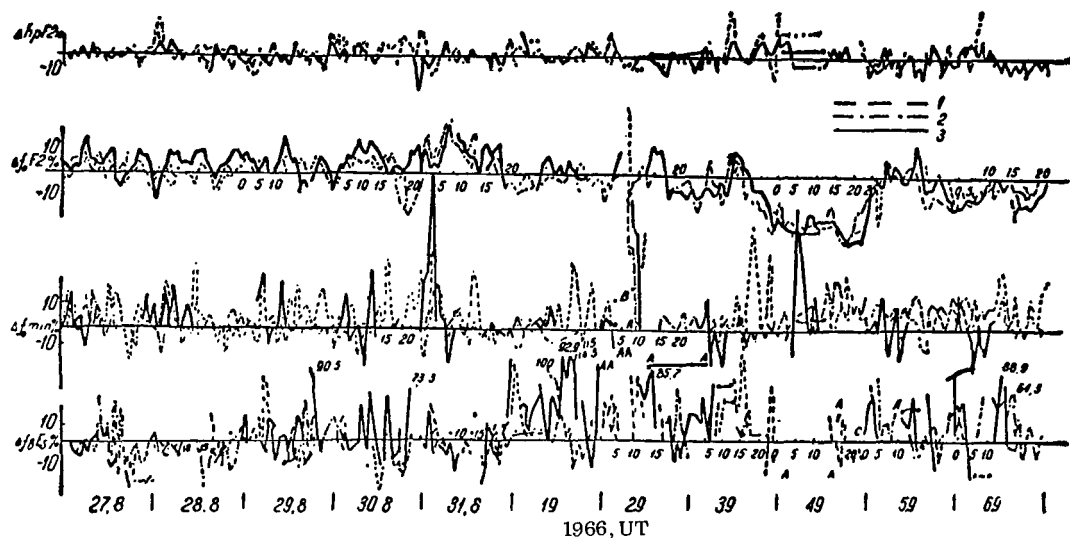


Figure 2.  $\Delta f_b E_s$ ,  $\Delta f_0 \min$ ,  $\Delta f_0 F2$ , and  $\Delta h_p F2\%$  from 27 August Through 6 September 1966. 1) Karaganda; 2) Novo-Kazalinsk; 3) Alma-Ata.

The critical frequencies increased slightly in the F-region at the times of the flares. When the flare occurred on 28 August the ionosphere above Kazakhstan was on the night side, and no wave effect appeared. Nor did it appear from 18 through 22 September, during a period of ordinary chromospheric flares.

Storms began in the magnetic field approximately 22 hours after the flares of 7 July and 28 August, when the geoeffective corpuscular stream arrived at the earth. The storm was moderate in the first case and mild in the second, increasing to moderate on 30 August and continuing until 23 hours on 1 September. The earth's magnetic field had not quite had time to quiet down when another proton flare occurred at 5 hours 45 minutes on 2 September, and a major storm began in the magnetic field on 2 September at 8 hours 23 minutes, continuing until 17 hours on 6 September.

The major storm may have resulted from the combined action of several flares, including nonproton flares, which occurred on 30 August at 15 hours 45 minutes and 31 August at 1 hour 12 minutes [2]. During the period from 18 through 22 September, a moderate magnetic storm was registered from 2 hours 52 minutes on 19 September until 20 hours on 20 September, with occasional flareups until 14 hours on 21 September, the latter probably due to a complex of chromospheric flares [3].

The corpuscular effects of the flares in the ionosphere always took different forms. After the flare of 7 July, the

ionospheric disturbance began 21 hours 40 minutes later and did not exceed 1 point. At Karaganda, it was single-phased and negative, with a deviation  $\Delta f_0 F_2 = -24.5\%$ ; at Novo-Kazalinsk, it was single-phased and positive with  $\Delta f_0 F_2 = +27.4\%$ ; at Alma-Ata, it was two-phased negative-positive with maximum deviations of  $\Delta f_0 F_2 = -22.7\%$  in the negative phase and  $\Delta f_0 F_2 = +24.2\%$  in the positive phase (Fig. 1).

On 30 August, approximately two days after the flare of 28 August, an ionospheric disturbance began above the Kazakhstan stations (Fig. 2). It was more intense than the preceding storm, and a positive phase was observed at all stations. Its intensity reached  $-3$  at Karaganda,  $+3$  at Alma-Ata, and  $\pm 2$  at Novo-Kazalinsk. In addition, it was two-phased negative-positive at Karaganda, positive-negative at Novo-Kazalinsk, and single-phased positive but quite intense ( $+3$ ) at Alma-Ata. While the intensity was 1 after the flare of 7 July, an intensity of  $\pm 2$  predominated after the flare of 28 August. The flare of 2 September caused a very strong ( $\pm 3$ ) and persistent disturbance in the ionosphere, with a negative phase at all stations (Fig. 2). It began quite a bit earlier than the disturbances following the first two flares. A single-phased negative disturbance was registered over Karaganda and Novo-Kazalinsk, with maximum deviations of  $\Delta f_0 F_2 = -47.3\%$  at Karaganda and  $\Delta f_0 F_2 = -47.7\%$  at Novo-Kazalinsk. At Alma-Ata, it was two-phased positive-negative and stronger and more persistent than at the other two stations. The maximum deviations were  $\Delta f_0 F_2 = +37.5\%$  and  $-58.1\%$ . On 4 September, a day-long three-point negative disturbance was observed above Kazakhstan according to data from all three stations (Fig. 2).

/23

The critical frequencies were observed to be stable during the disturbances, especially at the maxima of the negative storm phases. As a rule, the heights of the layer maximum  $h_p F_2$  (Figs. 1 and 2) and the beginning of the layer,  $h'F$ , increased sharply at the beginning of the negative phase. Where the disturbance was positive, these heights decreased. The height changes were particularly marked at the beginnings and at the maxima of the phases. The heights  $h_p F_2$  and  $h'F$  varied less strongly during positive disturbances than during negative disturbances.

According to data from the Karaganda station, the limiting frequencies of the sporadic  $E_s$ -layer increased from 8 to 11 hours on 8 July. The heights  $h'E_s$  showed no appreciable change. Very high limiting frequencies were observed on 11 July at the three stations, and also on 10 July above Alma-Ata and Novo-Kazalinsk. The shielding frequency  $f_b E_s$  increased during this time. The limiting frequencies were higher from 5 to 7 hours on 31 August over Karaganda. No particular changes in  $E_s$  were reported after

the 2 September flare if we discount a slight increase in the limiting frequency  $f_oE_s$  at Alma-Ata from 00 to 5 hours on 6 September and at Novo-Kazalinsk from 9 to 13 hours.

/25

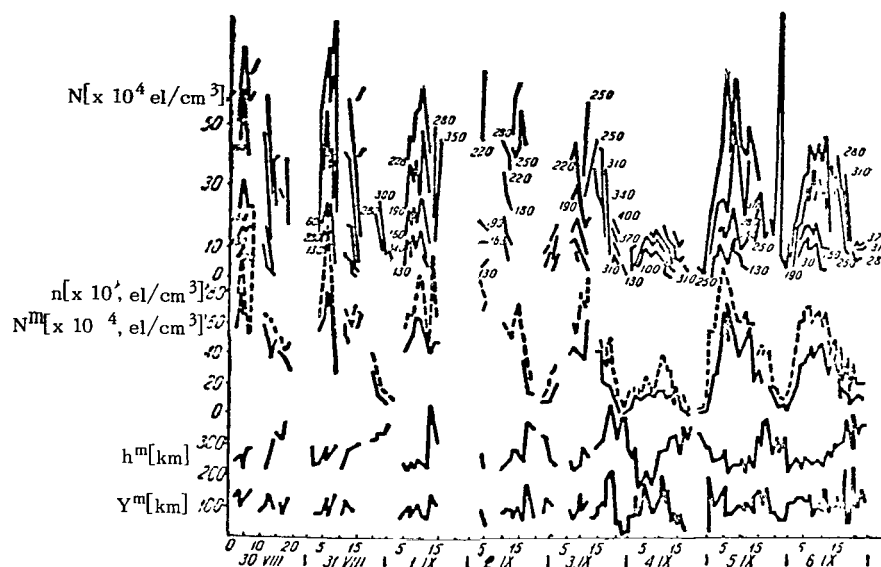


Figure 3.  $y^m(\text{km})$ ;  $h^m(\text{km})$ ;  $N^m[\times 10^4, \text{el}/\text{cm}^3]$ ;  $n[\times 10^4, \text{el}/\text{cm}^3]$ ;  $N[\times 10^4, \text{el}/\text{cm}^3]$  from 30 August Through 6 September 1966, According to Data from Alma-Ata Station.

Analysis of five-minute recordings of the height-frequency characteristics indicated that the structure of the ionosphere varied in a complex manner during the active phases of the disturbances. In addition to the sporadic formations, there were reflections from interlayers and a G-region. The behavior of the ionosphere from 18 through 22 September 1966 permitted the conclusion that the ordinary chromospheric flare caused no disturbances in the ionosphere or geomagnetic field. However, this conclusion cannot be regarded as final, since there is as yet no precise definition of the proton flare [5].

It was found that a decrease in ionization at the maximum of the F-layer ( $N_{\text{max}}$ ) on the  $N(h)$  profiles, such as that on 4 September 1966 (Fig. 3), when a negative disturbance phase was observed, was accompanied by an increase in the half-thickness ( $y_m$ ). The height  $h_{\text{max}}$  of the ionization maximum varies in antiphase with the half-thickness. The ionization at levels corresponding to 100, 110, and 130 km varies in synchronism with  $y_m$ . An increase in half-thickness indicates expansion of the layer, obviously due to heating through dissipation of the energy of

magnetohydrodynamic waves passing downward through the ionosphere [6]. During the main phase of the disturbance, the total ionization ( $n$ ) and the ionization at the maximum fell off markedly. The electron concentration varied for the most part at heights above 130 km and most strongly near the layer maximum.

From comparison of the effects of proton and nonproton solar flares in the earth's magnetic field and ionosphere, we have found that proton flares caused increased absorption of radio waves and magnetoionospheric disturbances. The aggregate of magnetoionospheric disturbances caused by proton flares is complex and varied, and the number of periods studied is inadequate to permit any definite conclusions as to the nature of the action of proton flares on the earth's ionosphere and geomagnetic field at this time. Research is being continued in this direction during the 1969-1970 solar maximum activity (IASY).

### REFERENCES

1. Notes IQSY. International Council of Scientific Unions Special Committee for the International Years of the Quiet Sun, 1967, April, No. 20.
2. In: "Solnechnyye dannyye" (Solar Data), 1966, No. 8.
3. In: "Solnechnyye dannyye," 1966, No. 9.
4. Zevakina, R.A., Lavrova, Ye.V., and Lyakhova, L.N. Osnovy prognozirovaniya ionosferno-magnitnykh vozmushcheniy i sluzhba kratkosrochnykh radioprognozov (Bases for the Prediction of Ionospheromagnetic Disturbances and the Short-Term Radio-Transmission Forecasting Service), Moscow, "Nauka," 1967.
5. Pushkov, N.V. and Zhulin, I.A. The Effects of the Sun on Terrestrial Phenomena. "Vestnik AN SSSR," 1968, No. 4, Part 3.
6. Dessler, A.J. Ionospheric Heating by Hydromagnetic Waves. "J. Geophys. Res.," 1959, No. 4, 64, 397-401.

PARAMETERS OF SMALL-SCALE IONIZATION INHOMOGENEITIES  
IN THE F-REGION OF THE IONOSPHERE

/27

V.I. Drobzhev

ABSTRACT: The results of a study of the parameters of small-scale ionization inhomogeneities of the ionosphere's F-region for October-November 1965 and January-February 1966 are presented. It is shown that the most probable values of the inhomogeneity parameters are as follows: degree of anisotropy 1.4-2; vertical dimension 200-400 m; horizontal dimensions along major and minor axes 400-1000 and 200-600 m, respectively; rate of chaotic motions 30-60 m/sec; lifetime 6-9 sec. With 1 illustration and 8 source citations.

In September 1965, working with the Ionosphere Sector of the Academy of Sciences of the Kazakh SSR, the author began reduction of observational results on movements in the F2-region of the ionosphere by the method of complete correlation analysis; eventually, 289 recordings obtained in October-November 1965 and January-February 1966 were processed. A Minsk-1 electronic computer was used to calculate one auto- and six mutual correlation functions from approximately 800 discrete amplitude values for each recording. The formulas for calculation of the correlation functions and estimating their errors are given in [1].

The characteristic  $V'_c$  and virtual  $V'$  velocities along the baselines and the correlation radius  $r_{0.5}$  are quite simply determined from the form of the correlation functions and the geometry of the measurement triangle. It is sufficient to know  $V'_c$ ,  $V'$ , and  $r_{0.5}$  to determine the inhomogeneity parameters of interest to us [2].

The form and horizontal and vertical dimensions of the small-scale inhomogeneities were determined by correlation analysis and construction of the so-called characteristic ellipse — the ellipse of anisotropy. Its shape and orientation were used to calculate the prolateness parameter  $l = a/b$  ( $a$  and  $b$  are the major and minor axes of the ellipse), the angle  $\alpha$  (the preferred direction of the prolateness), and  $\Delta_{\max}$  and  $\Delta_{\min}$  (the dimensions of the ellipse along its major and minor axes. Strictly speaking, it is the form and dimensions of diffraction-pattern spots on the surface of the earth that are defined here. The extent to which the properties of the diffraction pattern conform to those of the

ionosphere remains to be determined. However, it has been pointed out in certain theoretical studies that if the working wavelength is shorter than the inhomogeneity dimensions and the signal is shaped in a reflection region, the horizontal dimensions of the inhomogeneities in the ionosphere and the pattern on the earth's surface coincide on the average [3]. In view of this, we can speak only of certain effective inhomogeneity dimensions. /28

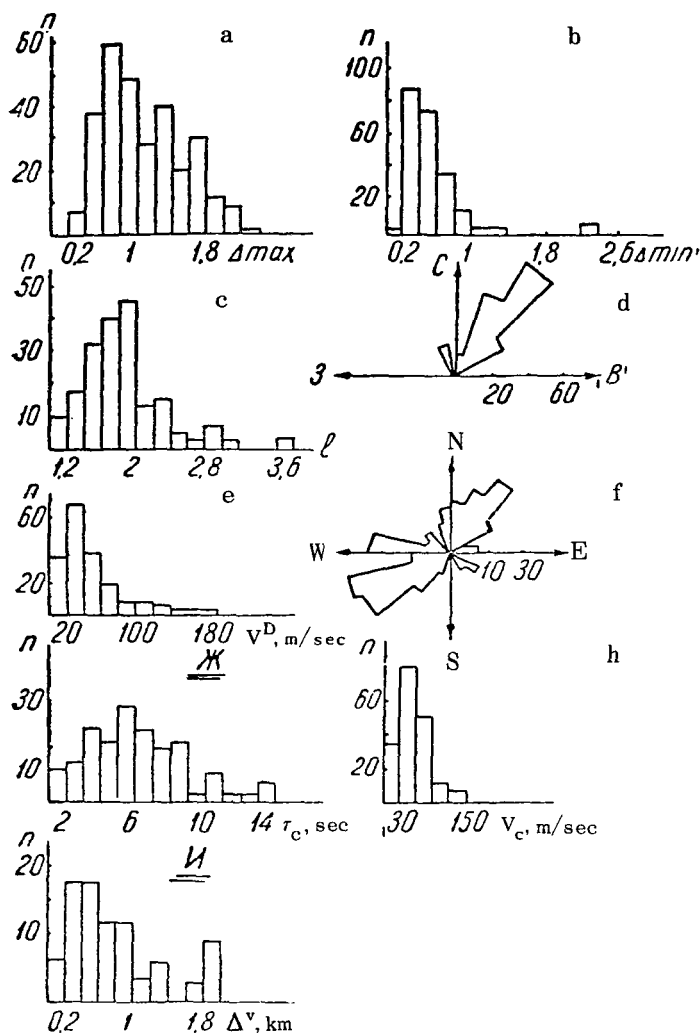


Figure 1. Distribution Histograms of a, b) Inhomogeneity Dimensions Along Axes of Characteristic Ellipse; c) Degree of Anisotropy; d) Direction of Prolateness; e, f) Magnitude and Direction of Drift Rate; g) Inhomogeneity Lifetime; h) Velocity of Chaotic Motions; i) Vertical Dimension of Inhomogeneities.

It is evident from the results of processing of the records obtained in October-November 1965 and January-February 1966 that the ratio of the axes of the characteristic ellipse varies from 1 (which corresponds to the isotropic case) to 3.8, with the most probable value of  $\underline{l}$  in the range from 1.4 to 2 (Fig. 1c). The angle  $\alpha$  varies from 0 to 60°, with a most probable value of 30-45° (Fig. 1d). The parameter  $\underline{l}$  is not observed to depend on the time of day or the season. The experimental values obtained for  $\underline{l}$  and  $\alpha$  confirm the previously posited shape anisotropy of the small-scale inhomogeneities, with preferential orientation along the magnetic field [4].

The shape anisotropy of the inhomogeneities can be explained by the difference between the coefficients of diffusion along and across the earth's magnetic lines of force ( $D_{11} > D_1$ ). Here the originally isotropic electron formation is stretched out in the direction of the magnetic field. Calculations of the lifetime and distension of the inhomogeneity confirm this hypothesis [5].

The horizontal dimensions of small-scale inhomogeneities are calculated by the formula

$$\Delta = 4\tau_{0.5}V'_c,$$

where  $\tau_{0.5}$  is the correlation radius, which satisfies the relation  $\rho_{ij}(\tau_{0.5}) = 0.5$ ;  $V'_c$  is the value of the characteristic velocity along the minor and major axes of the ellipse of anisotropy.

The distribution of the inhomogeneity dimensions along the major ( $\Delta_{\max}$ ) and minor ( $\Delta_{\min}$ ) axes of the characteristic ellipse is shown in the figure. To judge from the histograms, the inhomogeneity dimensions vary from 200 to 2200 m for  $\Delta_{\max}$  and from 200 to 1400 m for  $\Delta_{\min}$ , with dimensions of the order of 400-1000 and 200-600 m encountered most frequently along the major and minor axes, respectively. It must be noted that these values are in rather good agreement with calculated values for the linear scale of the inhomogeneities [6] and with the results of experimental studies by other authors [4].

Recordings obtained in October-November 1965 (by frequency-diversity reception) were used to evaluate the vertical dimensions of small-scale ionization inhomogeneities. The determination of  $\Delta_v$  was based on a simplified model [7]. Assume that the ionosphere is sounded by pulses at four frequencies  $f_1, f_2, f_3$ , and  $f_4$ , with  $\Delta f = |f_2 - f_1|, |f_3 - f_2|$  etc.  $< f_1, f_2, f_3, f_4$ . These four waves are reflected from their different levels in the ionosphere. Then  $\Delta f = |f_2 - f_1|$  will correspond to  $\Delta z = |z_2 - z_1|$ , the shift of the reflection levels of the waves with different frequencies; /30

$z_1$  and  $z_2$  are the respective distances from the surface of the earth to the points of reflection of frequencies  $f_1$  and  $f_2$ ;  $\Delta f = |f_2 - f_1|$  will correspond to  $\Delta z = |z_2 - z_1|$  etc. The distance between the reflection levels will increase with increasing separation of the simultaneously radiated frequencies. The effect is that of two screens with random field distribution. The mutual correlation coefficient  $R_{ij}/ij = 1, 2, 3, 4$  may serve as a quantitative index to the property similarity of these targets. The mutual correlation coefficient is 1 for a frequency separation  $\Delta f = 0 | \Delta z = 0 |$ . The  $\Delta z$  will increase and the  $R_{ij}$  decrease with increasing  $\Delta f$ , since the field on the screens will show greater differences in detail.

In practice, the fields can be assumed independent if the mutual correlation coefficient  $R_{ij} \leq 0.5$ . This value of  $R_{ij}$  is known as the radius of the frequency correlation [8]. The shift  $\Delta z$  of the reflection regions corresponding to the frequency-correlation radius can be taken as a certain effective vertical dimension of the small-scale inhomogeneities [7]. Generally speaking, this holds if the inhomogeneous structure of the fields corresponds to the inhomogeneous structure of the medium itself. The method and results of calculation of the frequency-correlation radius and  $\Delta Z$  — the reflection-region shift — are set forth in [8].

It was found that the effective vertical dimensions of the small-scale inhomogeneities vary from 100 to 2000 m, and that dimensions of the order of 200-400 m are most frequently encountered. No particular dependence of the vertical dimensions on time of day was detected; there was only an insignificant tendency toward smaller dimensions with the transition from day to night.

Comparing the experimental data obtained on the vertical dimensions and the results of horizontal-dimension measurements, we may conclude that the inhomogeneities are characterized by an approximately volume-symmetrical shape (considering the small anisotropy of the inhomogeneities in the horizontal plane,  $l = 1.4 - \alpha$ , and the simplifying assumptions adopted in calculation of the vertical and horizontal dimensions).

Regular drift of inhomogeneities. The drift rate was determined from the relationship

$$V_D = \frac{V_c'^2}{2V'}, \quad /31$$

where  $V_c'$  is the characteristic velocity in the direction of drift and  $V'$  is the virtual velocity obtained from the time shifts of



the cross-correlation functions.

Drift-rate magnitude and direction distribution histograms are given in Fig. 1 (e, f). We find that regular drift occurs in the F2-layer with velocities from 0 to 200 m/sec. The most probable velocity values lie in the range from 20 to 60 m/sec. Comparing these results with data on the distribution of the drift velocities  $V'$  determined by the fading-similarity method, we soon note that the drift rate  $V_D$  is usually smaller than  $V'$ .

Chaotic motions are evidently an important factor in the motions of small-scale inhomogeneities. The method of complete correlation analysis takes these motions into account, so that

$$V_D < V'.$$

Chaotic motions are also important in the ionosphere. The rate of the chaotic processes was calculated by the following formula in the application of correlation analysis:

$$V_c = \frac{1}{2} \sqrt{V_c'^2 - V_D^2},$$

where  $V_c'$  is the characteristic velocity and  $V_D$  is the regular drift rate.

Generally speaking, there is no clear physical interpretation of  $V_c$ , although it characterizes to some extent the degree to which chaotic variations affect the state of the diffraction pattern at the surface of the earth. The velocity of the chaotic motions varies from 1 to 150 m/sec, with the most probable value of  $V_c$  in the range from 30 to 60 m/sec (Fig. 1e). Considerable interest attaches to the distribution of the velocity ratio of the chaotic motions and the regular drift, i.e.,  $V_c/V_D$ . It is found that  $V_c/V_D$  varies from 0 to 3.5, with values of the order of 1 and 2 encountered most often. Consequently, the rates of chaotic processes exceed the regular drift velocities of the small-scale inhomogeneities.

The correlation analysis indicates that the rates of the chaotic variations are related to another parameter,  $\tau_c$ , which characterizes the dissolution of the inhomogeneities in the relationship

$$\tau_c = 2\tau_{05} \frac{V_c'}{V_c},$$

/32

where  $\tau_{0.5}$  is the time correlation radius,  $V_c$  is the rate of the chaotic processes, and  $V'_c$  is the characteristic velocity in the direction of the drift velocity.

The results of calculation of  $\tau_c$ , the "lifetime" of the inhomogeneities, appear in Fig. 1g.  $\tau_c$  varies from 3 to 15 sec. The most probable value lies in the 6-9-second range.

The dissolution of small-scale inhomogeneities is governed by diffusion processes, turbulent mixing of the medium, and also possibly on the chaotic motions of the inhomogeneous formations themselves. The contribution of each of these factors to the chaotic variation has not yet been established, although it is known that they play an important role in the behavior of the ionosphere.

### CONCLUSIONS

1. The experimental results confirm the prolateness of small-scale inhomogeneities with  $\underline{1} \sim 1.4 - 2$  and the most frequently encountered  $\alpha \sim 30-45^\circ$ .

2. The horizontal dimensions of the inhomogeneities along the major and minor axes of the characteristic ellipse are 400-1000 and 200-600 m, respectively. The most probable vertical dimension of the small-scale inhomogeneities is 200-400 m, i.e., approximately equal to the horizontal dimension.

3. The velocities of regular inhomogeneity drift (30-40 m/sec) determined by the method of complete correlation analysis were found to be lower than those calculated by the fading-similarity method (40-70 m/sec). The chaotic motions have velocities of 30-60 m/sec.

4. The most probable value of the dissolution time  $\tau_c$  of the inhomogeneities is 6-9 seconds.

### REFERENCES

1. Drobzhev, V.I. "Geomagnetizm i aeronomiya," 1967, No. 6, 1.
2. Mirkotan, S.F. and Kushnerevskiy, Yu.V. "Ionosfernyye is-sledovaniya," 1964, No. 12, 116.
3. Gusev, V.D. "Radiotekhnika i elektronika," 1959, 4, 1, 12.
4. In: "Dreyfy i neodnorodnosti v ionosfere" (Drifts and Inhomogeneities in the Ionosphere), No. 1, Moscow, Izd-vo AN SSSR, 1959.
5. Mirkotan, S.F., Kushnerevskiy, O.V. and Gusev, V.D. In: "Is-sledovaniya neodnorodnostey v ionosfere" (Studies of

/33

Inhomogeneities in the Ionosphere), No. 4, Moscow, Izd-vo AN SSSR, 1960.

6. Al'pert, Ya.L. In: "Issledovaniya ionosfery i meteorov" (Studies of the Ionosphere and Meteors), No. 2, Moscow, Izd-vo AN SSSR, 1960.
7. Mirkotan, S.F. Author's Abstract of Dissertation, Moscow, Moscow State University, 1955.
8. Drobzhev, V.I. "Geomagnetizm i aeronomiya," 1966, No. 6, 4.

T.K. Yakovets

ABSTRACT: Diurnal and seasonal absorption curves measured by a radioastronomical method at Alma-Ata during the IQSY (1964-1965) are submitted. The apparatus is described. The dependence of absorption on solar flares is indicated.

During the IQSY (1964-1965), ionospheric absorption was measured in the Ionosphere Sector of the Academy of Sciences of the Kazakh SSR in the process of registering the cosmic radio emission at 24.6 MHz. This method of measuring absorption (A2) yields continuous round-the-clock absorption data; it requires uncomplicated equipment that does not include radio transmitting devices and, consequently, does not create noise. This method can be used to measure the anomalously strong absorption during ionospheric disturbances, when the pulse method cannot be used because of the strong absorption at low frequencies. This method permits inferences as to the height of the absorbing region when several riometers are used at different frequencies at the same station [1] and can be used to study chromospheric flares on the sun [2]. Unlike the pulse method, method A2 makes it possible to measure the total absorption in the ionosphere, which can be broken down into the absorptions introduced by the separate layers [3, 4]. To obtain the final absorption data, it is necessary to perform measurements throughout an entire year. Only then does it become possible to construct a quiet-day (unabsorbed-level) curve. It is known that the cosmic noise level is highest when the ionization of the ionosphere is at minimum, i.e., in the later hours of the night. To present the complete diurnal curve of the unabsorbed level, therefore, it is necessary to have observations taken over the year at all sidereal times. The ratio of the unabsorbed cosmic-noise level and the observed level at the same sidereal time expresses the amount of absorption:

$$L = -10 \log \frac{P}{P_0}.$$

Here  $P$  is the power of the cosmic noise that has passed through the ionosphere and arrived at the receiver input and  $P_0$  is the power of the cosmic radio emission received by the receiver in the absence of ionospheric absorption.

/35

Apparatus for registration of cosmic noise. A simple apparatus consisting of an R-250M receiver, an EPP-09 automatic recorder, and a Yagi antenna (Fig. 1) was used.

The signal from the intermediate-frequency output of the receiver was fed through a cathode follower to a diode detector (D), from whose load it proceeded to the automatic recorder. The record was calibrated with a noise generator (NG), for which purpose the noise generator was connected to the receiver input instead of the antenna by means of a switch. The generator's output-power level was set in such a way that the deflection of the recorder pen would correspond to the level of the signal trace.

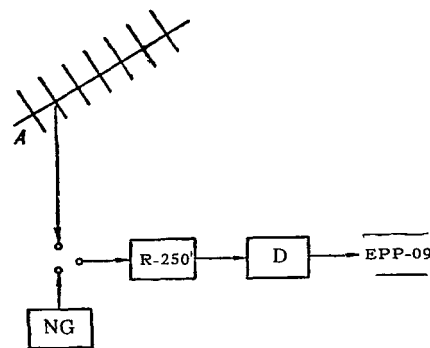


Figure 1. Block Diagram of Apparatus for Absorption Measurement.

Stabilized power sources were used, ensuring stability of the reception channel characteristics.

The antenna was pointed at Polaris. This pointing was selected in order to reduce the stellar component during registration of the cosmic noise. The region of Polaris is seen at a certain constant angle from any point on the earth. Even though the region of the celestial sphere around Polaris that is beamed by the major lobe of the antenna pattern includes discrete radio sources, the received noise level will not vary appreciably over the sidereal day, since this entire zone of the celestial sphere, rotating around Polaris on the celestial axis, remains at all times in the beamed region, and the over-all radio emission does not vary.

/36

Results of measurements. Previously, we had processed traces of the cosmic-noise intensity during the IQSY (1964-1965) by a method developed by the Leningrad Arctic and Antarctic Scientific-Research Institute [5]. The absorption values obtained were of the order of 1.5-2.5 dB, or at variance with the theoretically calculated absorption for this frequency (24.6 MHz). In addition, the seasonal variation of absorption in 1965 was found to be the opposite of that observed in 1964. Measurements over this period were therefore reprocessed with consideration of procedure changes proposed by M.D. Fligel' and N.A. Kochenova [IZMIR AN SSSR (Institute of Terrestrial Magnetism, the Ionosphere, and Radio Wave Propagation of the Academy of Sciences of the USSR)].

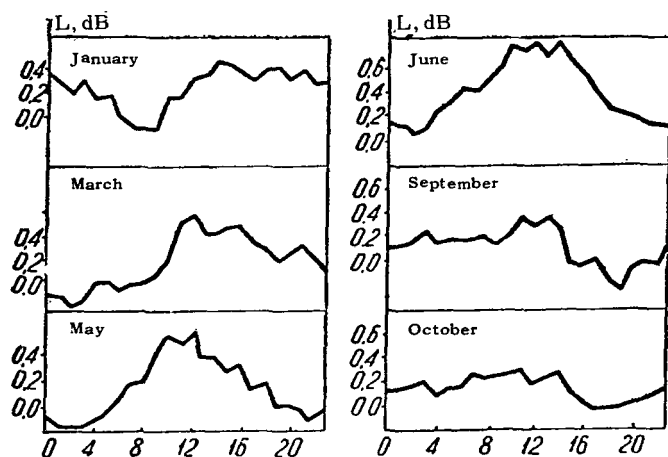


Figure 2. Diurnal Variation of Cosmic Noise Absorption.

Diurnal variation of absorption. In most cases, maximum absorption is observed at noon (Fig. 2). On certain curves (January), the maximum is shifted toward the evening hours. In September and October, the diurnal variation of absorption is less pronounced. The maximum absorption is 0.8 dB (May-June). Negative values indicate that the power of the cosmic radio emission was greater at this time than the noise power according to the quiet-day curve.

/37

Such cases were possible because the quiet-day curve was derived in accordance with the third maximum value for each hour.

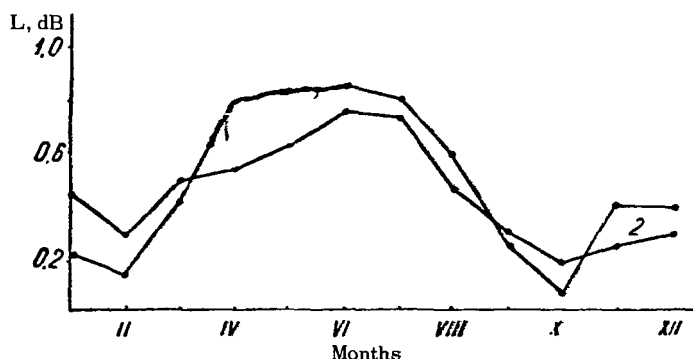


Figure 3. Seasonal Variation of Absorption. 1) 1965; 2) 1964.

Seasonal variation of absorption. Absorption is considerably stronger in the summer months than it is in winter (Fig. 3). The lowest absorption values are observed in February and October. The higher absorptions in December and January can apparently be explained in terms of the winter anomaly. The seasonal absorption curves for 1964 and 1965 agree quite closely.

Absorption of cosmic noise during solar flares. To determine the manner in which absorption is affected by solar chromospheric flares, we analyzed traces of the cosmic noise acquired over three months (July, August, September) in 1966. It was noted that absorption increased substantially during solar

TABLE

Date	SCNA			Maximum $\Delta L$ , dB	Solar flare			Field strength	Ionospheric data (f min)
	Time of onset (UT)	Maximum phase (UT)	Duration, min		Time		Maximum phase (UT)		
					Beginning (UT)	End (UT)			
9 Jul 1966	3 <sup>h</sup> 10'	3 <sup>h</sup> 25'	50	2.6				Radio signal not heard	Dellinger effect
31 Aug 1966	2 <sup>h</sup> 50'	3 <sup>h</sup> 52'	105	0.90	2 <sup>h</sup> 50'	4 <sup>h</sup> 35'	3 <sup>h</sup> 52'	—	1.9
		2 <sup>h</sup> 52'		0.80			2 <sup>h</sup> 52'		2.4
2 Sep 1966	5 <sup>h</sup> 45'	~12 <sup>h</sup>	~160	Signal dropped to 0 at gain used	5 <sup>h</sup> 43'	8 <sup>h</sup> 15'	5 <sup>h</sup> 57'	Radio signal not heard	Dellinger effect
8 Sep 1966	5 <sup>h</sup> 30'	5 <sup>h</sup> 40'		0.40	5 <sup>h</sup> 34'	5 <sup>h</sup> 37'	5 <sup>h</sup> 45'	—	1.6
14 Sep 1966	3 <sup>h</sup> 12'	3 <sup>h</sup> 16'	30	0.22	3 <sup>h</sup> 11'	3 <sup>h</sup> 42'	3 <sup>h</sup> 14'	—	1.3

chromospheric flares. Larger absorption increases correspond to more intense flares. Thus, the cosmic-noise level dropped to zero during the flare of 2 September 1966. The absorption data were compared with the minimum reflection frequency  $f_{\min}$  and with field-strength measurements. During the strong flares of 2 September and 9 July, the Dellinger effect intervened and the signal from the radio station was not monitored. In the other cases (31 August, 8 September, 14 September), the minimum reflection frequencies increased over those of the quiet period, while the field-strength traces showed no effects from the flares (Table).

## CONCLUSIONS

/39

1. In the majority of cases, the monthly-average diurnal variation of absorption is quite clearly in evidence. The absorption maximum occurs during the midday hours and those immediately preceding and following.

2. The seasonal absorption curve has its maxima in May-July and its minima in February and October. The winter anomaly is observed in December-January.

3. A distinct relation is traced between absorption increase and chromospheric flares on the sun.

## REFERENCES

1. Benediktov, Ye.A. and Korobkov, Yu.S. Absorption of Cosmic Radio Emission During the Magnetic Storm of 15 July 1959. "Izv. vuzov, radiofizika," 1960, No. 2, 3.
2. Radicella, S.M. Effects of Solar Radio Bursts on Riometers at 30 Mc/s. "J. Geophysical Res.," 1965, 70, No. 23, 5970-5974.
3. Benediktov, Ye.A. et al. Results of Measurement of the Absorption in the Ionosphere. "Izv. vuzov, radiofizika," 1960, No. 6, 3.
4. Lusignan, B. Cosmic Noise Absorption Measurement at Stanford, California and Pulman, Washington. "J. Geophys. Res.," 1960, No. 12, 65, 3881-3902.
5. Instruktsiya po obrabotke zapisov intensivnosti kosmicheskogo radioizlucheniya (Instructions for Processing of Cosmic Radio Emission Intensity Records) (edited by V.M. Driatskiy). Leningrad, Arctic and Antarctic Scientific-Research Institute, 1965.



THE IONOSPHERE ABOVE ALMA-ATA DURING A  
SOLAR ECLIPSE

/40

M.P. Rudina and P.Ye. Kozina

ABSTRACT: The influence of the solar eclipse observed at Alma-Ata on 23 November 1965 on the parameters of the ionosphere is examined. The eclipse effect was manifested during the second phase: the ionization of the F1- and F2-layers decreased and the minimum effective heights of E and F2 increased due to recombination processes. The manner in which electron density is distributed over the levels was ascertained from analysis of N(t) curves.

It is known that eclipses of the sun have appreciable influence on the ionosphere: electron content decreases, and the effective layer heights, the distribution of electron concentration, and other characteristics undergo changes.

Data on the influence of the solar eclipse of 23 November 1965 on the ionosphere were acquired by vertical sounding. An annular partial solar eclipse was observed during the morning hours, with a maximum obscuration of 0.75 at 7 hours 37 minutes (75° E time). The beginning of the eclipse coincided with sunrise (Fig. 1, a and b).

The parameters of the ionosphere on the day of the eclipse and on control days were measured with an AIS ionospheric recorder. The ionospheric records were registered at 15-minute intervals during the control period, every 5 minutes on the day of the eclipse, and continuously during the eclipse. A computer was used to obtain the true heights from the ionospheric records, and these heights were used to evaluate the effective recombination coefficient and determine the time relationships for the altitude distribution of electron density.

Critical frequencies. On the day of the eclipse (Fig. 1a), the stratification of the region into F-, F1-, and F2-layers was indistinct (L). The values of  $f_oF1$  after the eclipse differed little from the averages for the control days, while  $f_oE$  had decreased by about 0.5 MHz. During the entire period of sunlight after the eclipse, reflections from the sporadic E-layer were observed, with limiting frequencies up to 4 MHz.

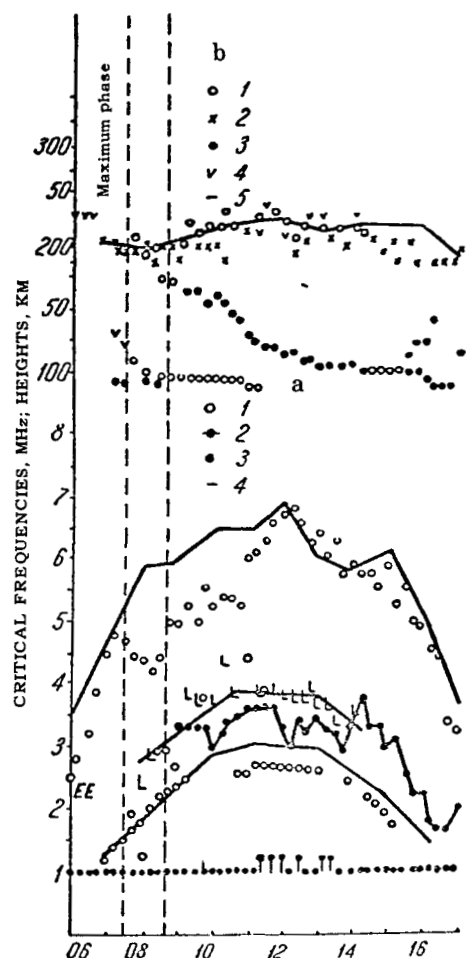


Figure 1. Curves of  $f$  and  $h'$  on 23 November 1965,  $75^\circ\text{E}$  Time. a) 1) Critical Ordinary-Wave Frequency of F2-, F1-, and E-Layers in Megahertz; 2) Limiting Frequencies of  $E_s$ ; 3) Minimum Frequencies; 4) Median Values of  $f_oF2$ ,  $f_oF1$ , and  $f_oE$  for Control Days; L) Absence of Distinct Inflection Between F1- and F2-Layers; b) 1) Effective Height  $h'$  of F2- and E-Layers in Kilometers; 2)  $h'F1$ ; 3)  $h'E_s$ ; 4)  $h'$  Smaller than Measured; 5) Median  $h'F2$  for Control Period.

The nighttime values of  $f_oF2$  on 23 November were higher than those of the control period. At about the time of maximum obscuration, the critical frequencies of the F2-layer first increased and then began to decline, reaching a minimum 15 minutes before the end of the eclipse.

A rise in the critical frequency was registered during the first half of the day after the eclipse, with substantial fluctuations of  $f_oF2$  from hour to hour. Before the end of the eclipse and at noon, the ionospheric records showed stratifications in the F2(G)-region. During the latter half of the day,  $f_oF2$  again varied from hour to hour, but differed only slightly from the critical frequencies for the control period. The evening ionization maximum was observed from 15 to 16 hours. The effect of the eclipse was also manifested in the F1-layer in the form of a critical-frequency drop after maximum phase.

/41

Effective heights. The minimum effective reflection heights of the E-layer on 23 November 1965 (Fig. 1b) were greater by 20 km than those measured in the second phase of the eclipse. The heights of the F1- and F2-layers differed little from the average values for the control days. To judge from the altitude variation, separation of the F-region occurred during the second half of the eclipse. During this time, the height of the F2-layer decreased twice: at 8 hours and at 8 hours 45 minutes. The height values were greatest when the ionization at the maximum of the F2-layer (critical frequency) reached its minimum. The heights of the F1-layer varied in antiphase with  $h'F2$ .

/42

The true heights were calculated from the ionospheric records by Baden's method, using a Minsk-1 computer with semiautomatic input of the coordinates of the  $f_0 = \phi(h')$  curve.

We see from the  $N(h)$  profiles (Fig. 2) that, depending on the time of day and the height of the level under consideration, the electron concentration  $N$  varies over a broad range: maximum variations at 160 and 180 km and a lag with respect to the maximum phase of the eclipse were noted. At heights below 150 km, the ionization remains constant for a certain time after maximum phase and then increases.

TABLE 1

Time, hours and minutes	$y_m$ , km		$h_{max}$ , km		$N_{max}$ , $10^4 \cdot \text{cm}^{-3}$		$n$ , $10^{10} \text{ cm}^{-3}$	
	1	2	1	2	1	2	1	2
7.00	58.1	74.4	233.4	234.3	12.4	15.8	156.4	203.9
7.15	70.1	77.3	231.8	223.1	15.6	22.9	195.2	267.9
7.30	56.2	64.9	197.5	205.9	16.6	23.2	187.5	261.1
7.45	93.6	72.3	219.2	207.2	14.0	23.7	241.0	272.9
8.00	80.6	67.5	207.8	200.0	13.4	27.0	197.5	301.0
8.15	66.4	71.2	194.5	198.1	12.5	25.6	176.2	300.4
8.30	99.6	90.5	224.2	214.2	15.4	26.2	279.4	350.3
8.45	111.4	89.7	212.5	112.0	17.3	26.7	321.5	371.6
9.00	97.1	74.5	205.6	203.7	17.7	28.8	280.2	350.0
9.15	79.1	83.5	199.5	206.9	17.4	28.0	272.5	373.6

After 8 hours,  $N$  begins to increase, doing so more rapidly the closer the particular level is to the layer maximum. At 8 hours 30 minutes, the electron density at the maximum of the F2-layer decreases; this is explained by the stratification effect in the F2-layer. The electron concentration at this level decreased by almost half during the second half of the eclipse.  $N(t)$  also varied rapidly at the beginning and end of the eclipse.

Table 1 presents the calculated true half-thicknesses of the F-region ( $y_m$ ), maximum heights ( $h_{max}$ ), maximum electron densities ( $N_{max}$ ), and total electron contents ( $n$ ) for 23 November 1965 (columns 1) and, for comparison, for the control days (columns 2). To judge by the manner in which the  $f_0nh'$  parameters vary, the true values of  $N_{max}$  and  $n$  were, as we should expect, lower on the

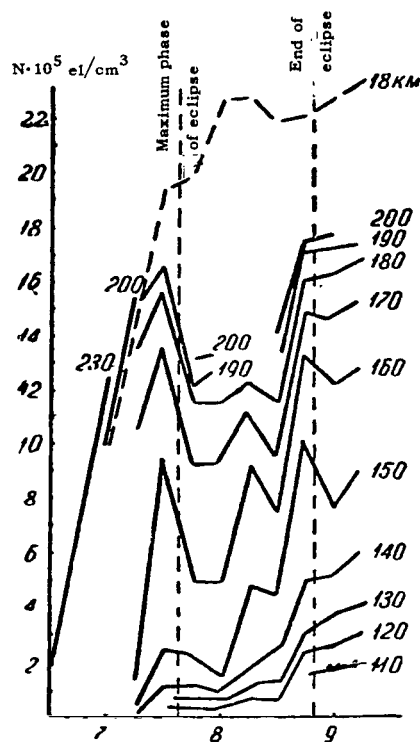


Figure 2. Distribution of Electron Concentration  $N$  at 10-km Intervals of True Height for 23 November 1965, 75°E Time; the Dashed Curve Indicates the  $N$  on the Control Days.

day of the eclipse than on the control days. The half-thickness increase at the time of maximum phase was also different. This process was accompanied by a decrease in electron density at the layer maximum and a decline in the total electron content.

Minor fluctuations of the true F2-layer parameters were also brought out between runs of measurements, but they are obviously unrelated to the solar eclipse. The recombination coefficient was calculated only after the maximum phase of the eclipse. The recombination coefficient for the true height (180 km) was  $\alpha = 1.0 \cdot 10^{-9}$ .

This account indicates the difficulty of ascertaining the effect of the 23 November 1965 solar eclipse on the ionosphere, since the period of the eclipse coincided with the nonsteady processes observed during the hours around sunrise.

However, the following ionospheric patterns were brought out during the eclipse: the critical frequencies of the F1- and F2-layers decreased, confirming the photon-ionization hypothesis; the effective height of the F2-layer varied in antiphase with  $f_oF2$ , confirming the existence of recombination; the effective height of the F1-layer varied little during the eclipse. Re-combination may not have been responsible for the decrease in F1-layer ionization; the eclipse influenced stratification of the F-region, retarding it; the critical frequencies of the F2-layer varied substantially from session to session. At times, stratification from F2 took place during periods of declining  $f_oF2$  owing to the interaction of the lunar tidal motions with the geomagnetic field, with the resulting vertical charge redistribution; during the eclipse, such parameters as  $y_m$ ,  $h_{max}$ , etc. varied insignificantly, apparently because of the ionosphere's inertia; it is evident from analysis of the  $N(t)$  curves that the layer at 180 km is most sensitive to ionizing radiation; the rapid changes of  $N(t)$  during maximum phase and at the end of the eclipse can be explained by the nonuniform distribution of the ionizing radiation over the surface of the solar disk.

/44

APPARATUS FOR INVESTIGATION OF THE AMPLITUDE-FREQUENCY  
RESPONSE OF THE IONOSPHERIC-SCATTERING CHANNEL

/45

V.M. Krasnov and A.F. Yakovets

ABSTRACT: Equipment for investigation of the amplitude-frequency response of the ionospheric-scattering channel is described. The first experimental results are reported.

The ionospheric-scattering communications channel is a channel with multipath signal propagation. This property results in different transmission coefficients at different frequencies or, in other words, nonuniformity of the channel's amplitude-frequency response (AFR). The nonuniformity is expressed quantitatively in terms of the ratio between the amplitudes at the ends of the frequency band under study. AFR nonuniformity is a random function of frequency and time, and is therefore described statistically. AFR nonuniformity functions have been obtained theoretically [1, 2] for channels at whose outputs the signal-amplitude envelope has a Rayleigh or generalized-Rayleigh distribution. By analogy with channels having constant parameters, a passband notion has been introduced for channels with variable AFR. This is the frequency band in which the AFR nonuniformity does not exceed a specified value with stated probability.

It is shown in [2] that the form of the AFR can be improved substantially and the channel passband broadened by linear addition of uncorrelated signals in front of the detector. The possibility of such improvement is very easily demonstrated by qualitative arguments. It is known that the amplitude of a signal with frequency  $f_0$  at the output of the ionospheric-scattering channel is a stationary ergodic process on a time segment ranging into the tens of minutes. This means that any realization of the process is characterized by the same statistical parameters during the course of this time. By "realization" we mean the amplitude envelopes at points separated in space. Adding  $N$  spatially separated signals after first reducing them to the same phase, we find that for large enough  $N$ , the resulting amplitude will tend at any point in time to the product of  $N$  by the average amplitude value obtained for one realization. A similar result can be obtained at any other frequency near  $f_0$ .

/46

Thus, we obtain a uniform AFR over a broad frequency band. The only limit on bandwidth is the fact that it is impossible to

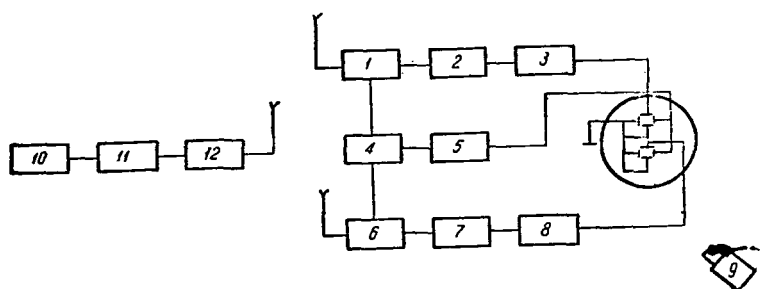


Figure 1. Block Diagram of Apparatus for AFR Measurement. 1) Receiver; 2) Logarithmic amplifier; 3) dc amplifier; 4) Reactive element; 5) Sweep oscillator; 6) Receiver; 7) Logarithmic amplifier; 8) dc amplifier; 9) Motion-picture camera; 10) 50-Hz generator; 11) Modulator; 12) Transmitter.

effect linear amplitude addition in a broad band because of the differences between the instantaneous phase-response characteristics of the channel for different points in space.

A theory of AFR nonuniformity has been elaborated [1, 2] for application to tropospheric-scattering channels and tested experimentally [3] on results obtained for tropospheric propagation. We have developed equipment for investigation of the AFR of the ionospheric-scattering channel.

AFR recording equipment for single and double reception (Fig. 1). Transmitter frequency was varied sinusoidally at 50 Hz in the band  $f_0 \pm 3$  kHz. The scanning frequency (50 Hz) was so selected that the fixed-frequency signal amplitude would remain constant during one scan of the frequency range. The receiving unit consists of two identical amplifier channels with a 1-kHz IF bandwidth. The frequency of the transmitter's receiver second local oscillators is varied in the same way to track the frequency of the received signal. Double reception of the transmitted information requires a unit that compares the phases of the signals that have passed through the different channels, a unit that controls the phase of one of the channels, and an adder in which coherent signals are added. However, these devices can be omitted, to the considerable simplification of the apparatus, in an experiment to determine the AFR with double reception. In this case, the amplitudes of the separate channels are added during reduction of the results, when the images of the AFR for the individual channels have already been fixed on film.

/47

Schematic diagram. After preamplification in a type R-250M receiver, the second-intermediate-frequency signal proceeds to the logarithmic-amplifier block. The amplifier block (Fig. 2)

consists of an intermediate-frequency amplifier, a detector, a logarithmic network, a dc amplifier, and a voltage stabilizer. The two-stage intermediate-frequency amplifier is built around tubes T16-T17 in a selective-gain circuit with resonance networks, and provides further voltage amplification of the signal incoming from the output of the receiver's second intermediate-frequency amplifier. The first stage used a 6Zh3P pentode with a large static amplification factor. Linearity of the amplitude characteristic is ensured by use of an output-stage tube with a linear grid-plate characteristic and deep negative voltage feedback bridging both stages (networks R57, R99, R98, R55). To obtain a high gain from a comparatively small power-source voltage, the IFA output stage has the circuit autotransformer-connected into the plate circuit of tube T17. The series resonance network (T3, C63, C64, C65) is used for the same purpose.

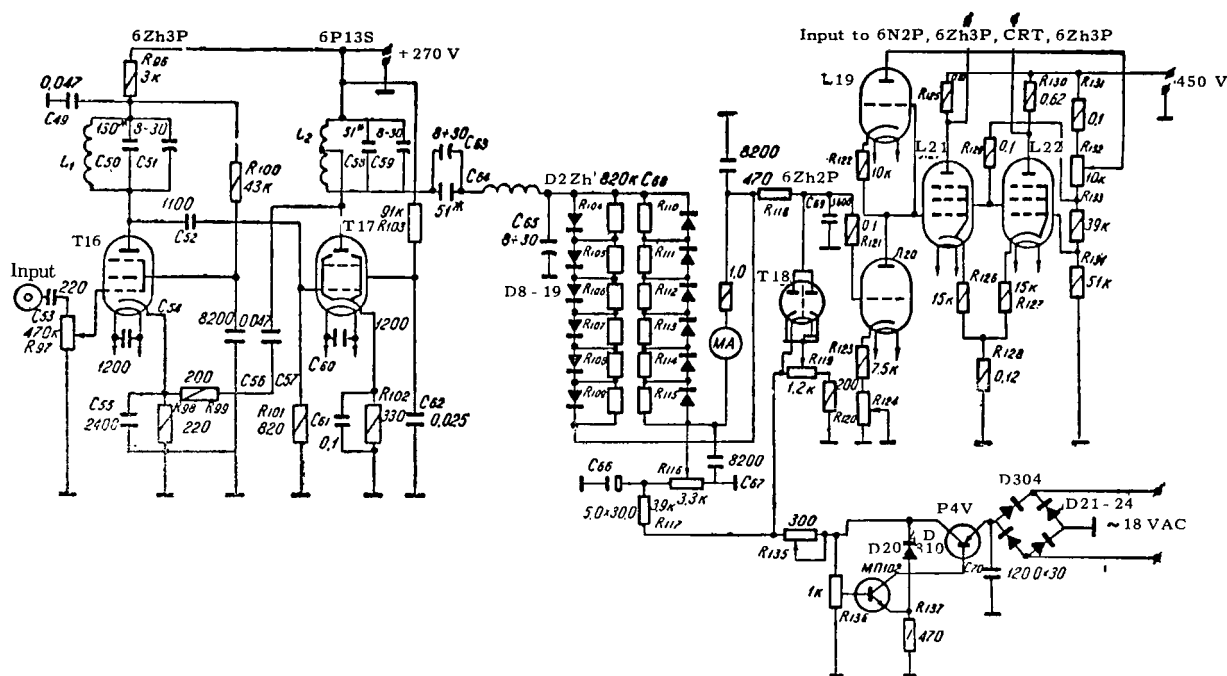


Figure 2. Logarithmic Amplifier Block. The Resistors and Capacitors Marked with the Asterisk are Matched During Adjustment.

The detector serves to double the detected signal voltage arriving from the output stage of the intermediate-frequency amplifier. Its voltage-doubler circuit operates on the voltages

added across the load, whose circuit contains a microammeter. To obtain a linear amplitude characteristic in the low-voltage range, a constant positive voltage from the stabilized power source is applied to the diodes.

The logarithmic network converts the voltage picked off the detector load from linear to logarithmic. The logarithmic unit is built around resistor R-118 and the 6Kh2P double diode Tl8. The logarithmic mode is set up by regulating the bias voltage in the cathode circuit of the 6Kh2P tube. To eliminate zero drift, the filament and bias supplies to the 6Kh2P tube are from the stabilized power source.

The dc amplifier further amplifies the signal arriving from the output of the logarithmic network. The two-stage dc amplifier, whose output goes to the plates of the cathode-ray tube, is built around tubes T19-T22. Its first stage is a balanced series circuit based on a 6N2P double triode with a high static amplification factor, and its second stage is a parallel balanced circuit built around 6Zh3P economy pentodes. The variable resistor R-124 serves for selection of the optimum drift compensation. The constant component of the first-stage output voltage is compensated by the voltage drop across resistors R-133 and R-134. In addition, resistors R-126 and R-127 provide negative feedback that reduces the influence of tube-parameter scatter on stage performance. Resistor R-28 is a cathode-coupling element, and variable resistor R-132 serves to shift the position of the beam on the oscilloscope screen. The stabilized power source is semiconductorized. The rectifier is a bridge-circuit type (diodes D21-D24). The high-rating capacitor C70 smooths the ripple of the rectified voltage. The P4V transistor is the controlled element of the voltage-stabilization network, the MP102 transistor is the controlling element, and network D20/R-137 is the sensing element. The function of variable resistor R-136 is to set the initial operating point of the MP102 transistor. /49

The receiver can track transmitter frequency precisely for long periods only when quartz master oscillators are used at the transmitting and receiving ends; 10-kHz crystals were selected for this purpose. To obtain sine waves with a frequency of 50 Hz, the 10 kHz was pulse-divided by a factor of 200 and the sine waves were separated in a narrow-band filter. The initial receiver lock-on to the transmitter frequency is accomplished by phase-tuning of the master oscillator with a kipp relay.

The horizontal-sweep block (Fig. 3) consists of a quartz master oscillator, a bilateral limiter, a bank of frequency dividers, a kipp relay, a square-wave generator, a normalizing stage, a narrow-band amplifier, and phase-inverter and output amplification stages. The self-excited quartz oscillator whose function is to generate a 10-kHz sinusoidal voltage of highly stabilized frequency and amplitude is built around tube T1 in a /51





The frequency dividers are built around tubes T3-T6 in a slave-multivibrator circuit. To preserve stability of the pulse repetition frequency, the slave multivibrators are activated by the leading edges of the triggering pulses. The division ratios of the slave multivibrators are 1:5, 1:5, 1:4, and 1:2, respectively. The function of the kipp relay is to provide variable delay of the leading edges of the pulses incoming from the divider bank. The kipp relay is built around tube T7, also in a slave-multivibrator circuit. By changing the wiper position on potentiometer R-51, we change the grid bias of tube T7 and, accordingly, the current flowing through the left half of the tube when it is open, thereby increasing or decreasing the discharge time of capacitor C24 appropriately and, consequently, also the duration of the pulses put out by the multivibrator.

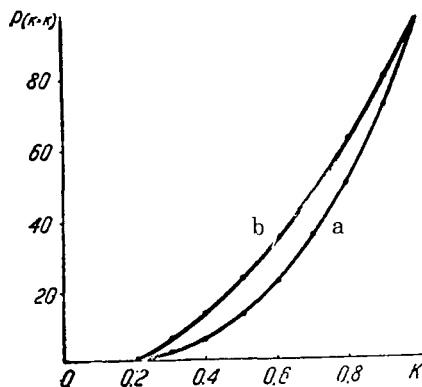


Figure 4. Distribution of AFR Nonuniformity for Frequency Band: a) 1 kHz; b) 2 kHz. The curves illustrate averaged results from eight measurement runs.

The square-wave generator, whose function is to generate meander-type oscillations, is built around tube T8 in a slave-multivibrator circuit. It is tripped by the trailing edges of the pulses incoming from the kipp relay. The normalizing stage (T-9) serves for amplitude normalization of the pulses coming from T-8. Limiting is by plate-current cutoff at the bottom and by plate-current saturation at the top. A sine wave with a frequency of 50 Hz is separated in the narrow-band amplifier from the meander of the same frequency. The amplifier is based on tubes T-10-T-11 with frequency-selective RC amplifiers and a double-T bridge in the feedback circuit (R78-R80, C37-C39). Negative current feedback (resistor R71) is used in the circuit to stabilize the amplitude of its output voltage. The signal

is fed to the selective amplifier through cathode follower T-10. From the output of the narrow-band amplifier, the sine wave goes to the phase-inverter stage T-12, then to the output stage T-12 [sic], and then to the output stage T-13-T-14. The cathode of T-14 is supplied from a negative voltage source to secure the necessary sweep on the CRT screen without voltage overloading of the tubes.

The reactive element that controls the second local oscillator frequency in the R-250M receiver is based on tube T-15. Capacitor C47 is a high-frequency blocking capacitor. Control capacitor C48 is connected to the local-oscillator circuit by means of diodes T-15. The time for which the diodes are alternately

/52

unblocked and the control capacitor is connected to the local-oscillator circuit depends on the value of the voltage applied to the diodes. Thus, the capacitance connected to the circuit can be varied by varying the amplitude of the modulating voltage.

In February 1968, we made several AFR measurements at 18.695 MHz on a path 1400 km long during the night, when this frequency exceeded the maximum useful reflected frequency. Probability distributions were obtained for the AFR nonuniformity for 1- and 2-kHz frequency bands (Fig. 4).

#### REFERENCES

1. Gusyatinskiy, I.A. Bandwidth and Transient-Noise Power in Radio Communication by Tropospheric Scattering. "Elektrosvyaz'," 1959, No. 4.
2. Nemirovskiy, A.S. Transmission Bandwidth in Single and Diversity Reception of USW Signals with Long-Range Tropospheric Propagation. "Elektrosvyaz'," 1961, No. 5.
3. Gusyatinskiy, I.A. and Nemirovskiy, A.S. An Experimental Study of Passbands in Single and Diversity Reception of Tropospheric-Scattering Signals. "Elektrosvyaz'," 1964, No. 7.

A METHOD OF INVESTIGATING THE PHASE-RESPONSE  
CHARACTERISTIC OF THE IONOSPHERIC-SCATTERING  
COMMUNICATIONS CHANNEL

/53

A.F. Yakovets

ABSTRACT: A method is proposed for measuring the fluctuations of the phase difference between vibrations at different frequencies that result from fluctuations in the scattering properties of the medium through which the wave is propagated. The measurement equipment is described.

It is known that the ideal communications channel, which preserves the original form of the transmitted message, has a uniform amplitude-frequency response (AFR) and a linear phase-response characteristic (PRC). Deviations of the characteristics from the ideal distort the signal. To evaluate signal distortion, it is necessary to investigate the channel's AFR and PRC experimentally. The PRC of multipath channels, which include tropospheric and ionospheric scattering channels, are statistical in nature. We can speak of some particular PRC form only within the limits of a time segment shorter than the time-correlation radius of the phase fluctuations. The probability distribution function of the fluctuations in the phase difference between adjacent frequencies becomes the principal parameter determining the PRC. With consideration of these properties of the PRC, we propose a method for measuring the fluctuations of the phase difference between adjacent frequencies.

Two vibrations, one at a frequency exactly twice the frequency of the other, are transmitted through a medium whose scattering properties are time-variable (Fig. 1, a and b). With a constant distance between the receiver and transmitter and constant scattering properties of the medium, the phase difference between the beginning of the positive half-waves at frequency  $\Omega$  and the beginning of every other positive half-wave of frequency  $2\Omega$  remains constant in time. Fluctuations in the scattering by the medium result in fluctuations of this phase difference. Henceforth, in speaking of a change in the phase difference between different frequencies, we refer to the changes caused by the scattering in the medium, as distinct from the changes governed by the difference  $\Delta\Omega$  between the frequencies being compared. The method described is applicable to the ionospheric-scattering channel.

/54

An amplitude-modulated wave arrives at the input of the ionospheric-scattering channel. The spectrum of this wave consists of a carrier  $u_1 = A_1 \sin \omega t$  and two side frequencies  $u_0 = A_0 \sin(\omega - \Omega)t$  and  $u_2 = A_2 \sin(\omega + \Omega)t$ .

After passage through the channel, each component has acquired its own phase lead:  $\phi_1$ ,  $\phi_2$ , and  $\phi_3$ , respectively. We shall be interested in the phase shift  $\phi_0 - \phi_1$  or  $\phi_2 - \phi_1$ . To measure these quantities, the incoming signal is passed through filters tuned to different spectral components. Then the carrier and one of the side frequencies are mixed, and the modulating frequency  $\Omega$  is separated at the mixer output:  $\sin(\omega t + \phi_1) \sin[(\omega - \Omega)t + \phi_0] = 1/2[\cos(\Omega t + \phi_1 - \phi_0) - \cos(2\omega t - \Omega t + \phi_0 + \phi_1)]$ . The side frequencies are mixed in the other mixer:  $\sin[(\omega + \Omega)t + \phi_2] \sin[(\omega - \Omega)t + \phi_0] = 1/2[\cos(2\Omega t + \phi_2 - \phi_0) - \cos(2\omega t + \phi_2 + \phi_0)]$  and the doubled modulating frequency is separated. The doubled frequency is then divided by two

to obtain  $\cos(\Omega t + \frac{\varphi_2 - \varphi_0}{2})$ . Thus, we have two audio-frequency waves:  $\cos(\Omega t + \phi_1 - \phi_0)$  and  $\cos(\Omega t + \frac{\varphi_2 - \varphi_0}{2})$ , the phase difference between which is

$$\frac{1}{2}[(\varphi_2 - \varphi_1) + (\varphi_0 - \varphi_1)].$$

This method is similar to the phase-invariant method suggested for investigation of the scattering of ultrasound [1]. The same method was used in a study of ionospheric electron concentration [2]. In the phase-invariant method, three spectral lines are also transmitted through the medium to be studied. Then the carrier is mixed with the lower and upper side frequencies. The result is two modulating-frequency vibrations with phases  $\phi_2 - \phi_1$  and  $\phi_1 - \phi_0$ . The phase difference between these vibrations  $2\theta = \phi_0 + \phi_2 - 2\phi_1$  is twice the value of the phase invariant. The distributions of  $\phi_2 - \phi_1$  and  $\phi_0 - \phi_1$  are the same, and the coefficient of correlation between these quantities can be found. Once we know the correlation coefficient, it is simple

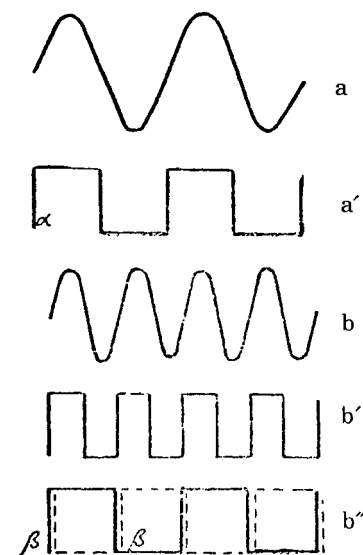


Figure 1. Diagrams of Voltages at Outputs of: a) Mixer  $M_2$ ; a') Limiter; b) Mixer  $M_1$ ; b') Limiter-amplifier LA; b'') Divider in two operating modes (solid line and dashed line).

to establish the relation between the statistical distribution parameters of the sum and the summands. For example, the variance

$$2\sigma_{\phi_2 - \phi_1}^2 = \frac{\sigma_{\phi_2 - \phi_1}^2 + (\sigma_{\phi_0 - \phi_1})^2}{2(1+R)},$$

where  $R$  is the correlation coefficient between  $\phi_2 - \phi_1$  and  $\phi_0 - \phi_1$ .

Having measured the phase fluctuations and constructed the integral distribution curve of  $\Delta\phi$  for frequencies separated by  $\Delta f$ , it is necessary to determine how accurately this curve describes the fluctuations of the phase difference between different combinations of frequencies in the band  $\Delta f$ , i.e., how accurately the nonuniformity of the PRC in a given frequency band can be described by the statistical parameters of the fluctuation of the phase difference between the frequencies at the ends of this band. The natural solution to this problem is to break up the frequency band into segments and determine the  $R$ -dimensional distribution function of the phase differences between the various frequencies. To begin, let us divide the frequency band  $\Delta f$  into two equal parts. Let the phase of the lower frequency be  $\phi_0(t)$ , that of the middle frequency  $\phi_1(t)$ , and that of the upper frequency  $\phi_2(t)$ . We shall denote the correlation coefficients between the phases of adjacent frequencies by  $\rho$ , and those between the end-frequency phases by  $R$ . We shall assume that a substantial constant component is present in the scattered signal, so that the distribution of the signal's phases is close to normal. This condition is often satisfied for ionospheric and tropospheric scattering.

Then the variances  $\sigma_{\phi_0}^2$ ,  $\sigma_{\phi_1}^2$ , and  $\sigma_{\phi_2}^2$  of the phases will be the same, depending on the ratio of the constant to the random components of the signal, and the variances of the phase differences will take the form

$$\sigma_{\phi_2 - \phi_0}^2 = 2\sigma_{\phi_0}^2(1 - R); \quad \sigma_{\phi_2 - \phi_1}^2 = 2\sigma_{\phi_0}^2(1 - \rho).$$

The phase differences are normally distributed with zero mean, and we may therefore write the coefficient of correlation between them as

$$r = \frac{(\phi_2 - \phi_0)(\phi_1 - \phi_0)}{\sigma_{\phi_2 - \phi_0} \sigma_{\phi_1 - \phi_0}} = \frac{\phi_1 \phi_2 - \phi_0 \phi_1 - \phi_0 \phi_2 + \phi_0^2}{2\sigma_{\phi_0}^2 \sqrt{(1-\rho)(1-R)}},$$

$$r = \frac{1}{2} \sqrt{\frac{1-R}{1-\rho}}. \quad (1)$$

Now, knowing the correlation coefficient between the phase differences  $\Delta\phi_1$  and  $\Delta\phi_2$ , we can compute the integral two-dimensional distribution function:

$$P(|\Delta\varphi_1| \leq \Phi, |\Delta\varphi_2| \leq \Phi) = \int_{-\Phi}^{\Phi} \int_{-\Phi}^{\Phi} w_2(\Delta\varphi_1, \Delta\varphi_2) d(\Delta\varphi_1) d(\Delta\varphi_2). \quad (2)$$

Here  $w_2(\Delta\phi_1, \Delta\phi_2)$  is the two-dimensional differential distribution function and equals

$$\frac{1}{2\pi\sigma_{\Delta\varphi_1}\sigma_{\Delta\varphi_2}\sqrt{1-r^2}} \exp\left\{-\frac{1}{2(1-r^2)}\left[\frac{\Delta\varphi_1^2}{\sigma_{\Delta\varphi_1}^2} - 2r\frac{\Delta\varphi_1\Delta\varphi_2}{\sigma_{\Delta\varphi_1}\sigma_{\Delta\varphi_2}} + \frac{\Delta\varphi_2^2}{\sigma_{\Delta\varphi_2}^2}\right]\right\}. \quad (3)$$

The evaluation of this integral is given in the appendix. Let us examine the behavior of the curve in a particular example:

$$P(|\Delta\varphi_1| \leq \Phi, |\Delta\varphi_2| \leq \Phi).$$

We take the experimental curve of the frequency-correlation coefficient as a function of frequency separation from [3]. For separation  $\Delta f = 4$  kHz, the correlation coefficient  $R = 0.5$ , and for  $\Delta f = 2$  kHz,  $\rho = 0.84$ . We use Formula (1) to calculate the correlation coefficient between the phase differences ( $r = 0.88$ ).

Calculated values of the integral (3) for various parameters  $\Phi/\sigma_{\Delta\phi_2}$  are presented graphically in Fig. 2 (curve b). Curve a in the same figure is the probability integral

$$P(|\Delta\varphi| \leq \Phi) = \frac{2}{\sqrt{2\pi}} \int_0^{\Phi/\sigma} \exp\left\{-\frac{x^2}{2}\right\} dx.$$

The probability  $P(|\Delta\phi| \leq \Phi)$  is expressed as a percentage and determines the time for which the phase difference remains in the range  $(-\Phi, +\Phi)$ . On comparing the curves, we note that the maximum divergence between them is observed at small values of the limits  $\Phi < 0.25 \sigma_{\Delta\phi_2}$ . With increasing  $\Phi$ , the difference  $P(|\Delta\phi| \leq \Phi) - P(|\Delta\phi_1| \leq \Phi, |\Delta\phi_2| \leq \Phi)$  decreases, to vanish at  $\Phi/\sigma_{\phi_2} \approx 1.5$ . The coincidence of the curves at the point  $\Phi \approx 1.5 \sigma_{\phi_2}$  becomes clear when we remember that an increase in the measurement limit  $\Phi$  to  $1.5 \sigma_{\Delta\phi_2}$  means an increase in the limit to  $2.4 \sigma_{\Delta\phi_1}$  for  $|\Delta\phi_1|$ .

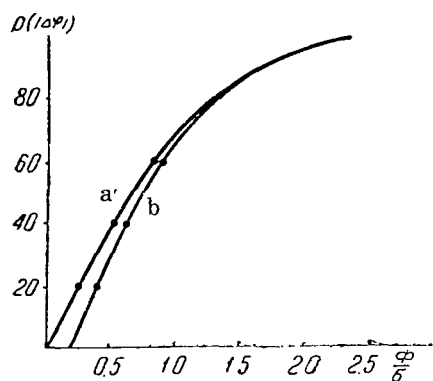


Figure 2. One-Dimensional (a) and Two-Dimensional (b) Phase Difference Probability Distribution Functions.

It is then necessary to divide the band  $\Delta f = 2$  kHz into two parts in order to improve the statistical picture of the phase-difference fluctuation in the band  $\Delta f = 4$  kHz. In this case,  $R = 0.84$  and  $\rho = 0.96$ . If  $r$  is calculated by Formula (1), we have  $r \approx 1$ . Consequently, the phase differences between the frequencies  $f_0$  and  $f_0 + 1$  kHz and  $f_0$  and  $f_0 + 2$  kHz fluctuate synchronously. Thus, the integral distribution function of the phase difference between frequencies  $f_0$  and  $f_0 + 2$  kHz is valid over the entire 2-kHz band.

Thus, in order to calculate the integral distribution function of the phase difference in a frequency band between all possible frequency combinations within this

band, it is sufficient to calculate the two-dimensional distribution function of the phase difference between the frequencies bounding this band and between one of the end frequencies and the center frequency. This conclusion was derived for a band bounded by frequencies whose correlation coefficient equaled 0.5.

#### DESCRIPTION OF APPARATUS

The signal — a carrier modulated by an audio frequency — is amplified in receiver R and fed after conversion to filters  $F_1$ ,  $F_0$ , and  $F_2$ , which are tuned to the converted carrier and lower and upper side frequencies, respectively (Fig. 3). The selected frequencies go to mixers  $M_1$  and  $M_2$ . The upper side and carrier are mixed in mixer  $M_2$  to yield the difference frequency  $\Omega$ .

The upper and lower side frequencies are mixed in mixer  $M_1$ . The frequency  $2\Omega$  is separated at the mixer output. The signal with frequency  $2\Omega$  goes to limiter-amplifier LA for conversion of the sine wave to square pulses. After division by 2 by a flip-flop (2), the pulses (Fig. 1, b") go to the input of phasemeter  $\Delta\phi$ , whose other input receives the frequency  $\Omega$ . The phasemeter measures the phase difference between the comparison signals by measuring the time interval between the leading edges of the  $\alpha$  and  $\beta$  pulses.

Note should be taken of one peculiarity of the division circuit. Depending on the state of the flip-flop, a positive voltage drop across its output may result from either the first or the second pulse (Fig. 1). For this reason, two phase meter readings



differing by  $180^\circ$  may correspond to the same value of the measured phase difference.

The flip-flop may misfire as a result of occasional deep fading of the signal, at which times no signal is impressed on the flip-flop input. In such cases, the phase-difference fluctuations will obviously group about two values separated by  $180^\circ$ . This does not give rise to any complications in reduction of the results, since it is sufficient to shift one of the distributions obtained through  $180^\circ$  to obtain the actual distribution.

The functioning of the apparatus was checked with a signal reflected from the sporadic E-layer on a 1400-km path. The 18.5-MHz frequency was modulated by a frequency of 1 kHz. The phase difference between frequencies separated by 1 kHz experienced slow fluctuations with periods from 30 seconds to 2 minutes. The amplitude of the fluctuations ranged up to  $4^\circ$ .

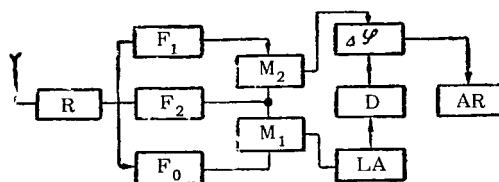


Figure 3. Block Diagram of Apparatus for Measurement of Channel PRC.  $F_0$ ,  $F_1$ ,  $F_2$ ) Filters; R) receiver;  $M_1$ ,  $M_2$ ) mixers; LA) limiter-amplifier; D) divider;  $\Delta\phi$ ) phase meter; AR) automatic recorder.

## APPENDIX

### EVALUATION OF INTEGRAL (2)

A method of evaluating iterated integrals of the form

$$I = \int_0^\infty dx_1 \int_0^\infty dx_2 \exp(-x_1^2 - 2ax_1x_2 - x_2^2)$$

is given in [4]. However, solution of the integral taken in finite limits is of independent interest and is important for many applications. An integral of the form (2) represents a volume bounded at the top by the surface  $\omega_2(\Delta\phi_1, \Delta\phi_2)$ , and at the sides by the planes  $\Delta\phi_1 = \pm\Phi$  and  $\Delta\phi_2 = \pm\Phi$ . Since this volume is divided into two equal parts by the plane  $\Delta\phi_1 = 0$ , Integral (2) can be rewritten

$$I = \frac{1}{\pi \sigma_{\Delta\phi_1} \sigma_{\Delta\phi_2} \sqrt{1-r^2}} \int_0^\Phi d(\Delta\phi_1) \int_{-\Phi}^\Phi d(\Delta\phi_2) \exp \left\{ -\frac{1}{2(1-r^2)} \left[ \frac{\Delta\phi_1^2}{\sigma_{\Delta\phi_1}^2} - \frac{\Delta\phi_1 \cdot \Delta\phi_2}{\sigma_{\Delta\phi_1} \sigma_{\Delta\phi_2}} + \frac{\Delta\phi_2^2}{\sigma_{\Delta\phi_2}^2} \right] \right\}.$$

We introduce the substitution of variables

$$\frac{\Delta x_1^2}{2(1-r^2)\Delta x_1^2} = x_1^2 \quad \text{and} \quad \frac{\Delta x_2^2}{2(1-r^2)\Delta x_2^2} = x_2^2.$$

The integral assumes the form

$$I = \frac{2}{\pi} \sqrt{1-r^2} \int_0^{X_1} dx_1 \int_{-X_2}^{X_2} dx_2 \exp \{-x_1^2 - 2rx_1x_2 + x_2^2\}.$$

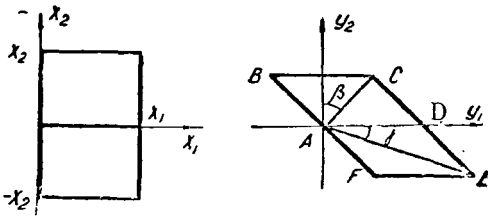


Figure 4. Regions of Integration with Respect to the Variables  $x_1$ ,  $x_2$ , and  $y_1$ ,  $y_2$ .

The limits of integration are expressed in terms of  $\Phi$ :

$$X_1 = \frac{\Phi}{2(1-r^2)\Delta x_1^2}; \quad X_2 = \frac{\Phi}{2(1-r^2)\Delta x_2^2}.$$

To reduce the expression in the exponent to a sum of squares, we convert to the new variables

$$x_1 = y_1 + aD^{-1/2}y_2 \\ x_2 = y_2 D^{-1/2}.$$

Here  $a = -r$  and  $D = 1 - a^2$ . The Jacobian of the transformation is  $\frac{D(x_1, x_2)}{D(y_1, y_2)} = D^{-1/2}$ . With the new variables, the integral equals

/60

$$I = \frac{2}{\pi} \int_{-X_2 D^{1/2}}^{X_2 D^{1/2}} dy_2 \int_{aD^{-1/2}y_2}^{X_1 + aD^{-1/2}y_2} dy_1 \exp \{-y_1^2 - y_2^2\}.$$

To reduce this integral to an ordinary definite integral, we convert to the polar coordinates  $\rho$  and  $\theta$ , which are related to  $y_1$  and  $y_2$  by  $y_1 = \rho \cos \theta$ .

$$y_2 = \rho \sin \theta, \quad dy_1 dy_2 = \rho d\rho d\theta.$$

The region of integration (Fig. 4) is broken up into four triangles and the integration performed separately for each of them.

1. In triangle ABC

$$\frac{\pi}{2} - \beta \leq \theta \leq \arctg aD^{-1/2}, \quad \beta = \arctg \frac{D'^{1/2}}{\frac{X_1}{X_2} - |a|},$$

$$0 \leq \rho \leq \frac{X_2 D'^{1/2}}{\sin \theta}.$$

2. In triangle ACD

$$0 \leq \theta \leq \frac{\pi}{2} - \beta,$$

$$0 \leq \rho \leq X_1 \frac{\sin(\pi - \arctg aD^{-1/2})}{(\pi - \arctg aD^{-1/2} - \theta)} = b(\theta).$$

3. In triangle ADE

/61

$$\gamma \leq \theta \leq 0 \quad \gamma = \arctg \left\{ -\frac{D'^{1/2}}{\frac{X_1}{X_2} + |a|} \right\};$$

$$0 \leq \rho \leq X_1 \frac{\sin(\arctg aD^{-1/2})}{\sin(\pi - \arctg aD^{-1/2} - \theta)} = c(\theta).$$

4. In triangle AEF

$$\arctg aD^{-1/2} \leq \theta \leq \gamma;$$

$$0 \leq \rho \leq \frac{X_2 D'^{1/2}}{\cos(\pi/2 + \theta)}.$$

The general form of the integral after evaluation of the inner integrals will be

$$\begin{aligned} I = & \frac{1}{\pi} \left\{ \int_{\pi/2 - \beta}^{\arctg aD^{-1/2}} d\theta \left[ 1 - \exp - \left( \frac{X_2 D'^{1/2}}{\sin \theta} \right)^2 \right] + \right. \\ & + \int_0^{\pi/2 - \beta} d\theta [1 - \exp - b^2(\theta)] + \int_{\gamma}^0 d\theta [1 - \exp - c^2(\theta)] + \\ & \left. + \int_{\arctg aD^{-1/2}}^{\gamma} d\theta \left[ 1 - \exp - \left( \frac{X_2 D'^{1/2}}{\cos(\pi/2 + \theta)} \right)^2 \right] \right\}. \end{aligned}$$

Subsequent evaluation of the resulting integrals is easily performed numerically.

## REFERENCES

1. Zverev, V.A. A New Method of Investigating the Scattering of Ultrasound. In: "Pamyati A. A. Andronova" (Memoirs of A.A. Andronov), Moscow, Izd-vo AN SSSR, 1955.
2. Ryzhov, Yu.A. and Yudin, O.I. On the Influence of Ionospheric Electron-Concentration Inhomogeneities on Certain Parameters of the Ionosphere. "Izv. vuzov, Radiofizika," 1962, No. 1.
3. Vetishev, Zh.N. and Nesterova, O.M. Determination of Frequency Band Transmitted Without Distortion in Ionospheric Scattering. Trudy SFTI, No. 45, Tomsk, 1964.
4. In: "Teoriya peredachi elektricheskikh signalov pri nalichii pomekh" (Theory of Transmission of Electrical Signals in the Presence of Noise), Moscow, IL, 1953.

RADIO-WAVE PROPAGATION AT FREQUENCIES EXCEEDING  
MUF-F2 IN THE SHORT-WAVE BAND

/62

Ya.F. Ashkaliyev and V.I. Bocharov

ABSTRACT: The results of measurements of field strength and signal/noise ratio on experimental ionospheric-scattering short wave radio links are presented. It is shown that the seasonal and diurnal variations of field strength are determined by features of the seasonal and diurnal variations of solar and meteoric activity. The role of the sporadic E-layer in propagation of short radio waves at frequencies exceeding MUF-F2 is noted. With 5 illustrations and 2 source citations.

Little study has been devoted to the natural contraction of the short-wave radio band during years of minimum solar activity and at night. It is shown in [1] on the basis of the operating frequencies actually used on radio communications trunk lines that the frequency spectrum allocated for short waves is only 60% utilized during the day and 40% utilized at night. Consequently, frequencies lower than recommended [2] (35-60 MHz) can be used on ionospheric-scattering links. Special research is required to establish the practical possibilities of building communications systems to work by ionospheric scattering in the short-wave range with conventional technical facilities. Such experimental studies have been made in the Ionosphere Sector of the Academy of Sciences of the Kazakh SSR on transmission paths of various lengths (1965-1966).

Experimental method and reduction of data. The studies were performed at middle latitudes on paths 1000, 1400, and 1650 km in length, and at frequencies of 16.170 and 18.340 MHz. Standard short-wave equipment was used at the transmitting and receiving stations. The transmitters operated in the carrier-frequency mode. The level of the radio-frequency voltage at the receiver input was determined by the substitution method. The standard was a signal from a G4-1A generator that had the same frequency as the transmitter carrier.

The signals on the three radio links were registered on paper tape by N-370 automatic recorders. The chart tape was advanced at a rate of 1.5 mm/sec. The average value  $E$  of the radio-frequency signal at the receiver input was evaluated as the median signal envelope level over two 10-minute measurement intervals

during each hour (00.05-00.15 and 00.50-00.01). Below we describe the basic features of the signal scattered on ionospheric inhomogeneities, as well as its diurnal and seasonal variations.

/63

General characteristics of the received signal. From the very first sessions during which signals were received at frequencies above the standard MUF of the F2-layer, a number of characteristic peculiarities were noted in the time variation of their envelope. On paths shorter than 2000 km, the manifestations of these peculiarities were as follows: rapid and deep variations of signal amplitude and, together with a component having rather stable fluctuation characteristics, as in the USW band, very strong surges with steep leading edges and comparatively slow decay. The appearance of these surges is accompanied by a marked Doppler frequency shift, which is manifested in the form of whistles of various tones in code reception. This is characteristic for reflected signals from dense layers of meteoric ionization in the lower ionosphere. Along with the records of signals scattered on electron-concentration inhomogeneities, we observe traces with very slow and comparatively shallow received-signal-amplitude variations. In most cases, such traces are accompanied by the appearance of a dense E-layer at the midpoint of the path.

Diurnal and seasonal variations of field strength. The signal-level traces for frequencies of 16.170 and 18.340 MHz on paths 1400 and 1650 km long were processed statistically to obtain the median values for each hour (Fig. 1).

Characteristically, field strength increases during the morning hours (09-10<sup>h</sup>) as a result of the changes in the critical frequency of the E-layer ( $f_oE$ ) during the course of the day, since scattered-signal field strength is proportional to  $f_oE^2$ . The minimum level is noted during the morning (07<sup>h</sup>). An evening minimum (19-20 hours) is characteristic for the USW band; it is shifted toward midnight (00-01 hours). This feature of the diurnal variation of the scattered signal is explained very nicely by features of the diurnal meteoric and solar activity variations. On comparing the diurnal-variation data for the signals on these links, we note that the morning minimum on the 1650-km path was deeper, indicating a substantial meteoric component in the received signal. A nocturnal maximum is observed on the 1400-km path, but to judge from the depth of the predawn minimum that follows it, the meteoric component does not predominate on this radio link. By comparison with the nocturnal maximum, the depth of the predawn minimum on the 1650-km path is 13 dB, while that on the 1400-km path is 2 dB. The maximum field-strength variations over the time covered by the measurements are 15 and 10 dB, respectively.

/64

As we see from Fig. 2, the field-strength maximum on the 1400-km path (18.340 MHz) occurs in July, like the maximum of

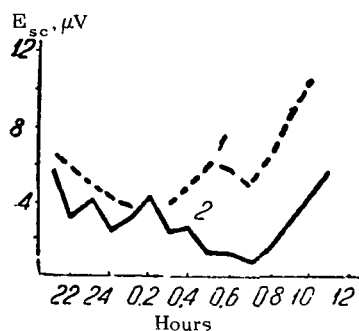


Figure 1. Signal Level as a Function of Time of Day. 1) 18 MHz; 2) 34 MHz.

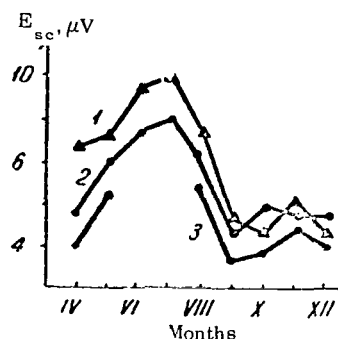


Figure 2. Seasonal Variations of median  $E_{sc}$ . 1) 18, 34 MHz; 2) dense meteor swarm; 3) 16, 17 MHz.

meteoric activity. This is quite natural, since the meteoric component makes a substantial contribution to the total scattered-signal level. There are no data for the 1650-km path in June and July; during these months, propagation was by reflection from the sporadic E-layer (90% of the time).

Minimum signal values are registered during periods around the vernal and autumnal equinoxes (February, September). Field strength rises appreciably in November, apparently as a result of the earth's passage through the Leonid meteor swarms.

Relation of signal level to  $E_S$ -layer. Very strong signals were very often received, for periods of several minutes and longer, and even for several hours on certain days. The high-level signals are most frequently observed during the daytime and for the most part in summer (May-August). During spring and autumn, high-level signals appear much less frequently. On comparing the high-level signals on the 1650-km path (16.170 MHz) with the ionospheric data for the midpoint of this path, we note that the high-level signals are associated with the appearance of an  $E_S$ -layer with limiting frequencies  $f_oE_S \geq \geq 3$  MHz at the middle of the path.

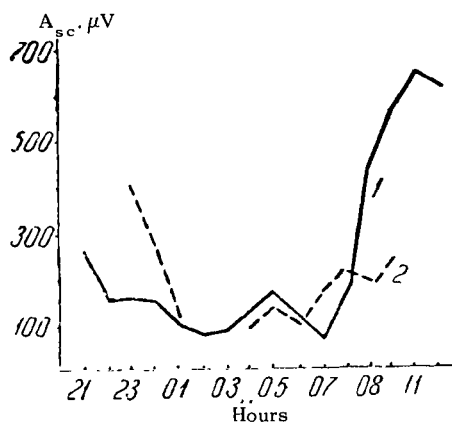


Figure 3. Diurnal Variation of  $E_{sc}$ , Propagation Via Sporadic E-Layer: 1) 16.1 MHz; 2) 18.3 MHz.

At certain hours during the daytime, the level at 16.170 MHz exceeds 500  $\mu$ V, but it fluctuates in the 100- $\mu$ V range at night (Fig. 3). At 18.340 MHz, the daytime level reaches 250  $\mu$ V at certain hours, while at night it varies in the same range as at 16.170 MHz.

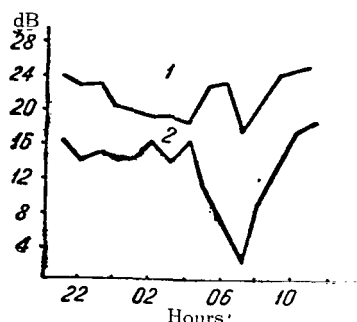


Figure 4. Diurnal Variation of Signal/Noise Ratio. 1) 18.34 MHz; 2) 16.17 MHz.

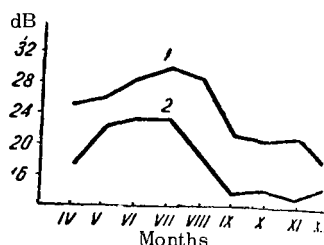


Figure 5. Seasonal Variation of Signal/Noise Ratio. 1) 18.34 MHz; 2) 16.17 MHz.

Signal/noise ratio. Cosmic noise was measured regularly on all paths for five minutes at the half-hour, a function for which the transmitter was switched off. The five-minute noise record was then used to determine the median value for each measurement session. Noise level varied insignificantly, amounting to 0.3  $\mu$ V at 18.340 MHz and 0.35  $\mu$ V at 16.17 MHz (Fig. 4). The data on the diurnal variation of the signal/noise ratio with the diurnal field-strength variation indicate that the basic features of the field-strength measurements are duplicated. At 18.340 MHz, the maximum value occurs during the morning hours (9-10) and is 29 dB, while the minimum at 5 hours is 22 dB. At 16.170 MHz, the signal/noise ratio varies from 7 to 20 dB throughout the day at 16.17 MHz and from 20 to 28 dB at 18.34 MHz. /66

For the most part, the signal/noise ratio is above 10 dB on both frequencies (Fig. 5) but not constant throughout the year. The largest values are seen in summer and the smallest ones in the fall. In all months, the signal/noise ratio at 18.340 MHz averages 5-10 dB higher than that at 16.170 MHz (Fig. 5).

## CONCLUSIONS

1. The field strength of the signal scattered by the lower ionosphere and the signal/noise ratio vary throughout the day and over the seasons in accordance with the features of the diurnal and seasonal solar and meteoric activity variations.



2. When highly directional antennas are used at the receiving end and the transmitters have outputs of 20 kW, the average signal/noise ratio does not drop below 20 dB even under the most unfavorable propagation conditions (September).

3. Reflection from the  $E_S$ -layer is an important factor in the propagation of short radio waves whose frequencies exceed the MUF of the F2-layer. In summer, this propagation mechanism is decisive for frequencies below 20 MHz.

#### REFERENCES

1. Rozov, V.I. "Elektrosvyaz'," 1967, No. 4, p. 18.
2. Dokumenty X plenarnoy assamblei (Documents of the Tenth Plenary Assembly). Vol. 2. Geneva, 1962, Moscow, "Svyaz'," 1964.

OCCUPANCY OF THE RADIO-FREQUENCY SPECTRUM  
IN THE 16-23 MHz BAND

/67

Ya.F. Ashkaliyev and V.I. Bocharov

ABSTRACT: The paper presents the results of measurement of the actual utilization of the short-wave frequency band, which were obtained by continuous registration of the number of radio stations in the 16-23-MHz band over an annual cycle (1965). It is shown that there is a definite relation between the number of radio stations and the variations of MUF-F2. During years of minimum solar activity and at night, segments free of radio stations operating by normal reflection, can be selected in the 18-23-MHz band for ionospheric-scattering links.

To evaluate the prospects for radio communications by scattering of short radio waves in the lower ionosphere, it is important to know the levels of noise of natural origin (atmospheric and cosmic) and interference from radio stations working by normal reflection. Since interference from radio stations will obviously predominate at certain times of the day and year, there is a genuine need to investigate the occupancy of the radio-frequency spectrum in the 16-23-MHz band in order to obtain statistical data on its actual utilization.

In the 16-23-MHz band\* [1], the maximum usable frequencies (MUF-F2) seldom exceed 16 MHz during years of minimum solar activity and at night; consequently, a working frequency for an ionospheric-scattering link can be selected in this frequency band. We undertook round-the-clock observations of the basic patterns in the diurnal and seasonal variations of occupancy of the 16-23-MHz radio band during 1965.

Apparatus for study of occupancy of radio-frequency spectrum and method of measurement. An instrument was built for investigation of the occupancy of the radio-frequency spectrum (Fig. 1). The antenna unit was a wide-band horizontal (WBH) dipole suspended at a height of 16 m above the ground. The antenna output voltage was applied via an RD-116 cable to a balanced transformer (BT).

---

\*Mesyachnyy prognoz rasprostraneniya radiovoln [Monthly Radio Propagation Forecasts]. Moscow, IZMIR AN SSSR [Institute of Terrestrial Magnetism, the Ionosphere, and Radio-Wave Propagation of the Academy of Sciences of the USSR], 1964.

The signal from the unbalanced transformer output was fed through a coaxial switch to a "Volna-K" receiver. The receiver was tuned through the 16-23-MHz band with a synchronous reversing motor, which was reversed automatically by setting up micro-contacts at the beginning and end of the receiver scale to be tripped by pressure from the tuning indicator. The signal was sent from the intermediate-frequency output to an amplifier-detector to which an N-370M automatic recorder was connected.

/69

A G4-1A generator was used for frequency and amplitude calibration. The time to sweep the 16-23-MHz band in one direction was 1 hour. A signal whose voltage was twice the noise level was used as interference. The number of interfering stations was computed in a  $\Delta f = 0.25$  MHz band (Fig. 2).

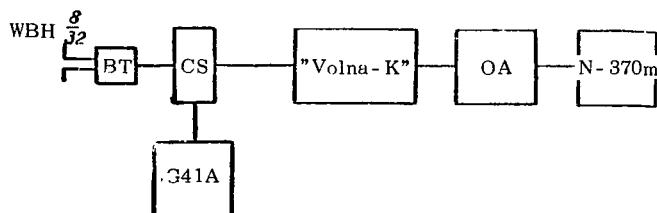


Figure 1. Block Diagram of Apparatus for Measurement of Occupancy of Radio-Frequency Spectrum.

Diurnal variations of number of radio stations. A characteristic feature in the diurnal variation of the number of radio stations is the presence of a predawn minimum and an afternoon maximum of the number of interfering stations (Fig. 3). The number of stations drops off rapidly with increasing frequency. The diurnal variations of the probability of interference from neighboring stations are generally similar to the variations of MUF-F2. However, substantial disagreement is also detected on detailed analysis of these relationships. It becomes clearly evident that the maximum number of stations is shifted to a later point in time, lagging behind the MUF by approximately three hours. Data from an ionospheric probe at the measurement station were used to compute the variations. Consequently, the incoming interference is predominantly from the west; the probability of interference from the radio stations is determined entirely by the state of the ionosphere and primarily by the behavior of the MUF.

/70

The time intervals during which the effects of interference were minimal were evaluated from the diurnal variations for each month: these intervals were from 3 to 6 hours local time in all seasons of the year, and from 0 to 6 hours at all frequencies during the autumn and spring months. The probability of interference at 22 MHz seldom exceeds 30%, even during the daytime.

Seasonal variations of interference probability. If we consider the seasonal variation of the probability of interference from radio stations at 00.00 hours local time (Fig. 4), we note that the largest numbers of radio stations are received during

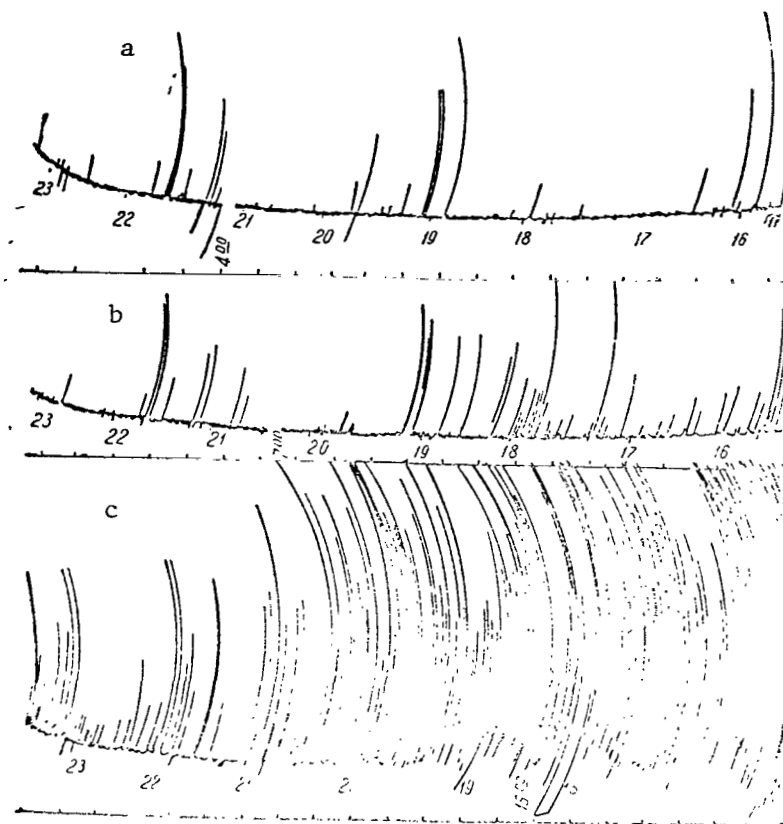


Figure 2. Typical Field-Strength Traces  
Characteristic for Nighttime (a), Predawn  
(b), and Daytime (c) Hours.

the summer months (May-July). The MUF shows a similar seasonal variation. The correlations between the interference probability and the MUF are also very close for other times of day (Fig. 5).

These quantities have in common maxima at the same seasons of the year, but their proportions are different. While the autumn maximum of MUF-F2 is sharp and exceeds the spring maximum, the picture is characteristically reversed for the interference probability. The autumn maximum is only faintly discernible, while the spring maximum is conspicuous.

/71

Thus, like the diurnal variations, the seasonal variations of the radio-station interference probability are determined to a substantial degree by the variations of MUF-F2. It is evident here that the probability of interference from neighboring stations increases with rising MUF. However, it has not been possible to establish any universal relationship, although the interference from radio stations varies as a function of the state of

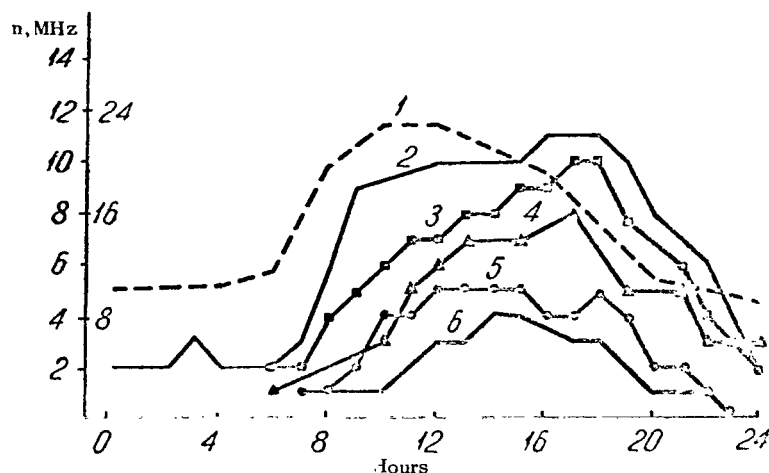


Figure 3. Number of Radio Stations in  $\Delta f = 0.25$  MHz Band as a Function of Time of Day: 1) 16 MHz; 2) 18 MHz; 3) 19 MHz; 4) 20 MHz; 5) 22 MHz; 6) MUF-F2.

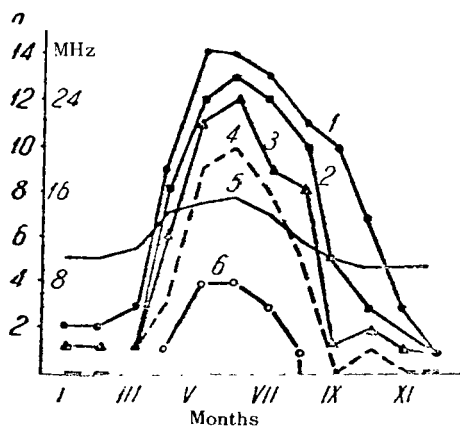


Figure 4. Number of Radio Stations in  $\Delta f = 0.25$  MHz Band: 1) 16 MHz; 2) 18 MHz; 3) 19 MHz; 4) 20 MHz; 5) MUF; 6) 22 MHz.

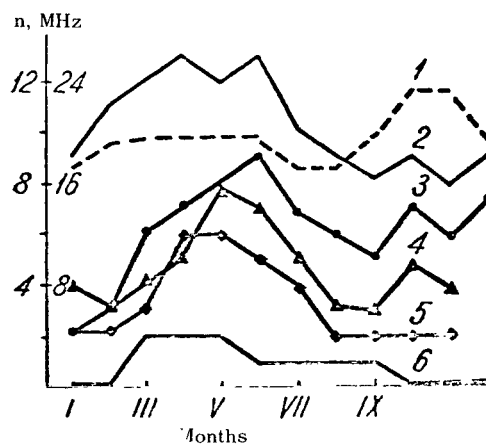


Figure 5. Number of Radio Stations in  $\Delta f = 0.25$  MHz Band for 9h. 1) MUF-F2; 2) 16 MHz; 3) 18 MHz; 4) 19 MHz; 5) 22 MHz; 6) 20 MHz.

the ionosphere. Interference from neighboring stations is a random process, and the number of radio stations working on a given segment of the frequency band depends on the time of day, the season, and a number of other factors.

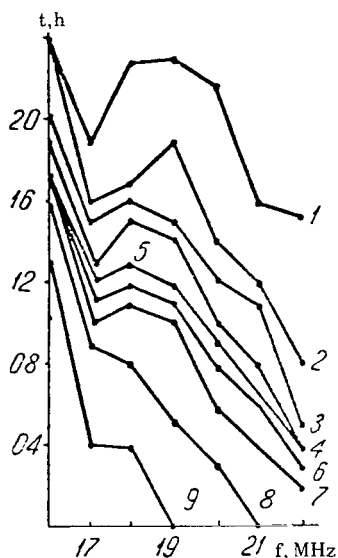


Figure 6. Probability That a Given Number of Stations will be Exceeded as a Function of Frequency. The Numerals are the Numbers of Stations in  $\Delta f = 0.25$ -MHz Bands.

Frequency dependence of the probability that a given number of interfering stations will be exceeded. A highly important statistical characteristic of radio station interference is the absolute or relative value of the time during which the number of interfering stations exceeds a given value (Fig. 6).

We see from the figure that the time during which there are more interfering stations than the number indicated on the corresponding curve decreases with rising frequency. Aspects of the frequency dependence include a decrease in the number of interference sources at 17 MHz, an increase at 18-19 MHz, and then a smooth decrease at higher frequencies. No fewer than one station per 0.25-MHz bandwidth was registered round-the-clock at 16 MHz. No fewer than 7 stations are in operation at this frequency during half of the time. From March through July, the number reaches its maximum value of 12. It is interesting to note that at least one station is observed round-the-clock even around 22 MHz during certain months.

/72

About 50% of the time, no more than three stations are in operation at 22 MHz. There are always fewer than 6 working radio stations in a 0.25-MHz band around 22 MHz throughout the entire period of the measurements.

Thus, the nature of the diurnal and seasonal variations of the number of stations is determined in general by the manner in which the maximum usable frequency varies. However, there are substantial detail differences, especially in the seasonal variation; although the MUF seldom exceeds 16 MHz during a solar activity minimum, it is still impossible to select a segment free of radio stations in the 16-17-MHz band. Such segments can be selected at any time of day or year only in the 18-23-MHz band by using authorized frequencies on ionospheric-scattering links.

Operating frequencies above 22 MHz must be selected to eliminate completely interference from radio stations working by normal reflection.

RECEIVING-ANTENNA INSTALLATION FOR IONOSPHERIC  
SCATTERING LINKS

/73

Ya.F. Ashkaliyev

ABSTRACT: Smearing of the scattered-energy flux density over a certain range of angles of arrival permits the use of a receiving-end antenna with a height lower than theoretical.

It has been observed that the median scattered-signal level received on antennas suspended at various heights undergoes minor variations [1]. Evidently, concentration of the energy flux density in a certain range of angles of arrival must be regarded as one possible cause of the constancy of the scattered-signal level.

Smearing of the scattered-energy flux density occurs [2] as a function of the fine structure of the scattering region in the ionosphere. To obtain quantitative figures, it is necessary to explain the experimental results theoretically. We shall assume to simplify mathematical analysis of the height losses that the zone of the ground surface around the antenna is flat within the first Fresnel zones and has the properties of a dielectric, and that the reflection coefficient is unity.

The scattered-energy flux density reaching the receiving antenna is the aggregate of a large number of different components. Applying the superposition principle, we shall substitute a system of  $n$  discrete beams for the angular distribution of the scattered beams.

If the antenna is mounted at height  $h$  and beam  $n$  arrives at an angle  $\theta_n$  with phase  $\alpha_n$ , the resultant signal  $E_1$  arriving directly at the antenna and  $E_2$  reflected from the ground surface can be written

$$E_1 = \sum_{n=1}^N A_{1n}(\theta_n) \cos(\omega t + \alpha_{1n} + Kh \sin \theta_n);$$

$$E_2 = \sum_{n=1}^N A_{2n}(\theta_n) \cos(\omega t + \alpha_{2n} + Kh \sin \theta_n). \quad (1)$$

Here  $n$  is the number of beams,  $\theta_n$  is the instantaneous angle of arrival of the beam,  $k$  is the wave number, and  $A_n$  and  $\alpha_n$  are

the amplitude and phase of the scattered components. Assuming a quasicoherent scattered signal, the power at the receiving-antenna output can be represented as

/74

$$P = \overline{(E_1 - E_2)^2} = \left[ \sum_{n=1}^N A_{1n}(\Theta_n) \cos(\omega t + \alpha_{1n} - Kh \sin \Theta_n) \right]^2 - \\ - 2 \sum_{n=1}^N A_{1n}(\Theta_n) \cos(\omega t + \alpha_{1n} - Kh \sin \Theta_n) \times \\ \times \sum_{n=1}^N A_{2n}(\Theta_n) \cos(\omega t + \alpha_{2n} + Kh \sin \Theta_n) + \\ + \left[ \sum_{n=1}^N A_{2n}(\Theta_n) \cos(\omega t + \alpha_{2n} + Kh \sin \Theta_n) \right]^2. \quad (2)$$

Since the terms  $E_1^2$  and  $E_2^2$  can be interpreted simply as average powers of the same signal, but with different phases, we have  $\overline{E_1^2} = \overline{E_2^2} = \overline{E^2}$ . We can then write (2) as follows:

$$P = 2\overline{E^2}(1 - \frac{\overline{E_1 \cdot E_2}}{\overline{E^2}}) = 2\overline{E^2}(1 - \rho), \quad (3)$$

where  $\rho$  is the coefficient of correlation between  $E_1$  and  $E_2$ .

To evaluate  $\rho$ , let us examine the product of the sums of the random processes in (2) in greater detail:

$$\sum_{n=1}^N A_{1n}(\Theta_n) \cos(\omega t + \alpha_{1n} - Kh \sin \Theta_n) \cdot \sum_{n=1}^N A_{2n}(\Theta_n) \cos(\omega t + \\ + \alpha_{2n} + Kh \sin \Theta_n) = \sum_{l=k=1}^N A_{1l}(\Theta_l) A_{2k}(\Theta_k) \cos(\omega t + \\ + \alpha_{1l} - Kh \sin \Theta_l) \cos(\omega t + \alpha_{2k} + Kh \sin \Theta_k) + \\ + \sum_{l=1}^N \sum_{\substack{k=1 \\ l \neq k}}^N A_{1l}(\Theta_l) A_{2k}(\Theta_k) \cos(\omega t + \alpha_{1l} - \\ - Kh \sin \Theta_l) \cos(\omega t + \alpha_{2k} + Kh \sin \Theta_k). \quad (4)$$

The product of the sums of the random processes is equal to the sum of the correlation functions of each of them plus the sum of all mutual correlation functions that can be formed from any pair of summable random variables [3].

Since the mechanism of radio-wave propagation by scattering on electron-concentration inhomogeneities is incoherent, the

/75



second term in (4) can be set equal to zero. If, further, we consider that the scattering region can be regarded as an extremely turbid medium, it becomes obvious that  $A_{1n} \approx A_{2n}$  and  $\alpha_{1n} \approx \alpha_{2n}$ ; then Expression (4) can be written as follows after simple transformations:

$$\overline{E_1 \cdot E_2} = \frac{1}{2} \sum_{n=1}^N A_n^2(\theta_n) \cos(2Kh \sin \theta_n). \quad (5)$$

With similar transformations for the denominator in (3), we obtain the correlation coefficient

$$\rho = \frac{\sum_{n=1}^N A_n(\theta_n) \cos(2Kh \sin \theta_n)}{\sum_{n=1}^N A_n^2(\theta_n)}. \quad (6)$$

Expression (6) can be simplified if we consider that the angles of arrival are normally no more than a few degrees, so that  $\sin \theta_n \approx \theta_n$ , and the antenna suspension height is assumed equal to  $h = x \cdot h_0$ , where  $h_0 = \lambda/4\theta_0$  is the theoretical optimum height.

Replacing the sum in (6) by the integral, we obtain

$$\rho = \frac{\int_{\theta} A^2(\theta) \cos(2Kh \theta) d\theta}{\int_{\theta} A^2(\theta) d\theta}, \quad (7)$$

where  $\theta_0$  is the angle of arrival of the scattered-energy flux-density maximum. To determine the theoretical height losses, Expression (7) is integrated numerically with consideration of the smearing of the angles of arrival. The amplitude distribution in the angle spectrum is taken in the form of a sine wave:

$$A(\theta) = \sin\left(\frac{\pi}{2} \cdot \frac{\theta}{\theta_0}\right). \quad (8)$$

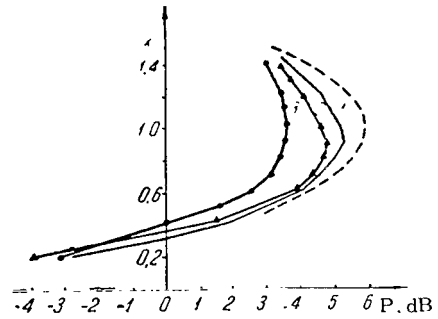


Figure 1. Power (P) at Receiver Output for Various Antenna Suspension Heights Referred to Optimum Height and Blurring of Scattered-Energy Flux Density.

As we should expect, we obtain  $\rho = \cos \pi x$  from (7) for  $\theta = \theta_0$ . With  $x = 1$ ,  $\rho$  assumes its maximum possible value of 6 dB, i.e., is the same as in coherent reception. Consequently, the ionosphere behaves as a smooth mirror, and the reflected-energy flux density is concentrated in a relatively narrow interval in which the amplitude  $A(\theta)$  is maximum (dashed curve in Fig. 1).

Curve 1 (Fig. 1) was calculated for insignificant scatter of the angles of arrival, i.e.,  $\Delta\theta = \theta_0/2$ , and the gain maximum is shifted toward lower heights. Additional losses appear as a result of smearing. The  $\rho$  for two other cases were calculated in similar fashion: by integration of (7) in appropriate angle-of-arrival scatter limits (curves 2 and 3).

For example, curve 3 (Fig. 1) was plotted for substantial angular scattering, and shows a very distinct and quite broad ( $x = 0.7-1.3$ ) saturation region. Using a real antenna height 40% off theoretical results in additional power losses (a total of 1 dB)[4].

Thus, the constancy of the median scattered-signal level when antennas suspended at various heights are used at the receiving end can be explained in terms of blurring of the scattered signal's angle of arrival.

#### REFERENCES

1. Bocharov, V.I., Nesterova, O.Sh., and Nesterova, I.I. Scattering of Short Radio Waves in the F2-Layer of the Ionosphere. Trudy SFTI, No. 38, Tomsk, 1960, p. 74.
2. Ratkliff, D. Certain Problems in the Theory of Diffraction and their Application to the Ionosphere. In: "Problemy sovremennoy fiziki" (Problems of Modern Physics), 1957, No. 10, p. 5.
3. Levin, B.R. Theoretical Foundations of Statistical Radio-mechanics. In: "Sovetskoye radio" (Soviet Radio), 1966, p. 197.
4. Fitch, E. and Ruddlesden, R. "Proc. IEE," Part B, 1959, No. 8, Vol. 105.

INPUT OF INFORMATION RECORDED ON MAGNETIC  
TAPE INTO THE BESM-3M COMPUTER

/77

E.L. Afraymovich, G.M. Kudelin, and G.M. Pelenitsyn

ABSTRACT: An input unit designed and built in the Ionosphere Sector of the Academy of Sciences of the Kazakh SSR for the BESM-3M general-purpose digital computer (GPDC) is described. The input unit uses a standard MEZ-28A studio tape recorder. An automatic data-input subroutine is presented.

There is a large class of general-purpose digital computers (the M-20, Minsk, Ural) with "standard" inputs (punched cards and punched tape) that lack auxiliary units — analog-digital converters — by means of which a converted analog signal might be put into the machine's storage. This presents difficulties for

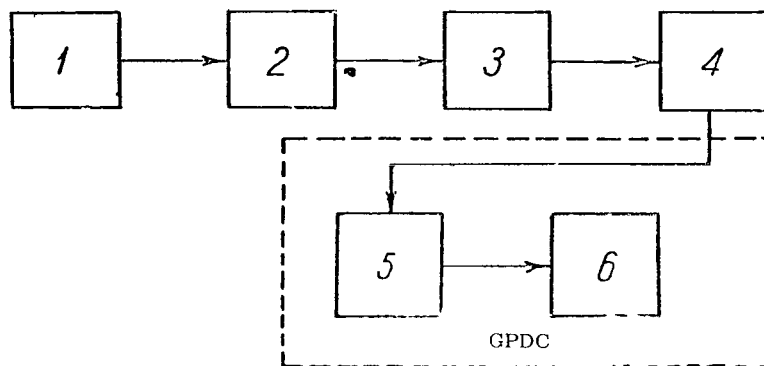


Figure 1. Block Diagram of Input Unit. 1) Converter module; 2) Storage element; 3) readout module; 4) shaper; 5) counter; 6) register.

radiophysicists studying the statistical properties of signals reflected from the ionosphere (signals from the receiver output), biologists and physicians studying records of heart sounds (EKG's), geophysicists investigating the laws governing the motions of the earth's surface (seismograms), etc.

We investigated ways of increasing the effective rate of input and increasing its reliability. A device developed in the



The tape recorder can record and play tapes at two speeds: 76.2 and 38.1 cm/sec. Pulse packets with an amplitude of 7 V from the playback amplifier of the readout module 3 go to the input of the three-stage amplifier of the shaping circuit 4 (Fig. 2). An automatic-bias network is connected to the cathode of the first amplifier, which is built around tube  $V_1$ , to improve the linearity of input-signal amplification.

Negative bias is applied to the grid of the second stage  $V_2$  to eliminate playback-amplifier noise and amplify the positive voltage drop of the symmetrical signal. Positive-going pulses from the output of the third stage  $V_3$  go through toggle  $T_1$  to the plate of the slave-multivibrator tube  $V_6$ . After the differentiating network, since the trailing edge of the pulse is slightly steeper than the leading edge, a negative-going 60-V pulse flips the circuit of  $V_6$ ,  $V_7$  and a positive-going pulse is generated on the plate load of tube  $V_7$  and goes to the input of slave blocking oscillator  $V_8$ . Negative-going 7-V pulses with a leading-edge width of 0.2  $\mu$ sec pass from the third winding of the blocking transformer through an RK-150 cable matched to the load to the input of the eight-digit binary counter 5, which is based on the BESM-3M readout-unit register 6.

In turn, each digit of the eight-place counter is decoupled through a standard amplifier-shaper network (UF-2). The multivibrator ( $V_4$ ,  $V_5$ ), which operates in the self-excited mode when the plate voltage is applied through toggle  $T_1$ , generates pulses at a repetition rate of 250 Hz for visual monitoring of binary-counter performance.

/80

#### INPUT AND CONTROL SUBROUTINE

The input subroutine is based on the principle of automatic synchronization of GPDC operation with the process recorded on the magnetic tape. The time necessary for synchronization is the sole factor determining the effective input speed, provided that all of the remaining time is used for processing of the signal. Thus, the efficiency with which the GPDC is utilized depends to a substantial degree on the flexibility of the processing program and on matching of the speed at which the information carrier moves to the speed of data processing. Thus, for example, the machine-time utilization factor varies from 0.95 to 0.1 for various types of information processing in ionospheric research. Nevertheless, the average rate of input into the GPDC is an order higher than for punched-card input in the reduction of ionospheric information.

To control the performance of the entire coupling channel to the GPDC (converter, storage, input module, input subroutine), a special test recording was made in the form of pulse packets with a constant number of pulses  $n = 32$ , and a block was included in the input subroutine for construction of the nonnormalized

0100	50	0500		0377	Print distribution
1	70	0200			
2	52				
3				0200	Restore
4	12	0200	0103	0001	
5	20	0004		0071	Wait for start of session
6	20	0004		0072	
7	15	0071	0072		
0110	36		0106		
1		0153		0074	Wait for interval
2	20	0004		0071	
3	42	0074	0154	0074	
4	76		0113		
5	20	0004		0072	
6	15	0071	0072		
7	76		0111		
0120		0156		0073	
1		0072		0070	Scanning in interval
2	20	0004		0071	
3	42	0073	0154	0073	
4	36		0100		
5	20	0004		0072	
6	15	0071	0072		
7	36		0123		
0130		0153		0074	Wait for end of pulse packet
1	20	0004		0071	
2	42	0074	0154	0074	
3	76		0132		
4	20	0004		0072	
5	15	0071	0072		
6	76		0130		
7	42	0072	0070	0075	Restore true value
0140	76		0143		
1	42	0152	0070	0076	
2	41	0076	0072	0075	
3	55	0075	0157	0075	
4		0155		0146	Construct distribution
5	16		0160		
6	13	0154	0200	0200	
7		0072		0071	
0150		0072		0070	
1	16				
2			0164	0377	
3				0002	Constants
4				0001	
5				0200	
6				2000	
7				0177	
0160	13	0143	0075	0146	Construct distribution
1	14	0114	0075	0075	
2	13	0143	0075	0146	
3	16		0146		
4	00	0156		0073	
5	16		0123		

distribution  $W(n)$ . The control recording is put in before each large-scale data-processing run and the distribution  $W(n)$  is printed out. The  $W(n)$  is analyzed to evaluate isolated misfires in the system and their number, as well as the performance of the signal-coding and -recording devices.

The subroutine incorporates a block that determines the end of the recording session (sessions are separated from one another by an interval of 2-5 sec) and transfers control to the  $W(n)$  distribution printout or normalization block, after which the program is automatically restored pending the start of the next session. Thus, the entire cassette is processed automatically without stopping the tape (one cassette has a capacity of  $\sim 10^5$  numbers).

A system for input and processing of data with a magnetic-tape storage and the BESM-3M GPDC of the Computer Technique Department of the Institute of Mathematics and Mechanics, Academy of Sciences, Kazakh SSR has been placed in operation. Signals with sampling frequencies up to 100-200 Hz can be processed with it.

I.D. Kozin

ABSTRACT: It is shown on the basis of data on the variations of the cosmic-ray neutron component, ionospheric soundings, and measurements of cosmic radio-emission absorption at "Vostok" station (Antarctica) that the ionization of the lower ionosphere increases during times of low intensity of Forbush-type cosmic rays. This is manifested in increased absorption and the appearance of strong sporadic layers in the E-region.

Geophysical observational material obtained with an AIS ionospheric sounder, an MVS-13 magnetic variation station, a riometer, and a neutron monitor are used in the present paper.

Data obtained at the geomagnetic pole on the variations of the cosmic radiation are of definite interest for analysis of the variations of solar cosmic rays during rising solar activity and their influence on the state of the ionosphere.

The influence of cosmic radiation on the ionization of the lower atmosphere has already been noted in the literature [1]. Moler [2] and Nicolet [3] were the first to advance the idea of formation of a C-layer as an effect of cosmic rays; experimental confirmation was obtained in the studies of P.Ye. Krashnushkin [4]. Evidently, a massive influx of low-energy particles to the geomagnetic pole has a substantial ionizing effect in the lower ionosphere.

We shall examine the variations of the cosmic radiation during disturbed states of the earth's magnetic field and their influence on the ionosphere (29 August-7 September 1966). This period is characterized by powerful chromospheric flares occupying large areas on the sun. They were long-lived, with the strengths attained ranging from 2f to 3b. The maximum of the chromospheric-flare disturbance fell on 2 September 1966, when a proton flare on the sun was also reported.

An extremely strong magnetic storm with sudden onset was observed at "Vostok" station at 20 hours GMT on 29 August; it ended at 16 hours 30 minutes GMT on 4 September. This storm had two active periods: 30 August and 3-4 September. "PCA" absorption was observed on the polar cap. The following attendant phenomena



TABLE 1

Date	Absorption, dB	
	20 MHz	30 MHz
30 August	-9.2	-4.6
31 August	-1.9	—
2 September	-7.8	-3.5
3 September	-30	-10.5
4 September	-9.7	-4.5

were observed during this period: nonpropagation of radio waves on the "Vostok-Mirnyy" link, which is 1400 km long; an increase in the absorption of cosmic radio noise. Table 1 gives the maximum absorption values for the disturbed days as measured with an American-made riometer by the geophysicist John H. Taylor at frequencies of 20 and 30 MHz.

/83

The figure shows the variations of the earth's magnetic field according to the MVS-13 at "Vostok" station (field-strength values for the H-component), the variations of the cosmic-radiation neutron component at "Vostok" and "Alma-Ata" stations, solar data [4], and f-diagrams based on the results of ionospheric soundings at "Vostok" station. At the onset of the magnetic storm, the intensity of the cosmic-radiation neutron component dropped abruptly, reaching 11.7% during the next 43 hours. Then, with relatively mild geomagnetic-field disturbance, the intensity recovered over a 54-hour period. The second phase of the magnetic storm began at 17 hours on 2 September, and the cosmic radiation showed a new drop in intensity, lasting 7 hours and followed by a ten-hour recovering trend. The similar fluctuations of the cosmic-radiation neutron component intensity that followed are nonstatistical; they result from the disturbed state of the magnetosphere and new corpuscular streams.

It is known that the sun is the basic source of the soft cosmic-ray component. The influence of cosmic rays and the magnetic field on the reflective state of the ionosphere is marked (Fig. 1). The f-diagram was compiled from the hour-by-hour values of the  $f_{\min}$  and  $f_0$  of the F-layer and the E-region and the frequencies of appearance of sporadic E-region formations of various types: c, l, h, r. Generally, sharp drops in cosmic-radiation intensity, like the decreases in the H-component strength of the earth's magnetic field, first cause an increase in  $f_{\min}$  and absorption as indicated by the riometer readings, and then complete disappearance of reflection in the 1-20-MHz range — total absorption. The recovery of cosmic-radiation intensity also corresponds to the reappearance of reflection (late on 3 September and on 4 September).

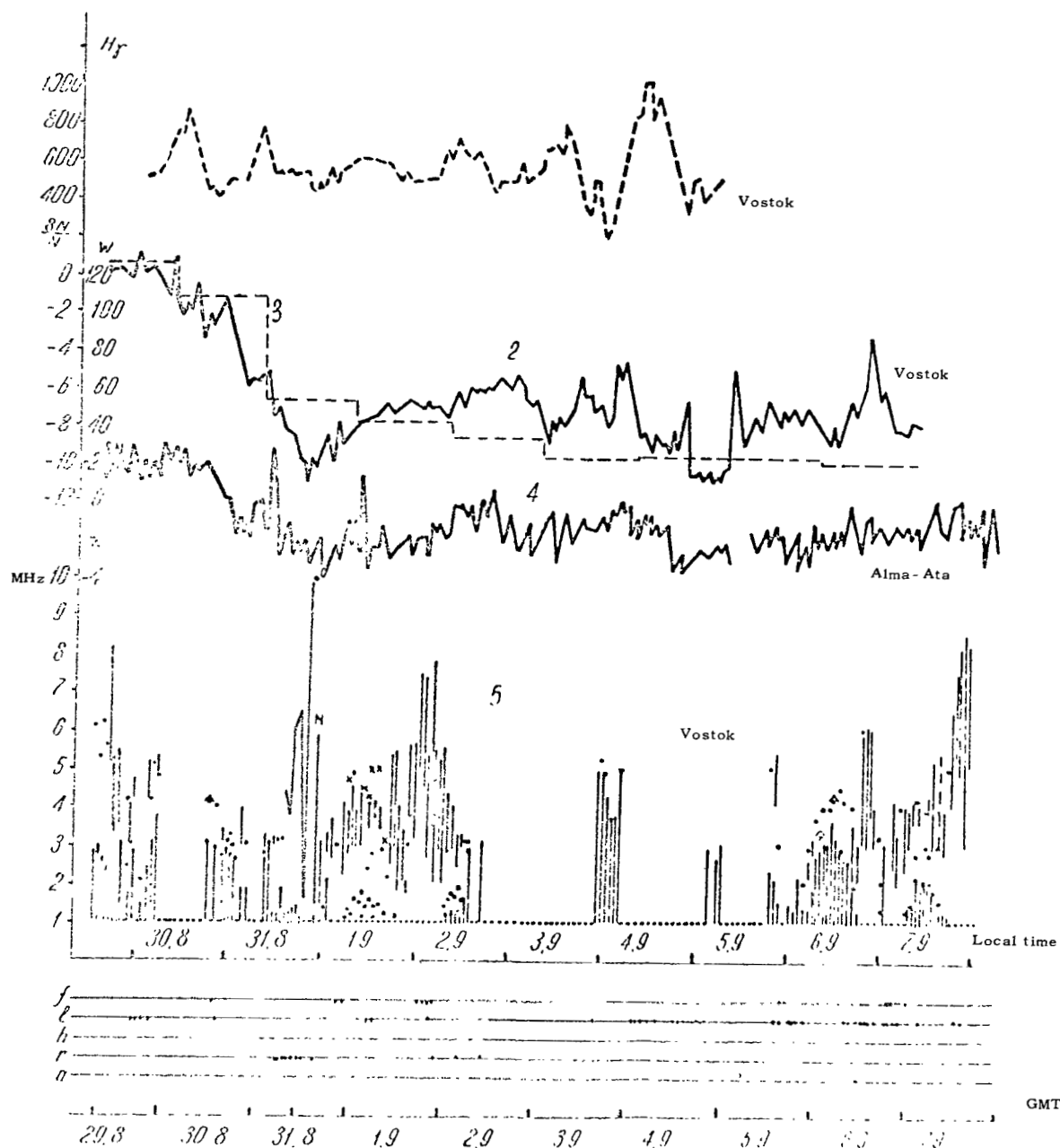


Figure 1.

1) Horizontal component of the earth's magnetic field; 2) variations of cosmic-radiation neutron component according to "Vostok" data; 3) relative sunspot numbers (Wolf numbers W); 4) variations of cosmic-radiation neutron component according to "Alma-Ata" station; 5) variation of critical frequencies of ionospheric F2-layer according to "Vostok"-station data.

Early on 6 September, the cosmic-radiation intensity began to recover, and the normal diurnal variation of the vertical-sounding critical frequencies appeared. Cases in which large chromospheric flares on the sun ( $2f$  and above) were accompanied by ionospheric disturbances manifested in increased electron concentration in the D-region (height 50-70 km) by 500-1000 electrons/cm<sup>3</sup> have already been reported in the literature [1, 5]. It is this increase in D-layer electron density that increases the nondeviative absorption of radio waves that is displayed on the screens of panoramic ionospheric stations as an increase in  $f_{\min}$  and, eventually, as total absorption. It was precisely this pattern that was observed in the ionosphere above the geomagnetic pole during the magnetic storm of 29 August-7 September, which was caused by chromospheric flares on the sun.

The absorption increases in the ionosphere were detected by the riometers and the AIS, and the abrupt appearance of strong sporadic layers after total absorption permitted the assumption that the ionization took place for the most part in the lower ionosphere; vertical drifting from the D-region to the E-region was also possible.

Thus, ionization occurs in the lower ionosphere, in the D-regions, as can be seen from the increase in absorption (see Table 1) for the low-energy cosmic-radiation component; strong reflections from sporadic formations in the E-region make their appearance (see Fig. 1).

#### REFERENCES

1. Gardner, F.F. "Australian J. Phys.," 1959, 12, 42.
2. Moler, H. "J. Geophys. Res.," 1960, 65, 1459.
3. Nicolet, M. and Aikin, A.C. "J. Geophys. Res.," 1960, 65, 1469.
4. Krasnushkin, P.Ye. and Kolesnikov, N.L. Study of the Lower Ionosphere with LW and Low-Frequency Radiosondes Mounted on a Rocket, "Dokl. AN SSSR," 1962, Vol. 146, No. 3.
5. Titherige, J.E. "J. Atmos. Terr. Phys.," 1962, 24, 269.

STATISTICAL ACCURACY OF COSMIC RADIATION  
NEUTRON COMPONENT RECORDERS

/85

L.I. Dorman and I.A. Pimenov

ABSTRACT: The paper examines a method for calculating the error of experimental data from a standard neutron monitor with consideration of the multiplicity of neutron generation. It is shown that use of the Poisson distribution to estimate the real statistical error is inadequate. The method proposed is of interest for analysis of low-amplitude periodicities in the cosmic-ray variations.

Accuracy of the experimental data obtained — the basic requirement made of equipment to register the intensity of cosmic radiation — depends on a whole series of factors, including the effective area of the detectors used to register the various cosmic-radiation components. An increase in effective registration area tends to improve statistical accuracy. However, the accuracy improvement obtained in the experimental data is usually smaller than expected [1, 2], since the operating conditions of the registering instruments and other factors lead to departures from the original theoretical models on which the accuracy calculation was based. This calculation is made on the assumption that particles striking the instrument are statistically independent and that their distribution is subject, for small average counting rates  $N(\text{pls.}) > 1$ , to Poisson's law, which is closely described by a normal distribution with increasing average counting rate  $N(\text{pls.}) \gg 1$ . Thus, for example, the condition of particle statistical independence may be violated twice in one of the most common instruments for registration of cosmic rays — the neutron monitor, which uses the principle of local neutron generation. Firstly, neutrons generated in the atmosphere may have a weak genetic relationship to one another, and, secondly, the relation becomes quite strong within the monitor itself.

As we know, the standard neutron monitor described in [3, 4], which is used by a number of international-network stations as an intensity detector for the neutron component of the cosmic rays, incorporates proportional counters filled with boron trifluoride  $\text{BF}_3$  for detection of thermal neutrons. Neutrons formed in lead on interaction with cosmic rays are moderated in paraffin. Several neutrons may be formed in the lead from a single neutron, and on moderation they will be registered with a certain efficiency

/86

by the proportional counters (Fig. 1). If each cosmic-ray neutron were registered once by the monitor, the relative statistical error of the intensity registration per unit time would be

$$\sigma^{\text{fl}} = \frac{1}{\sqrt{N}} \cdot 100\%, \quad (1)$$

where  $N$  is the number of pulses registered by the monitor during this same unit time. On the other hand, if each neutron striking the monitor is registered by an average of  $\underline{k}$  pulses ( $k \geq 1$ ) and  $N$  is the average number of pulses per unit time, we have in the general case

$$\sigma^{\text{fl}} = \sqrt{\frac{k}{N}} \cdot 100\%. \quad (2)$$

Generally speaking, therefore,  $\sigma^{\text{fl}}$  is not determined by Formula (1); Formula (2) must be used for the calculation. However, the value of  $\underline{k}$  is usually unknown. For this reason, we find  $\sigma^{\text{fl}}$  from the readings of two independent sections A and B. If the average counting rates for the sections are approximately equal,

$$\overline{N}(A) \approx \overline{N}(B) \approx N, \quad (3)$$

then according to [5]

$$\sigma_{I(A)-I(B)} = \sqrt{\frac{\sum [I(A)-I(B)]^2}{n}} = \sqrt{2} \sigma^{\text{fl}}. \quad (4)$$

Here  $I(A)$  and  $I(B)$  are the intensities of the neutron component according to sections A and B at corresponding points in time and  $n$  is the number of counts over the interval of analysis. It should be noted that the denominator in the radicand of Formula (4) must be reduced by one for small counts ( $n \leq 100$ ) to reduce the systematic error that arises.

Comparing (3) and (2), we find that

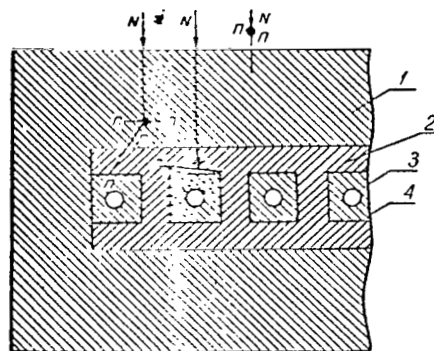


Figure 1. Diagram of Local Neutron Generation. Section through standard IGY, IGC, or IQSY neutron monitor. 1) Paraffin screen; 2) lead; 3)  $B^{10}F_3$  proportional counters; 4) paraffin.

$$k = 5 \cdot 10^{-5} \cdot N \cdot \sigma^2_{I(A)-I(B)}. \quad (5)$$

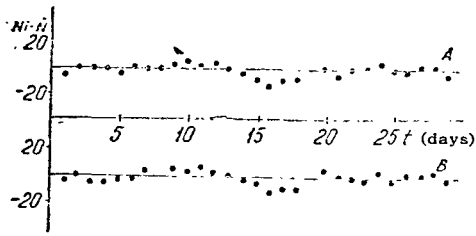


Figure 2. Daily Average Neutron Counting Rate as a Function of Time for February 1964 (Chicago) According to Sections A and B. The straight line is the average counting rate for the month. Values of the error of the daily average intensity values are plotted for the sections against the axis of abscissas.

We analyzed hour-by-hour data for the Chicago station (February 1964), which were corrected for the cosmic-ray barometric effect. Since Relation (5) is valid only if Condition (3) is satisfied, sections A and B were checked for equality of counting rates. The computed average counting rates over the interval of analysis (Fig. 2) satisfy Condition (3), since the average counting rate over a day remained within the limits of error of the daily average values throughout the month.

The variance of the readings from the two sections  $\sigma^2_{I(A)-I(B)}$  calculated by Eq. /88

(4) was  $\sim 2\%$ ; therefore,

$$k = 5 \cdot 10^{-5} \cdot N \cdot \sigma^2_{I(A)-I(B)} = 5 \cdot 10^{-5} (16 \cdot 760) \cdot 2 = 1.21.$$

This result signifies that on the average over the time interval considered, a single cosmic neutron was registered with an efficiency of 1.2. Consequently,  $\sigma^{fl}$  will be more accurately estimated as

$$\sigma^{fl} = \sqrt{\frac{k}{N}} \cdot 100\% = \sqrt{\frac{1.21}{12160}} \cdot 100\% \approx 1\%.$$

This calculated estimate exceeds the theoretical estimate obtained from the Poisson distribution:

$$\sigma^{fl} = \sqrt{\frac{1}{N}} \cdot 100\% = \sqrt{\frac{1}{12160}} \cdot 100\% \approx 0.9\%.$$

The calculation confirms the conclusions drawn in [1, 2, 6] by another method.

The method examined here for calculating the real statistical error of the experimental data makes possible quite reliable estimation of the noise level of the instrument registering the cosmic rays for a given averaging interval. This permits quick resolution of the question as to whether the data for a given time interval are suitable for analysis of low-amplitude cosmic-ray variations.

#### REFERENCES

1. Kane, R.P. A Critical Appraisal of Some Cosmic Ray Data for the IGY. Proc. Indian Acad. Sci., 1960, A52, No. 2.
2. Dyring, E. Statistical Studies of the Performance of Cosmic Rays Recording Instruments. Tellus, XIV, 1962, No. 1.
3. Simpson, J.A., Fonger, W.H., and Treiman, S.B. Phys. Rev., 1953, 90, 934.
4. Simpson, J.A. Neutron Monitor, Chicago, 1955.
5. Dorman, L.P. Variatsii kosmicheskikh luchey (Variations of the Cosmic Rays), Moscow, Gostekhizdat, 1957.
6. Dyring, E. and Lindren, S. Standard Errors of Cosmic Ray Data Corrected for Atmospheric Effects. Tellus, XIV, 1962, No. 2.

ESTIMATES OF THE ELECTRIC FIELDS IN THE  
LOWER IONOSPHERE ABOVE THE MAGNETIC EQUATOR

/89

V.N. Pogrebnoy and M.N. Fatkullin

ABSTRACT: The electric fields at the solar-activity minimum on the magnetic equator are evaluated on the basis of data from rocket studies of the vertical profiles of the ionospheric-current magnetic fields and electron concentration. The electric field strength is  $1-4 \cdot 10^2$  CGSM units. In addition, the electric field has altitude and time distributions. Its maximum is observed at a height of 110 km, and at 90 and 140 km it is smaller by a factor of 3-4 than at the 110-km height. The maximum values are registered around noon.

Investigation of electric fields in the ionosphere is necessary for study of the features of the ionosphere itself and the

TABLE 1

Flight	Date	Launch time	Geographic coordinates		Source
			$\psi$	$\lambda$	
UNH 65-4	12.III.65	8 <sup>h</sup> 30 <sup>m</sup>	11°23' S	81°25' W	[7]
UNH 65-5	12.III.65	11 30	11 25 S	81 20 W	[7]
FL-14.171	16.III.65	11 15	12 47 S	78 03 W	[8]
FL-14.176	18.III.65	11 01	12 47 S	78 00 W	[8]
FL-14.174	24.III.65	11 24	11 44 S	78 36 W	[8]
FL-14.173	26.III.65	10 41	10 12 S	79 30 W	[8]
FL-14.175	27.III.65	11 08	14 12 S	77 57 W	[8]
FL-14.70	29.III.65	10 47	12 05 S	78 14 W	[8]
PRL-20.05	7.VIII.66	13 45	8 31 N	76 52 E	[9]

origin of the geomagnetic-field variations. Until direct measurement methods were developed, ionospheric electric fields were



evaluated from ground geomagnetic observations within the framework of the dynamo theory. The investigators would state supplementary hypotheses as to current-localization regions, ionospheric electrical conductivity, etc. With the development of rocket and satellite research methods for the upper layers of the atmosphere, it became possible in principle to measure the ionospheric electric fields directly, and attempts to do so have been reported in the literature [1-5]. On the other hand, a whole series of rocket experiments was performed during the IGY and IQSY to study ionospheric currents, and the results, together with available information on other parameters of the ionosphere, enable us to estimate the electric field in the ionosphere with greater confidence than had previously been possible. Below we present the results of estimates of the electric fields in the lower ionosphere over the magnetic equator according to rocket data on the vertical ionospheric-current magnetic-field profile under magnetically quiet conditions. /90

Reference [6] presents a detailed analysis of results from rocket studies of currents in the ionosphere in middle and low latitudes. The table gives certain information on specific rocket launchings near the magnetic equator ( $I \sim 0$ ) during the morning and midday hours at a solar activity minimum.\*

Figure 1 gives a few examples of the vertical distribution of the eastward-current density in the ionosphere over the magnetic equator.

In the electric-field estimates, we began from the following conceptions. Since vertical currents are forbidden, Ohm's law for an anisotropic medium

$$\vec{j} = \sigma_{\parallel} \vec{E}_{\parallel} + \sigma_{\perp} \vec{E}_{\perp} + \sigma_H (\vec{B} \times \vec{E}_{\perp}), \quad B \quad (1)$$

in a coordinate system with the x-axis pointed toward magnetic south, the y-axis eastward, and the z-axis vertically upward, takes the form [10]:

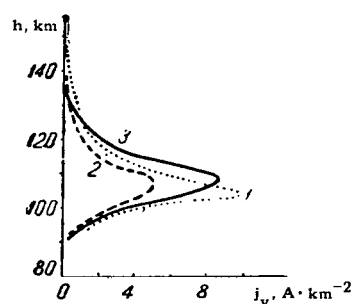


Figure 1. Vertical Distribution of Current Density in the Ionosphere Above the Magnetic Equator According to Rocket Data. 1, 2, 3) Data from flights FL-14.174, FL-14.173, and FL-14.70, respectively;  $j_y$ ) eastward component of current density;  $h$ ) height.

---

\*The restriction to these launchings takes cognizance of the fact that electron concentration was determined in addition to the current-magnetic-field measurements.

$$\left. \begin{aligned} j_x &= \sigma_{xx} E_x + \sigma_{xy} E_y \\ j_y &= -\sigma_{xy} E_x + \sigma_{yy} E_y \end{aligned} \right\} \quad (2) \quad \underline{91}$$

where

$$\left. \begin{aligned} \sigma_{xx} &= \frac{\sigma_{\parallel} \sigma_{\perp}}{\sigma_{\parallel} \sin^2 I + \sigma_{\perp} \cos^2 I} \\ \sigma_{xy} &= \frac{\sigma_{\parallel} \sigma_H \sin I}{\sigma_{\parallel} \sin^2 I + \sigma_{\perp} \cos^2 I} \\ \sigma_{yy} &= \frac{\sigma_H^2 \cos^2 I}{\sigma_{\parallel} \sin^2 I + \sigma_{\perp} \cos^2 I} + \sigma_{\perp} \end{aligned} \right\} \quad (3)$$

$\sigma_{\parallel}$ ,  $\sigma_{\perp}$ ,  $\sigma_H$  are the longitudinal, transverse, and Hall components of conductivity,  $I$  is the magnetic inclination, and  $B$  is the strength of the geomagnetic field. For small magnetic inclinations ( $I \approx 0$ ),

$$\sigma_{xx} = \sigma_{\parallel}, \quad \sigma_{xy} = 0, \quad \sigma_{yy} = \sigma_{\perp} + \sigma_H^2 \sigma_{\perp}$$

and

$$j_y = \sigma_{yy} E_y. \quad (4)$$

Around noon at the magnetic equator, meridional currents are absent or are at least much smaller than  $j_y$ .

The vertical distribution  $E_y(h)$  was computed from (4). The distributions of  $\sigma_{xx}$ ,  $\sigma_{xy}$ ,  $\sigma_{\parallel}$ ,  $\sigma_{\perp}$ ,  $\sigma_H$ , where  $\sigma_{\parallel} = n\sigma'_{\parallel}$ ,  $\sigma_{\perp} = n\sigma'_{\perp}$ ,  $\sigma_H = n\sigma'_H$ ,  $\sigma_{yy} = n\sigma'_{yy}$

$$\left. \begin{aligned} \sigma'_{\parallel} &= e^2 [1/m_e \nu_e + 1/m_i \nu_i] \\ \sigma'_{\perp} &= e^2 [\nu_e m_e (\nu_e^2 + \omega_e^2) + \nu_i m_i (\nu_i^2 + \omega_i^2)] \\ \sigma'_H &= e^2 [\omega_e m_e (\nu_e^2 + \omega_e^2) - \omega_i m_i (\nu_i^2 + \omega_i^2)] \end{aligned} \right\} \quad (5)$$

$\sigma'_{\parallel}$ ,  $\sigma'_{\perp}$ ,  $\sigma'_H$ ,  $\sigma'_{yy}$ , the corresponding conductivities per electron-ion pair,  $n$ , the electron concentration, and  $\nu_e$ ,  $\nu_i$  and  $\omega_e$ ,  $\omega_i$  the collision frequencies and gyrofrequencies of the electrons and ions, respectively, were calculated separately for each flight. The following ionospheric and atmospheric variables were assumed for the calculations.

1. For flights UNH 65-4, 65-5, and PRL-20.05, the electron-concentration profiles  $n(h)$  were determined experimentally by means of Langmuir probes mounted on the rockets. The traces of the Langmuir currents, whose intensity is proportional to electron concentration, were interpreted by comparing them with the critical frequency of the E-layer as obtained from vertical-sounding data obtained at the time of the launch. For the other flights, the electron concentration was determined with a standard  $n(h)$  profile (Fig. 2a).

/92

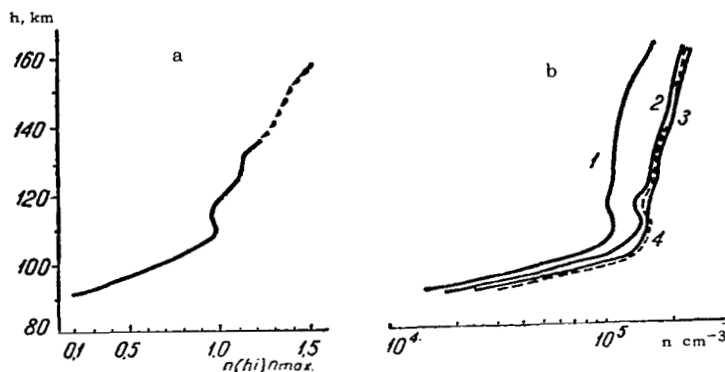


Figure 2. Electron Concentration as a Function of Height. a) Standard profile; b) rocket data. 1) Flight UNH 65-4; 2, 3, 4) flights UNH 65-3, UNH 65-2, and UNH 65-3, respectively;  $n(h_i)$  and  $n_{\max}$  are the electron concentrations at fixed height and at a maximum of the E-layer, respectively, in  $\text{cm}^{-3}$ ;  $h$  is height.

A considerable number of launchings near the magnetic equator with Langmuir probes aboard, namely UNH 64-1, 64-2, 64-3 [11]; UNH 65-2, 65-3, 65-4, 65-5 [7], PRL-20.05, FL-10.11, FL-10.12, FL-10.14 [9], FL-14.177, 14.179, 14.180, 14.181, and 14.182 [12] indicated that although the flights were made not only at different hours and on different days, but also in different years, the Langmuir-current traces and, consequently, the height profiles  $n(h)$  for the quiet atmosphere were qualitatively identical in nature (Fig. 2b). This made it possible to construct a standard  $n(h)$  profile for the region of the magnetic equator by statistical processing of the data.

The  $n(h)$  profile can be constructed by assigning the  $n_{\max}$  determined from the vertical-sounding data and using the ratios  $n(h_i)/n_{\max}$  given in Fig. 2a. This method was used to compute  $n(h)$  for the launchings FL-14.171, 14.173, 14.174, 14.175, 14.176, and FL-14.70.

2. We used the CIRA 1965 standard model of the atmosphere [13] to compute the altitude distribution of electron and ion collision frequencies, which were computed from the improved expressions [14, 15]

$$\left. \begin{aligned} \nu_e &= \nu(e, N_2) + \nu(e, O_2) + \nu(e, O) \\ \nu_i &= \nu(O_2^+, O_2) + \nu(N_2^+, N_2) \end{aligned} \right\} \quad (6)$$

where

$$\left. \begin{aligned} \nu(e, N_2) &= 2,33 \cdot 10^{-11} n(N_2) [1 - 1,21 \cdot 10^{-4} T_e] T_e \\ \nu(e, O_2) &= 1,82 \cdot 10^{-10} n(O_2) [1 + 3,6 \cdot 10^{-2} T_e^{-1}] T_e^{-1} \\ \nu(e, O) &= 2,8 \cdot 10^{-10} n(O) \cdot T_e^{-1} \\ \nu(O_2^+, O_2) &= 3,4 \cdot 10^{-13} n(O_2) \Gamma^{1/2} (10,6 - 0,76 \lg \Gamma)^2 (\Gamma > 1600^\circ K) \\ \nu(O_2^+, O_2) &= 8,2 \cdot 10^{-10} n(O_2) \quad (\Gamma < 1600^\circ K) \\ \nu(N_2^+, N_2) &= 3,6 \cdot 10^{-13} n(N_2) \Gamma^{1/2} (14,2 - 0,96 \lg \Gamma)^2 \end{aligned} \right\} \quad (7)$$

$\nu(e, N_2)$ ,  $\nu(e, O_2)$ ,  $\nu(e, O)$  are the frequencies of collisions of electrons with neutral  $N_2$ ,  $O_2$ , and  $O$  molecules, respectively;

$\nu(O_2^+, O_2)$ ,  $\nu(N_2^+, N_2)$  are the frequencies of collisions of positive /94 ions with neutral  $O_2$  and  $N_2$  molecules;

$T_e$  and  $T_i$  are the electron and ion temperatures;

$T_n$  is the temperature of the neutral gas,  $\Gamma = T_e + T_i$ . It was assumed that  $T_e = T_i = T_n$ .

The calculated distributions  $\nu_e(h)$  and  $\nu_i(h)$  and the experimental values of  $\nu_e$  determined by various methods [16-23] are shown in Fig. 3. As we see, they agree well with the theoretical values of  $\nu_e(h)$ .

The components of anisotropic conductivity per electron-ion pair were calculated for two longitudes:  $\lambda = 75^\circ E$  and  $75^\circ W$  (Fig. 4).

The calculations showed that the electric fields in the lower ionosphere over the magnetic equator are subject to considerable altitude and time variations (Fig. 5). The altitude distribution of  $E_y$  has a maximum at heights around 110 km, where the field strength may reach  $\sim 4 \cdot 10^2$  CGSM units in the midday hours at the

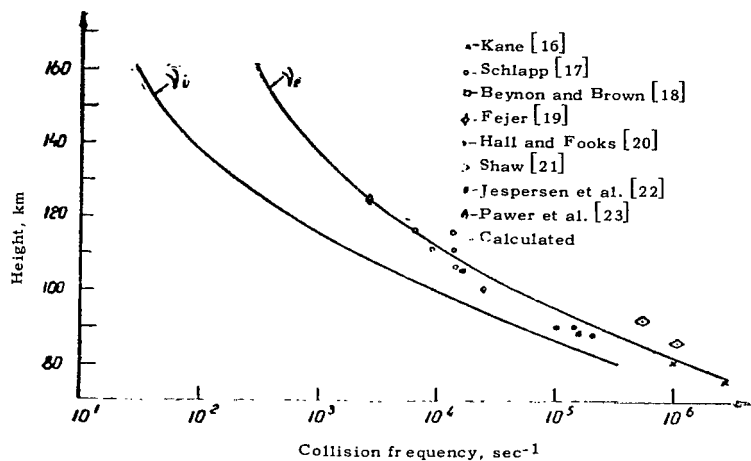


Figure 3. Collision Frequencies as Functions of Height.  $\nu_e$  is the frequency of electron collisions;  $\nu_i$  is the frequency of ion collisions.

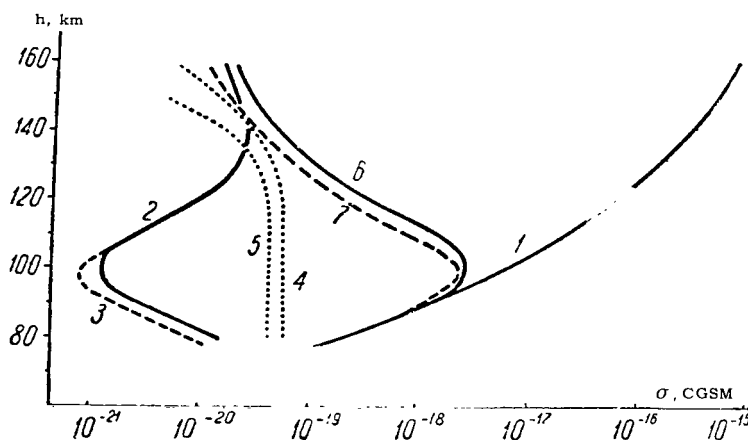


Figure 4. Components of Conductivity per Electron-Ion Pair as Functions of Height. 1, 2, 4, 6)  $\sigma_{II}'$ ,  $\sigma_{\perp}'$ ,  $\sigma_H'$ ,  $\sigma_{yy}'$  at longitude  $75^\circ$  W; 3, 5, 7)  $\sigma_{\perp}'$ ,  $\sigma_H'$ ,  $\sigma_{yy}'$  at longitude  $75^\circ$  E, where  $\sigma_{II}'$  is the longitudinal component,  $\sigma_{\perp}'$  is the transverse component,  $\sigma_H'$  is the Hall component, and  $\sigma_{yy}'$  is the Cowling component of the conductivity tensor.

solar activity minimum. At the heights  $h = 90$  and  $140$  km, the electric field strength is smaller by factors of 3-4 than at  $h = 110$  km. The maximum values of  $E_y(h, t)$  occur around noon ( $\sim 11^h00^m - 11^h30^m$ ).

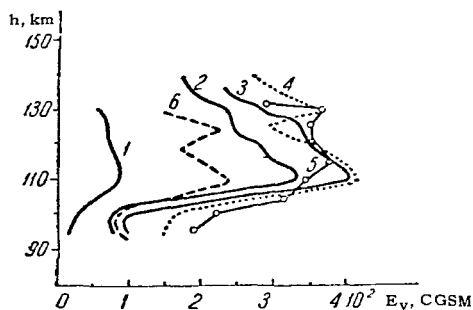


Figure 5. Altitude Profiles of the Electric Field. Curves 1, 2, 3, 4, 5, and 6 were plotted on the basis of the rocket flights UNH 65-4, UNH 65-5, FL-14.70, FL-14.176, FL-14.174, and FL-14.173, respectively.

It is interesting to compare the resulting values with experimental data on the electrostatic field in the ionosphere. Such experiments have been performed at middle latitudes and in the regions of the polar electrojet.  $E$  (the component of the electrostatic-field vector perpendicular to the magnetic field) and  $E_{II}$  (the component of electrostatic-field vector along the magnetic field) were determined at middle latitudes with electrostatic fluxmeters carried on rockets. According to measurements made on 15 November 1961 and 8 June 1963 at heights of 200-400 km,

$E_{\perp} \approx 7 \cdot 10^{-2} \text{ V} \cdot \text{m}^{-1}$ , and according to the results of the 18 October 1962 and 18 June 1963 launchings,  $E_{\perp} \approx 1 \cdot 10^{-1} \text{ V} \cdot \text{m}^{-1}$  and  $E_{II} \approx 10^{-3}$

$\text{V} \cdot \text{m}^{-1}$  [2]. Reference [1] cites values of  $E_{\perp} = 2 \cdot 10^{-1} \text{ V} \cdot \text{m}^{-1}$ . A rocket launched at about midnight on 17 October 1966 into a region with a visible aurora made it possible to estimate both  $E_{\perp} \approx 8.5 \cdot 10^{-2} \text{ V} \cdot \text{m}^{-1}$  and  $E_{II} \approx 2 \cdot 10^{-2} \text{ V} \cdot \text{m}^{-1}$  [4].

Experiments were performed in middle latitudes in 1964-65 (a total of 12 high-altitude-rocket launchings) with formation of artificial clouds at heights of 130-200 km. Their motion was used to estimate  $E_{\perp}$ , which was normally  $1-3 \cdot 10^{-3} \text{ V} \cdot \text{m}^{-1}$  in this case [3]. In April 1967, barium was ejected from a rocket at a height of 230 km near the observatory at Kiruna, Sweden. The value of  $E_{\perp}$  derived from the motion of the barium-cloud ions varied in the  $(2-20) \cdot 10^{-3} \text{ V} \cdot \text{m}^{-1}$  range [5].

According to our estimates, the electric fields in the ionospheric E-layer above the magnetic equator around noon were  $1-4 \cdot 10^{-2} \text{ CGSM}$ , or  $1-4 \cdot 10^{-4} \text{ V} \cdot \text{m}^{-1}$ . These values are 1-2 orders below the electric fields measured experimentally at middle and high latitudes.

This result does not contradict the dynamo theory, since, according to the latter, the electric fields are generated at middle latitudes and transported to low latitudes. Naturally,  $E_y$  is smaller at low than at middle latitudes. Experiments to

/95

/96

measure  $E_y$  at the magnetic equator would be extremely desirable for arrival at a final conclusion.

## REFERENCES

1. Kavadas, A. and Johnson, D. Space Res., 1964, 4, 365.
2. Gdalevich, G.L. and Imyanitov, I.M. Issledovaniye kosmicheskogo prostranstva (Investigation of Cosmic Space), Moscow, "Nauka," 1965.
3. Haerendel, G., Lüst, R., and Rieger, E. Planet Space Sci., 1967, 15, 1.
4. Moser, F.S. and Bruston, B. J. Geophys. Res., 1967, 72, 1109.
5. Föppl, H., Haerendel, G., Haser, L., Lüst, R., Meezner, F., Meyer, B., Heuss, H., Rabben, H., Rieger, E., and Stocker, J. J. Geophys. Res., 1968, 73, 21.
6. Pogrebnoy, V.N. and Fatkullin, M.N. Geomagn. i aeronomiya, 1969, 9, 69.
7. Maynard, N.C. J. Geophys. Res., 1967, 72, 1863.
8. Davis, T., Burrows, K., and Stolaric, J. J. Geophys. Res., 1967, 72, 1845.
9. Prakash, S. Subbarays, M., and Gupta, S. Rocket and Balloon Stud., Ahmedabad, 1967, 13, 34.
10. Baker, W. and Martyn, D. Phil. Trans. Roy. Soc. London, 1953, A246, 285.
11. Maynard, N. and Cahill, L. J. Geophys. Res., 1965, 70, 5923.
12. Aikin, A. and Blumbe, L. J. Geophys. Res., 1968, 73, 1617.
13. CIRA 1965, Cospar International Reference Atmosphere, Amsterdam, 1965.
14. Banks, P. Planet Space Sci., 1966, 14, 1025.
15. Banks, P. Planet Space Sci., 1966, 14, 1105.
16. Kane, J. J. Atmos. Terr. Phys., 1961, 23, 338.
17. Schlapp, D. J. Atmos. Terr. Phys., 1959, 16, 340.
18. Beynon, W.J.G. and Brown, G.M. Private communication, 1965.
19. Fejer, J. J. Atmos. Terr. Phys., 1955, 7, 322.
20. Hall, J. and Fooks, J. Planet Space Sci., 1965, 13, 1013.
21. Shaw, I.J. Proc. Phys. Soc., 1951, B64, 1.
22. Jespersen, M., Petersen, O., Rybner, J., Bjeland, J., Holt, O., and Landmark, B. Electron Density Distribution in Ionosphere and Exosphere, Amsterdam, 1964, 22.
23. Pauer, K., Bibl, K., Argence, E. C.R. Acad. Sci., Paris, 1951, 233, 667.

ON THE POSSIBILITY OF EXPLAINING FEATURES OF THE LATITUDE  
VARIATIONS OF  $S_q(H)$  AND  $S_q(Z)$  IN THE EQUATORIAL  
REGION BY ELECTRICAL MODELLING

/97

V.N. Pogrebnoy, G.I. Gordiyenko, and B.T. Zhumabayev

ABSTRACT: Curves of  $H$  (the horizontal component) and  $Z$  (the vertical component) of the magnetic field from a strip with an assigned current-density distribution compiled from the results of electrical modelling are calculated. The calculated curves are compared qualitatively with latitude curves of  $S_q(H)$  and  $S_q(Z)$  obtained from ground magnetic observatory data. It is shown that the forms of the theoretical  $H$  and  $Z$  and the experimental latitude variations of  $S_q(H)$  and  $S_q(Z)$  are qualitatively similar. Moreover, electrical modelling made it possible to explain the appearance of secondary maxima during the forenoon hours, valleys in the latitude curve of  $S_q(H)$  in the early morning and evening hours near the magnetic equator, and the complex form of the latitude curves of  $S_q(H)$  and  $S_q(Z)$ , the latter in terms of nonuniform current-density distribution in the equatorial electrojet from the period of its formation to completion of its decay.

Variations of  $H$ ,  $Z$ , and  $D$  recorded at ground magnetic observatories are the starting materials for study of the parameters of the equatorial electrojet. The value of observations from a network of temporary and permanent observatories situated at the same longitude on either side of the magnetic equator is obvious. Such observations were first made by Giesecke [1]. On the basis of data obtained at 14 stations in the latitude range from  $16^{\circ}12'$  S to  $3^{\circ}24'$  N at longitude  $75^{\circ}$  W, he made a detailed study of the latitude variation of the  $H$ -component diurnal amplitude and established that this amplitude has a maximum in a narrow zone within  $\pm 3-4^{\circ}$  of the magnetic equator. Subsequent latitude surveys [2, 3] and IGY data obtained with 11 stations functioning directly on the magnetic equator and more than 30 magnetic observatories in the equatorial zone ( $\pm 20^{\circ}$ ) brought out a whole series of peculiarities in the latitude variations of  $S_q(H)$  and  $S_q(Z)$ . For example, it was reported in [4, 5] that the form of



the latitude-variation curves varies widely, not only from day to day, but even from hour to hour.

However, a statistical analysis that we made of the latitude-variation curve of  $S_q(H)$  and  $S_q(Z)$  indicates that the characteristic curve types shown in Fig. 1 are observed at specific hours of the day, namely: the early morning hours (6h), evening (18h), midday (11-12h), forenoon (8-10h), and afternoon hours (13-17h).

It is evident from the figure that the latitude curve of  $S_q(H)$  has either a maximum or a minimum at the magnetic equator in the early morning or evening hours (see curves 1 and 2, Fig. 1). Around noon, the  $S_q(H)$  curve peaks with a maximum at about 11 hours local time. It is important to note that the peak of the latitude curve falls at the latitude of the magnetic equator.

The form of the latitude curve of  $S_q(H)$  is quite complex in the forenoon and afternoon hours. Although the values of  $S_q(H)$  are higher near the magnetic equator, one or two additional peaks usually appear on the latitude curve to the north or south of the magnetic equator (see curves 3 and 4, Fig. 1).

We note further that if the latitude curves of  $S_q(H)$  are analyzed in a broad latitude band,  $\pm 20-30^\circ$ , they are found to be asymmetric about the magnetic equator. However, the  $S_q(H)$  curves are symmetrical with respect to the magnetic equator in a narrow zone,  $\pm 4-6^\circ$ , during the midday hours.

The latitude curve of  $S_q(Z)$  is also complex in form. Its study would require a network of observatories denser than that used for the latitude surveys [1-3]. At present, therefore we can speak only of the most general features of the latitude variations of  $S_q(Z)$  in the region of the magnetic equator, namely:

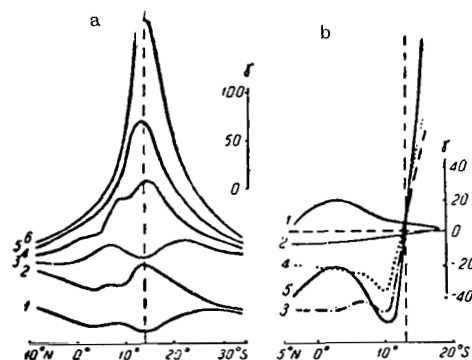


Figure 1. Latitude Variations of  $S_q(H)$  and  $S_q(Z)$

According to Data from Ground Magnetic Observatories. a, b)  $S_q(H)$  and  $S_q(Z)$ , respectively; 1,2)

Typical curves for the morning (evening) hours; 3,4) forenoon (afternoon) hours; 5,6) for midday hours; the vertical dashed line is the line of the magnetic equator.

1. The values of  $S_q(Z)$  are positive in the southern hemisphere and negative in the northern hemisphere.

2. The transition of  $S_q(Z)$  from positive to negative is observed in the region of the magnetic equator.

3. The values of  $S_q(Z)$  are considerably more south of the magnetic equator than north of it. /99

The known models of the equatorial electrojet [6, 7, 8] cannot be used to explain the complex form of the  $S_q(H)$  and  $S_q(Z)$  latitude curves. However, the scheme that we proposed earlier, in which the equatorial electrojet is formed from middle-latitude  $S_q$  currents, made it possible to use electrical modelling to compute the current-density distribution in the jet from the period of its formation to the end of its decay.

By way of example, Fig. 2, c and f, shows latitude profiles of the current-density distribution in the equatorial region of the ionosphere for the following particular conditions:

strip width of equatorial electrojet  $2b = 600$  km;

height of current layer above ground level  $h = 110$  km.

conductivity ratios  $\sigma_2 = 5\sigma_1$  and  $\sigma_2 = 2\sigma_1$ , where  $\sigma_2$  and  $\sigma_1$  are the conductivities of the strip and the surrounding region, respectively.

It is known that a strip of width  $2b$  with uniform current  $I$  at height  $h$  above ground level creates a magnetic field at the ground that can be computed by the formulas

$$H = 2I \operatorname{arctg} \frac{2bh}{h^2 + x^2 - b^2}; \quad (1)$$

$$Z = -I \ln \frac{h^2 + (x+b)^2}{h^2 + (x-b)^2}, \quad (2)$$

where  $H$  and  $Z$  are the horizontal and vertical components of the magnetic field and  $x$  is the present coordinate.

$H$  and  $Z$  were computed for various  $2b$  (10 m, 20 m, ..., 1190 m, 1200 m) by (1) and (2) on a BESM-3M electronic computer, assuming  $I$  equal to 1 CGSM unit. However, the fields were added graphically in compiling the  $H$ - and  $Z$ -curves for the particular current layers.

The calculated results appear in Fig. 2. The following features are to be noted:

1. When  $\sigma_2 = 5\sigma_1$ , the H-component shows a peak with a maximum in the early morning hours; additional maxima appear during the forenoon hours, approximately at the edge of the strip; during the midday hours, there is again a single peak with the maximum on the magnetic equator. The midday values of H on the magnetic equator are 5 times the values of H away from the magnetic equator.

2. If  $\sigma_2 = 2\sigma_1$ , the H-curve forms a valley in the early morning hours, i.e., the values of H are smaller near the equator than the H at distances of 700-800 km from the magnetic equator. During the forenoon hours, the maxima are observed near the equator, and two peaks form approximately at the edge of the strip; around midday, a single peak is observed, with midday values of H at the magnetic equator twice as large as the H at distance from the magnetic equator.

3. The H-curve for strip 5 indicates that the maximum-H peak shifts away from the magnetic equator in the direction of an eddy with high current density. In this case, the H-curve is asymmetric.

4. The Z-curves have maxima and minima that clearly mark the boundaries of the strip for  $\sigma_2 = 5\sigma_1$ , but they are more complex in nature with  $\sigma_2 = 2\sigma_1$ .

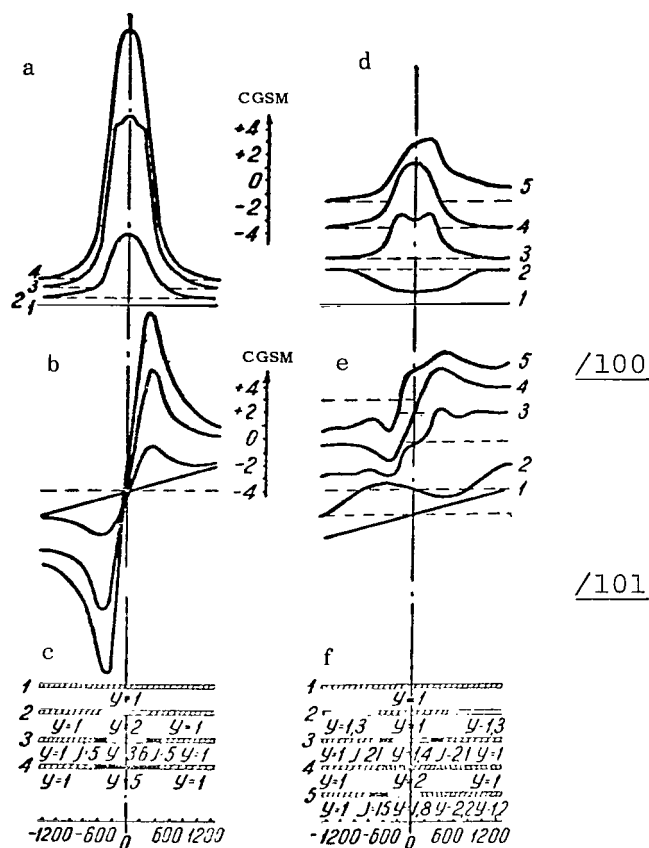


Figure 2. Calculated H- and Z-Components of Magnetic Field from Current Strip. a, d) H-curves; b, e) Z-curves for  $\sigma_2 = 5\sigma_1$  and  $\sigma_2 = 2\sigma_1$ , respectively;  $\sigma_2$ ) conductivity of strip;  $\sigma_1$ ) conductivity of surrounding medium; c, f) current density distribution profiles in strip for  $\sigma_2 = 5\sigma_1$  and  $\sigma_2 = 2\sigma_1$ , respectively. The profiles 2 are characteristic for the current distribution in the equatorial electrojet (equinox conditions) during the morning (evening) hours; 3) during forenoon (afternoon) hours; 4) during midday hours; 5) during forenoon hours (solstice conditions); profile 1: uniform conductivity.

It is interesting to compare the calculated H- and Z-curves with the latitude curves of  $S_q(H)$  and  $S_q(Z)$  obtained from magnetic-observatory observations. Since it was possible to model only part of the global  $S_q$  of the current system, and not all of it, this comparison can be made only qualitatively. For example, let us compare curves 2 (Fig. 2d) with curve 1 (Fig. 1a), 2 (Fig. 2a) with 2 (Fig. 1a), 1 (Fig. 2d) with 2 (Fig. 1b), 2 (Fig. 2d) with 1 (Fig. 1b), 3 (Fig. 2d) with 3 (Fig. 1a), 3 (Fig. 2a) with 4 (Fig. 1a), 3 (Fig. 2d) with 3 (Fig. 1b), 4 (Fig. 2d) with 4 (Fig. 1b), 4 (Fig. 2d) with 5 (Fig. 1a), 4 (Fig. 2a) with 6 (Fig. 1a), 4 (Fig. 2b) with 5 (Fig. 1b), 5 (Fig. 2d) with 4 (Fig. 1a).

We see from comparison of the curves (Figs. 1 and 2) that the forms of the calculated latitude variations of  $S_q(H)$  and  $S_q(Z)$  and those obtained from observations are qualitatively similar.

Electrical modelling made it possible to explain such features of the latitude variation of  $S_q(H)$  as the appearance of the secondary forenoon maxima and the valleys in the latitude curve of  $S_q(H)$  during the early morning (late evening) hours near the magnetic equator; it also indicated a cause for the complex form of the  $S_q(H)$  and  $S_q(Z)$  latitude curves: nonuniform current-density distribution in the strip.

Thus, electrical modelling opens new prospects for study of equatorial electrojet phenomena.

## REFERENCES

/102

1. Giesecke, A.A. J. Geophys. Res. 1949, 54, 90.
2. Ogbuehi, P.O. and Onwumechilli, C.A. J. Geophys. Res. 1963, 68, 2421.
3. Godivier, R. and Crenn, Y. Annales de Geophys., 1965, 21, 143.
4. Yaremko, L.N. Inform. bull. "Geofizika i astronomiya," 1966, No. 9, 137.
5. Hutton, R. J. Atmos. and Terr. Phys., 1967, 29, 1411.
6. Chapman, S. Arch. Meteorol. Geophys., 1951, 4, 368.
7. Sugiura, M. and Cain, J. J. Geophys. Res., 1966, 71, 1869.
8. Unitiedt, J. J. Geophys. Res., 1967, 72, 5799.

ON THE RESOLUTION OF THE STANDARD ALGORITHM FOR  
COSMIC-RAY STATIONS

/103

I.A. Pimenov

ABSTRACT: The resolution of the standard algorithm for cosmic-ray stations (SA CRS) [1, 2] is discussed. It is shown that resolution increases with increasing averaging interval. However, this is accompanied by an increase in the uncertainty with which the SA CRS is localized.

References [1, 2] proposed a method for quality rating of new instruments for registration of the secondary cosmic radiation at cosmic-ray stations (CRS). The essentials of the proposed method are as follows. The following methods were used for qualitative analysis of the zero-level drifts of certain CRS channels accurate to 0.1% against the background of cosmic-ray variations ranging into the tens of percent (after preliminary testing of the traces from identical channels for parallelism):

## 1. The method of ratios

$$A_i^{kl} = I_i^k / I_i^l, \quad (1)$$

where  $A_i^{kl}$  is a parameter characterizing the intensity ratio at the particular point in time,  $I_i^k$  and  $I_i^l$  are the registered intensity values in pulses, and  $k$  and  $l$  are the channels.

## 2. The method of differences

$$B_i^{kl} = I_i^k - I_i^l, \quad (2)$$

where  $B_i^{kl}$  is a parameter characterizing the intensity difference in relative units at the particular point in time.

Series of  $A_i^{kl}$ ,  $B_i^{kl}$  ( $i = 1, 2, \dots$ ) are then analyzed for all possible combinations of  $k$  and  $l$ . By using both methods, we

can exclude periodic components from the traces. Consequently, the standard algorithm for the CRS (SA CRS) is a method of investigating the noise associated with operation of the apparatus registering the cosmic radiation and governed by the statistical nature of the cosmic rays. Detection of faults in the performance of CRS channels and their localization are based on the fact that the behavior of the noise will change when there is a breakdown. /104  
It can be shown that the equation of the probability density for the  $B_i^{kl}$  will be subject to the normal law

$$f_{B_i^{kl}} = \frac{1}{\sqrt{2\pi} \sqrt{D(I_i^k) + D(I_i^l)}} \exp \left\{ - \frac{[(I_i^k - I_i^l) - (\bar{I}_i^k - \bar{I}_i^l)]^2}{2[D(I_i^k) + D(I_i^l)]} \right\} \quad (3)$$

on the interval of normal functioning of the registering instrument. Since the values of  $I_i^k$  and  $I_i^l$  are expressed in relative units for the  $B_i^{kl}$ , Formula (3) can be written

$$f_{B_i^{kl}} = \frac{1}{\sqrt{2\pi} \sqrt{D(I_i^k) + D(I_i^l)}} \exp \left\{ - \frac{(I_i^k - I_i^l)^2}{2[D(I_i^k) + D(I_i^l)]} \right\}. \quad (4)$$

The ordinary estimate of the variance of the  $B_i^{kl}$  and

$$\sigma_{B_i^{kl}} = \sqrt{D(I_i^k) + D(I_i^l)}$$

will be somewhat on the high side, since it does not take account of the fact that the counts  $I_i^k$  and  $I_i^l$  from which the  $\sigma_{B_i^{kl}}$  are calculated are pairwise related. A more accurate estimate will be

$$\sigma_{B_i^{kl}} = \sqrt{\frac{\sum_i (\Delta_i - \bar{\Delta})^2}{n-1}} = \sqrt{\frac{\sum_i [(I_i^k - I_i^l) - (\bar{I}_i^k - \bar{I}_i^l)]^2}{n-1}}. \quad (5)$$

Consequently, the probability density equation of the  $B_i^{kl}$  will be determined by (3), where the value of  $\sigma_{B_i^{kl}}$  is calculated by (5).

When there are breakdowns in channel operation, the behavior of the  $B_i^{kl}$  series will change for certain combinations of

the indices  $\underline{k}$  and  $\underline{l}$ . A similar situation will also arise for the  $A_i^{kl}$ . Thus, in the case of regular failures, Eq. (5) will take the following form for a stage failure:

$$f_{B_i^{kl}} = \frac{1}{\sqrt{2\pi} \cdot \sigma_{B_i^{kl}}} \exp \left\{ \frac{[(I_i^k - I_i^l) - (\bar{I}_i^k - \bar{I}_i^l \pm \gamma(\bar{I}_i^k - \bar{I}_i^l))]^2}{2\sigma_{B_i^{kl}}^2} \right\} \quad (6)$$

and for line failure:

$$f_{B_i^{kl}} = \frac{1}{\sqrt{2\pi} \cdot \sigma_{B_i^{kl}}} \exp \left\{ \frac{[(I_i^k - I_i^l) - (aI + b)]^2}{2\sigma_{B_i^{kl}}^2} \right\}. \quad (7)$$

The parameters  $\delta$ ,  $\underline{a}$ , and  $\underline{b}$  in (6) and (7) are found by the method of least squares. In calculating  $\delta(\bar{I}_i^k - \bar{I}_i^l)$ ,  $\underline{a}$ , and  $\underline{b}$ , it is necessary to remember that any type of failure can be detected if its magnitude exceeds the minimum noise level characteristic for the particular instrument. It is natural to assume that this level will be lower for equipment that performs stably and reliably. At the same time, the over-all noise level will be higher than the minimum at certain values of the averaging interval  $\Delta T$ , since the quantities  $A_i^{kl}$  and  $B_i^{kl}$  also depend on statistical fluctuations. Hence the condition that the minimum noise level be exceeded is necessary, but not sufficient for failure detection. We should expect  $\sigma_{B_i^{kl}}^2$ , which

characterizes the total noise level, to decrease with increasing averaging interval  $\Delta T$ , since the influence of statistical fluctuations becomes weaker with increasing  $\Delta T$ . Consequently, the  $\sigma_{B_i^{kl}}^2 = f(\Delta T)$  curve will drop with ris-

ing  $\Delta T$ , making an asymptotic approach to the noise level governed by equipment operation. In other words, the  $\sigma_{B_i^{kl}}^2 = f(\Delta T)$  curve will tend to the set-noise level of the

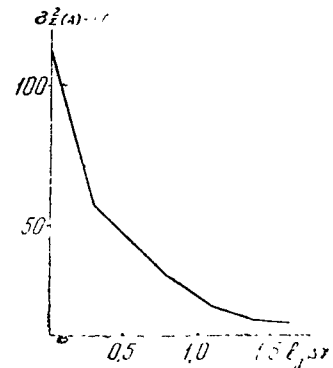


Figure 1. Variance of Difference Between Readings of Identical Channels  $\underline{k}$  and  $\underline{l}$ ,  $\sigma^2_{I(A)-I(B)}$ , as a Function of Length of Averaging Interval. The scale on the axis of abscissas is logarithmic, and the ordinates are pulse counts. Chicago, February 1964.

registering instrument.

The dependence of  $\sigma_{B_i}^2$  on  $\Delta T$  was computed to verify these considerations.

Data for the city of Chicago (February 1964) were analyzed. The statistical fluctuations make an appreciable contribution only for small  $\Delta T = 1, 2$ , and 6 hours (Fig. 1); at  $\Delta T = 12$  hours, the statistical and instrumental factors are of approximately equal influence, but beginning with  $\Delta T = 1$  day, the instrumental factor begins to exert the decisive influence on system noise level. This indicates that as  $\Delta T$  increases, it becomes possible to detect increasingly weaker drifts of the null level over a time interval equal to  $\Delta T$  or a multiple thereof. The steepness with which the  $\sigma_{B_i}^2 = f(\Delta T)$  curve descends depends to a consider-

/106

able degree on the quality of instrument performance. Thus, for stations less reliable than that of Chicago, we should expect the asymptote to which the  $\sigma_{B_i}^2 = f(\log \Delta T)$  curve tends to be higher

on the axis of ordinates. The minimum and maximum noise levels can vary with time even at the same station.

For the SA CRS, therefore, it is necessary to provide for acquisition of a family of  $\sigma_{B_i}^2 = f(\Delta T)$  curves that will deter-

mine station resolution. In this case, the range of possible  $\Delta T$  values will vary from  $\Delta T = 15$  min (the basic registration range of the CRS) to  $\Delta T = 1$  day. There is no point in making the calculations for intervals longer than a day, since the null level of a CRS is constant with an accuracy no better than 0.1%.

## REFERENCES

1. Blokh, Ya.L. and Pimenov, I.A. A Standard Algorithm for Testing Constancy of Registration Level at Cosmic-Ray Stations. *Geomagnetizm i aeronomiya*, 1967, No. 5, 7.
2. Blokh, Ya.L. and Pimenov, I.A. A Standard Algorithm for Cosmic-Ray Stations. *Geomagnetizm i aeronomiya*, 1969, No. 1, 9.



RESULTS OF MEASUREMENT OF RADIO-WAVE  
ABSORPTION IN THE IONOSPHERE BY THE  
AI METHOD

/107

N.A. Korinevskaya

**ABSTRACT:** The results of absorption measurements at 2.2 MHz in 1964-1967 are examined. The instruments are described. Median noon absorption values for each month from 1964 through 1967, the diurnal variations of absorption on the Regular World Days (RWD's), and the seasonal variations of absorption and  $\cos \chi$  are given. The dependence of the absorption coefficient on sun spot number is analyzed.

During the period of the IGY and IQSY, the absorption of radio waves in the ionosphere was investigated at a broad network of stations under the unified international program [1-3]. New data that enable us to begin study of the geographic distribution of absorption were obtained. Studies of absorption during the years of the solar activity minimum are of particular interest.

Apparatus. Program of observations. The absorption of radio waves in the ionosphere (AI method) was measured from 1955 through 1962 at two frequencies:  $2.2 \pm 0.2$  and  $3.0 \pm 0.2$  MHz. The reflected-pulse amplitudes were registered visually [4].

Radio-wave absorption was not measured at Alma-Ata from 1962 through 1964, since improved apparatus had been installed. An SP-3 ionospheric sounder with a special OG-1-11 oscillograph was prepared for photographic registration of reflected-signal amplitudes. The pulse powers of the SP-3 transmitter, which range up to 20 kW, are regulated with a five-position selector. Pulse duration is 100  $\mu$ sec. Pulse repetition rate is 30 Hz. The receiver has a sensitivity of 10  $\mu$ V with a 2:1 signal-to-noise ratio and a passband of 30 kHz.

The receiver for absorption measurements has a linear amplitude response over a broad voltage range (up to 12 mV at its input with 70-dB attenuation). The transmitting antenna is rhombic, and the receiving antenna is a wide-band horizontal dipole. Pulse amplitudes are monitored visually with a K-2 display. Two gated echo signals go from the station output to the differential input of the OG-1-11 oscillograph. The reflections of the first and

second echo signals appear on either side of the centerline on the oscillograph screen and are registered on film (width 35 mm) moving at a speed of 20 mm/min. Time markers are automatically placed at one-minute intervals by an electronic flash tripped by the ionospheric sounder's program clock.

/108

On 1 January 1964, measurements of radio absorption were resumed under the international program at  $2.2 \pm 0.2$  MHz [3]. A second auxiliary frequency was selected in the band from 3.2 to 4.8 MHz as a function of the state of the ionosphere, with the proviso that it be separated by 10% from the critical frequency of any layer. Stratification in the E- and F-regions and low critical frequencies during the night, when the calibration constant of the instrument was determined, made it difficult to select the second frequency. Radio-wave absorption was measured three times a day at each frequency:

1. Two 15-minute sessions around noon (11:30-11:45 and 12:30-12:45 local solar time).

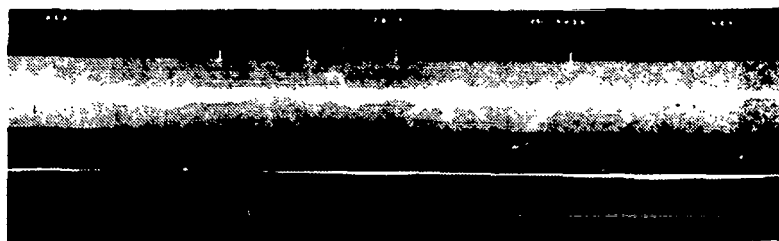


Figure 1. Specimen Photographic Record of the Amplitudes of Signals Reflected from the Ionosphere.

2. One 30-minute session at night, when double reflections occur, for determination of the instrument's calibration constant. Measurements were made in the 3.2-4.8-MHz frequency band in 1964-1965.

The oscillograph was calibrated with a GSS-6 with external modulation from a pulse generator. Two gated pulses delivered from the receiver output with different input voltages and receiver gains were photographed on moving film. A calibration curve expressing the amplitude of the signal on the OG-1-11 oscillograph (in mm) as a function of receiver input voltage (in  $\mu$ V) was then plotted. The coefficient K was calculated from the calibration curves for the different gains with transmission bandwidth held constant, for use in determining the average amplitude of the signal over each measurement session (Fig. 1).

Calculation of radio wave absorption coefficient. The absorption coefficient L (in dB) for vertical incidence is

determined by the formulas

$$L = -20 \lg \rho; \quad (1)$$

$$L = 20 \lg \frac{A_{1n} K h_n}{\rho} - 20 \lg A_{1d} K h_d'; \quad (2)$$

$$\rho \rho_e = \frac{E_1 h_1}{E_0 h_0}, \quad (3)$$

$$E_1 = A_1 K; \quad (4)$$

$$E_2 = A_2 K, \quad (5)$$

where  $A_{1n}$  is the average amplitude of the first reflection at night, in mm;  $A_{1d}$  is the average amplitude of the first reflection during the day, in mm;  $A_2$  is the amplitude of the second reflection in mm;  $\rho$  is the coefficient of reflection from the ionosphere;  $\rho_e$  is the coefficient of reflection from the earth;  $h'$  is the effective height of the reflecting layer at the particular frequency;  $\rho_e$  is assumed equal to unity.

All measurements were reduced to a height  $h = 100$  km by using the expression  $20 \log(h_n'/100)$ . The quantity

$$G_0 = 20 \lg \frac{A_{1n} K}{\rho} + 20 \lg \frac{h_n'}{100} \quad (6)$$

characterizes the unabsorbed energy of the radio wave and is the calibration constant of the equipment. During the day, when there are no multiple reflections, absorption is calculated by Formula (2) from the first-multiplicity reflected signal with consideration of the instrumental constant. The average amplitude of the signal on the film is determined with an electromechanical integrating device designed to average the ordinates of the curves and suggested by Engineer A.A. Starovarov.

Determination of instrument calibration constant. The instrumental constant  $G_0$  (unabsorbed field strength) is determined from the nighttime echo-signal-registration sessions, when absorption is very weak and multiple reflections from the F- and E-layers of the ionosphere are observed.

Methodological difficulties arise in determining the instrumental constant  $G_0$ . There are two methods of calculating the calibration constant (6). In the first, it is determined from the amplitude of the first reflection at night. It is assumed that absorption is very weak at night. In the second method, it is

necessary to determine the amplitudes of the first and second reflections and compute the coefficient of reflection from the ionosphere in order to calculate the instrument's calibration constant. As we know, the coefficient of reflection from the earth may vary over a broad range from 0.99 (sea water) to 0.5 (dry ground), depending on soil conductivity [8]. The coefficient of reflection from the earth is assumed equal to unity in both the first and second calculation methods. This assumption introduces an error in determination of the calibration constant, especially in localities where soil conductivity varies widely and the relief is broken [10].

In 1964, only reflections from the nighttime F-layer were used to determine  $G_0$ , and sessions during which reflections from the sporadic E-layer appeared on the ionospheric records were not considered in the calculation. The largest numbers of sessions with multiple reflections from the F-layer are observed in September through March. During the summer, multiple reflections from the F-layer are rarer owing to screening by the sporadic E-layer. In virtue of the large number of night sessions, we were able to determine the instrumental constant separately for each month. June 1964 was an exception; in that month, there were very few sessions with multiple reflections from the F-layer that were suitable for calculation, and we were not yet taking reflections from the sporadic E-layer into account. The average value of the instrumental calibration constant  $G_0$  over the month was calculated by linear averaging, i.e., the quantity  $G_0 = \frac{A_1 K h}{p}$  was averaged for the individual measurements before converting it to decibels, and then the height correction  $20 \log(h/100)$  was added to it. With a sufficiently large number of measurements, linear and decibel averagings of  $G_0$  differ by no more than 1-1.5 dB.

TABLE 1

Month	I		II	
	Number of measurements	$G_0$	Number of measurements	$G_0$
January	49	90,4	31	89,6
February	72	90,0	33	89,2
March	28	90,2	18	90,4
Total	149	90,2	82	89,7

In study of radio-wave absorption in the ionosphere, an interesting problem is that of the influence of a semitransparent sporadic E-layer on the value of the instrumental constant [9]. In this case, we may expect a decrease in the instrumental constant because some of the energy of the radio waves is reflected from the E-layer and does not reach the F-layer [8]. During January-March 1964, many reflections from a semitransparent sporadic E-layer were registered at night. This enabled us to compute the instrumental constant for two different sets of conditions.

First, all night sessions with reflections from the F-layer in the presence of an  $E_s$ -layer were taken into account in computing the instrumental constant  $G_0$  (Table 1).

/111

Then we computed  $G_0$  from reflections from the F-layer with exclusion of the sessions in which reflection from the semitransparent sporadic E-layer was observed.

As Table 1 shows, the semitransparent sporadic E-layer actually has no influence on the instrument's calibration constant.

In determining the calibration constant, it is necessary to consider the state of the ionosphere. A diffuse ionosphere causes scattering of the radio wave's energy on inhomogeneities and a decrease in the coefficient of reflection

$\rho = \frac{2E_2}{E_1}$  from the ionosphere. As a result, the instrumental con-

stant  $G_0 = 20 \lg \frac{E_1 h}{\rho}$  is on the high side if determined under these conditions [9].

The experimental curve (Fig. 2) is approximated quite closely by the Rayleigh probability density distribution of random variables (dashed curve).

Results of measurement of radio absorption at  $2.2 \pm 0.2$  MHz. In absorption measurements, it is desirable to select the lowest possible frequencies in order to minimize the error introduced by the extraordinary wave. The selected frequencies must not be close to the critical frequency of the region for any length of time. In accordance with these requirements, a frequency of 2.2 MHz was selected for the basic measurements by international agreement [1, 3].

On analyzing the variation of the noon values of the absorption coefficient  $L$  (Fig. 3), we note that absorption varied sharply during January in 1964 and 1965. The absorption increase from 10 through 15 and from 25 through 27 January 1964 was accompanied by a marked rise in the minimum reflection frequency on the ionospheric records. In 1965, absorption was unusually strong from 5 through 10 January and from 28 through 31 December, and in 1966 from 19 through 23 January. This is an example of the winter absorption anomaly, which has been observed on many occasions at

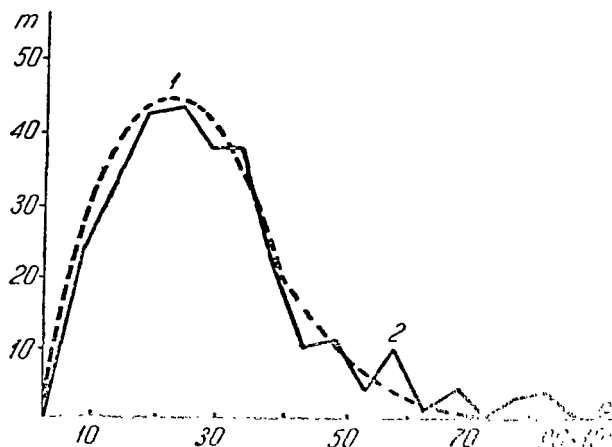


Figure 2. Rayleigh Probability Density of Random Variables (1); Calibration Constant at 2.2-MHz Frequency (2).

/114



Figure 3. Variation of Daily Noon Value of Absorption Coefficient. a) 1964; b) 1965; c) 1966; d) 1967.

TABLE 2

Month	Year																										
	1958		1959		1961		1962		1964		1965		1966		1967												
	L	σ	L	σ	L	σ	L	σ	L	σ	L	σ	L	σ	L	σ											
January	50	4.0	4.0	58	6.5	10.7	28	7.5	13.5	50	27	8.2	12.8	3.6	28	7.5	10.6	3.1	26	6.0	4.9	5.2	6.1	6.9	3.5		
February	47	6.3	7.3	45	5.2	5.2	38	4.0	4.0	48	24	4.3	4.0	3.2	25	5.1	3.4	5.9	26	4.6	3.0	4.6	5.2	3.8	5.3		
March	50	1.9	4.9	48	4.7	11.8	38	3	5	3.5	40	28	5.9	6.1	3.9	25	4.3	3.7	4.1	27	6.2	7.2	3.1	5.5	4.8	3.7	
April	56	4.7	6.7	59	6.7	8	44	4	4	4.4	41	31	6.7	4.6	6.4	30	3.3	1.1	2.7	29	4.5	4.0	3.9	4.8	3.8	3.5	
May	49	5.0	11.3	61	4.9	8.2	46	3	4	3.4	48	34	5.9	4.7	3.8	34	4.4	3.5	3.7	33	5.0	3.9	4.4	5.5	4.0	5.5	
June	51	3.8	10.8	60	3.9	9.5	50	2	9	2.9		40	4.9	3.4	4.2	36	3.6	3.4	2.7	35	6.9	5.7	5.8	6.0	5.2	4.4	
July	53	2.3	9.1	55	4.9	8.3	49	4	3	6.1		34	4.3	4.3	3.1	34	3.9	4.2	2.6	43	4	8.4	1	5.1	5.4	3.4	
August	53	3.3	11.0	57	7.2	11.1	49	2	8	2.8		32	4.7	3.6	4.8	34	4.4	3.3	4.7	36	4.0	4.4	2.7				
September	48	3.9	7.5	49	7.5	10.3	48	4	1	4.1		32	5.1	3.5	4.5	28	4.0	1.8	5.4	37	5.3	4.7	4.8				
October	50	5.6	5.6	43	5.7	5.7	47	3	4	3.4		27	6	6	5.2	6.6	23	4.4	3.0	4.6	28	5.0	4.9	4.0			
November	45	5.2	6.5	41	8.6	8.6	45	4	8	4		21	4.2	3.6	2.5	18	4.0	3.7	3.4	25	4.7	3.7	4.0				
December	46	5.2	8.8	46	6.2	9.5	49	3	8	3.8		22	5.0	5.5	3.3	19	5.5	5.8	2.7	28	6.2	5.8	4.9				
Average	50	4.4	7.8	52	6.0	8.9	45	4	1	4.6	45	29	5.5	5.1	4.1	27.8	4.5	4.1	3.8	31.0	5.3	4.7	4.4				

Note.  $\pm \Delta L = \frac{\Sigma L - L_{\text{med}}}{n}$  is the deviation from the median for a quiet ionosphere;  $\sigma_1$  is the root-mean-square deviation with consideration of disturbed days.

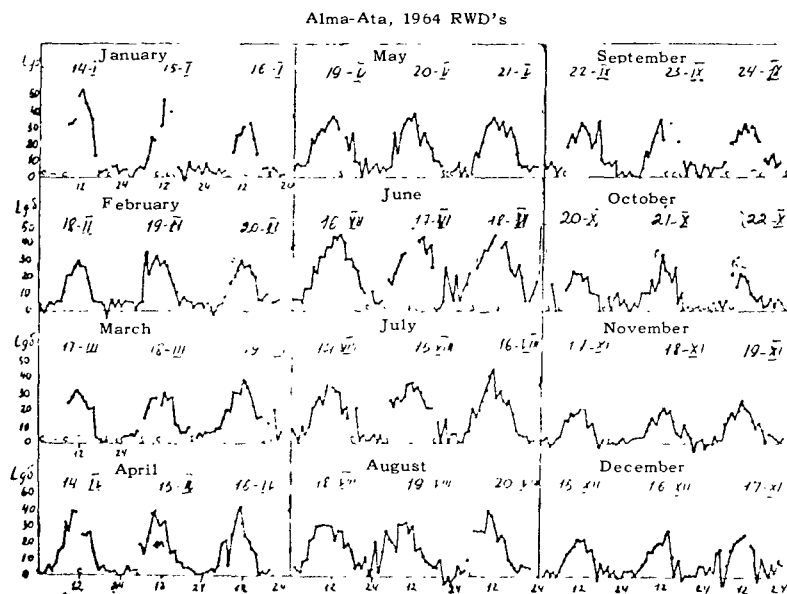
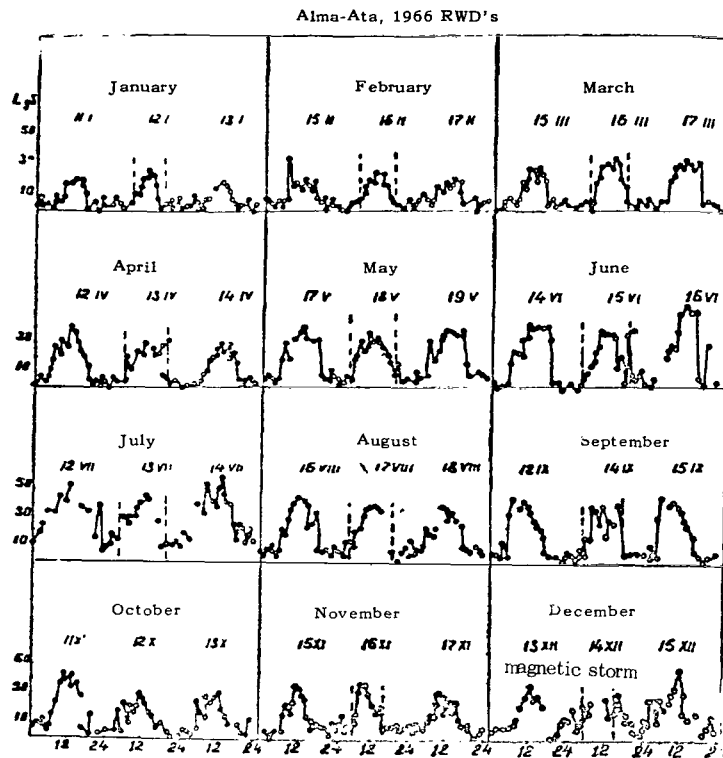


Figure 4. Absorption on RWD. ●) Cases of reflection from sporadic E-layer; the dashed lines are times of sunrise and sunset.



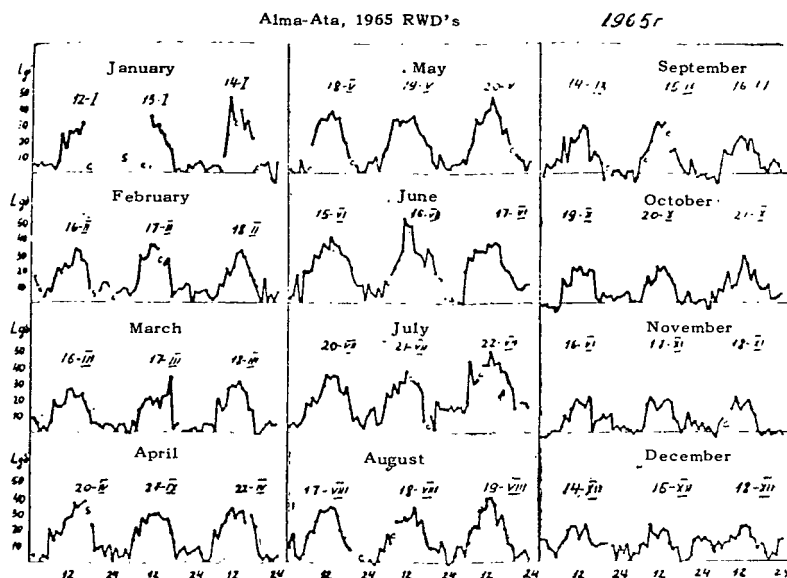


Figure 4, Cont'd.

other stations in latitudes from 30 to 60° and in both the northern and southern hemispheres. The increased absorption associated with the winter anomaly usually persists for about two to five days in a row at various times during the month. The winter anomaly is assumed to be due to a rise in the temperature of the lower ionosphere [11, 12]. The strongest absorption during the winter anomaly was registered in the year of the solar activity minimum (1964); then, as solar activity increases, the winter absorption fluctuations become smaller.

In January 1964 (Fig. 4), the RWD's coincided with the days of the winter absorption anomaly. The strongest absorption ( $L = 53$  dB) was observed on 14 January; absorption then decreased gradually to  $L = 19$  dB on 17 January. In the diurnal absorption curves, there were occasionally (19 February, etc.) sharp increases during the morning and evening hours due to the proximity of the working frequency to the critical frequency of the E-layer. During the night, absorption fluctuates in the range from 0 to 10 dB; in certain cases, we note negative absorption-coefficient values (in February 1964 and September 1965), possibly as a result of focusing (Table 2, Fig. 5). At Alma-Ata, the weakest absorption is usually observed in February and November, and the strongest during the summer. Table 2 gives median noon absorption values ( $L$ , dB) and the root-mean-square deviation ( $\sigma$ ).

/117

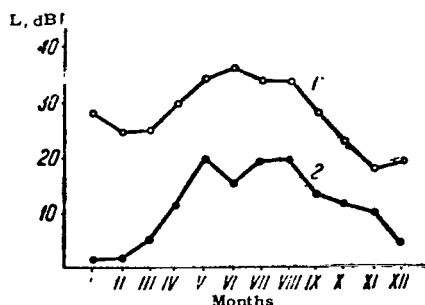


Figure 5. Seasonal Variation of Noon Absorption for 1964-1967. 1) At 2.2 MHz; 2) at 4.5 MHz during 1965.

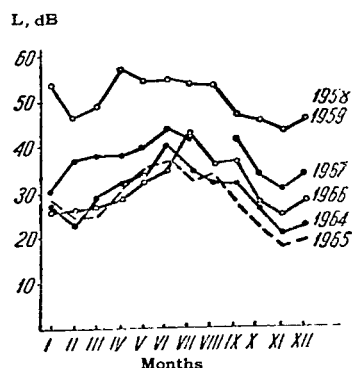


Figure 6. Seasonal Variation of Absorption at Alma-Ata During Years of Sunspot Maximum (1964-1967).

Absorption was traced as a function of solar activity on the basis of the Alma-Ata absorption data for 1958 and 1959 and partial data for 1960-1967 (Figs. 6 and 7).

Absorption begins to increase during the latter half of 1966; during February and March of 1967, it was above normal owing to a sharp increase in the number of sunspots.

Absorption can be expressed by the following formula as a function of sunspot number for Alma-Ata:

$$L = L(1 + aW).$$

where  $a = 0.0026$  and  $W$  is the relative sunspot number. During years of maximum and minimum solar activity, however, a certain correction must be introduced into this formula, since it has been observed that the fall and rise of solar activity do not immediately reduce and increase absorption. There is a shift of approximately one year between sunspot number and absorption. Indeed, absorption was no weaker in 1959 than in 1958, and even somewhat stronger; in 1965, it did not exceed the 1964 level. The relationship is similar for other stations.

/118

Diurnal variation of absorption and the zenith angle of the sun. It is known from single-layer theory that the ionospheric absorption of radio waves  $L \sim (\cos \chi)^{3/2}$ . The results of the radio-wave absorption measurements do not confirm this law, and it has generally been found that  $L \sim (\cos \chi)^n$ , where  $n < 3/2$ . Consequently, most of the absorption occurs in a region that lies lower than the E-layer and is not subject to the single-layer laws. The numerical values obtained by various authors for the

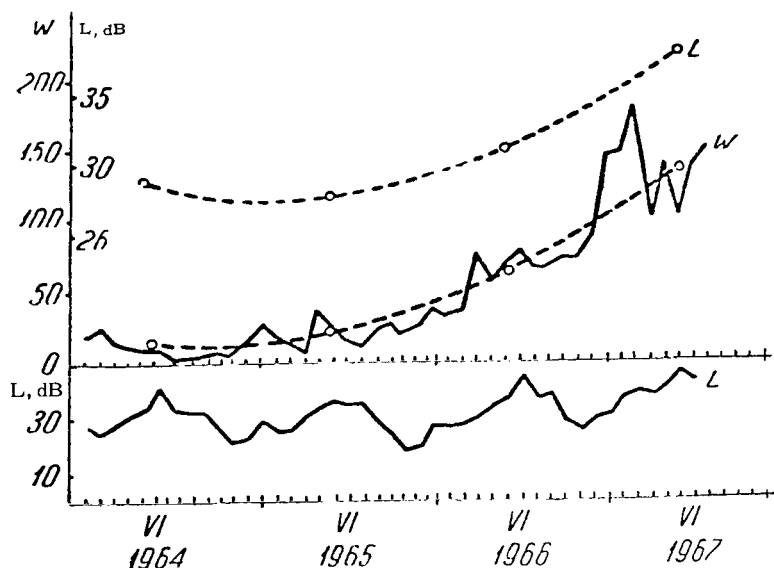


Figure 7. Variation of Monthly Average and Annual Average Sunspot-Number Values (Middle Curve), Variation of Annual Average Values of Absorption at 2.2 MHz (Upper Curve), and Seasonal Variation of Monthly Median Absorption Values (Lower Curve) from January 1964 Through July 1967.

exponent  $\bar{n}$  vary widely, averaging 0.5-0.7. We determined the exponent  $\bar{n}$  from absorption data measured round-the-clock on the RWD's in each month of 1964, 1965, and 1966. For this purpose, we plotted  $1 + \log \kappa$  as a function of  $1 + \log \cos \kappa$ , where  $\kappa = -\ln \rho$ , determining  $\bar{n}$  from the slopes of lines found by the method of least squares (Table 3, Fig. 8).

Seasonal variation of absorption and  $\cos \kappa$ . It is known that the radio absorption measured at middle-latitude stations at a constant zenith angle fluctuates through a small range about a certain average level during the year, except for the winter months, when the absorption anomaly is observed [11]. We calculated the absorption on the RWD's in 1964 for a zenith angle  $\kappa = 70^\circ$ . It was found that the absorption at  $\kappa = 70^\circ$  is about 20 dB, except for January, when  $L = 35$  dB. In January 1964, the RWD's coincided with those of anomalous winter absorption. To establish the relation between the seasonal variation of absorption and solar zenith angle, we plotted  $1 + \log \kappa$  as a function of  $1 + \log \cos \kappa$  for each month in 1964. The data for January were excluded from the calculation, and the method of least squares was used to find the straight line  $y = 0.61x + 1$  (Fig. 8).

/119

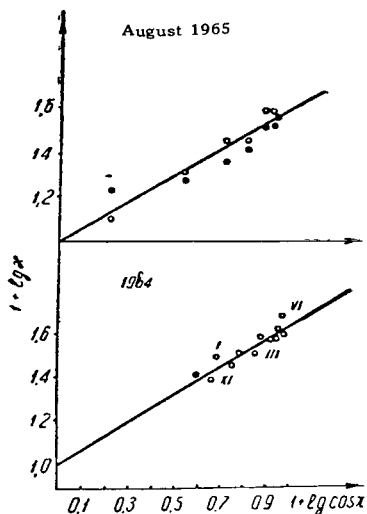


Figure 8. Relation Between Seasonal Variation of Absorption and the Zenith Angle of the Sun.

TABLE 3. VALUES OF THE EXPONENT  $\underline{n}$  FOR  $(\cos \chi)^{\underline{n}}$

Month	Year			Three-year average
	1964	1965	1966	
January	0.79	0.41	0.68	0.63
February	0.65	0.30	0.19	0.38
March	0.64	0.57	0.35	0.52
April	0.92	0.56	0.60	0.69
May	0.53	0.60	0.43	0.52
June	0.56	0.44	0.20	0.40
July	0.56	0.35	0.31	0.41
August	0.52	0.55	0.43	0.50
September	0.71	1.11	0.96	0.93
October	0.73	1.24	0.60	0.86
November	0.48	0.24	0.24	0.32
December	0.59	0.48	0.23	0.43
	0.64	0.57	0.435	0.55

The value obtained for the exponent,  $\underline{n} = 0.61$ , agrees closely with the  $\underline{n} = 0.62$  calculated from the diurnal absorption

/120

curves on the RWD's in 1964. The exponent  $\underline{n}$  shows a seasonal variation, averaging (over three years) 0.55 (Fig. 9). The largest values of  $\underline{n}$  are observed in the spring and autumn, and the smallest in summer. The 1964 increase in  $\underline{n}$  is associated with a winter absorption anomaly, since the January 1964 RWD's coincided with several days of enhanced absorption.

To judge from the data of Table 3, the height of the basic (nondeviative) absorption region varies over the course of the year [13]. The authors of [13] obtained a height curve of the exponent  $\underline{n}$  by assigning specific model height distributions to the recombination coefficient  $\alpha$  in the lower ionosphere. It was found that  $\underline{n} = 3/2$  for an absorbing layer above 90 km. The exponent  $\underline{n}$  will decrease with increasing absorbing-layer height and, consequently, with increasing recombination coefficient  $\alpha$ .

We compared the data on the height dependence of  $\underline{n}$  in [13] with the results of our calculations (Table 3) and made tentative estimates of absorbing-region height. We found that in the spring and fall, when  $\underline{n}$  increases, the absorbing region is situated at a height of 70-80 km, and that in summer it descends to 60-70 km. During the anomalous absorption on the RWD's of January 1964,  $\underline{n}$  equalled 0.79. It can be assumed with [13] as a base and considering our own data that the basic absorption during the winter anomaly takes place at heights of 70-80 km, i.e., that the absorbing layer is higher at this time than on ordinary days.

/121

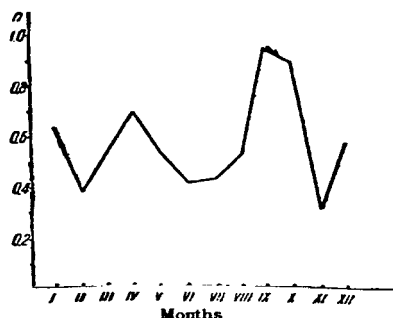


Figure 9. Seasonal Variation of  $n$  According to Data in Table 3.

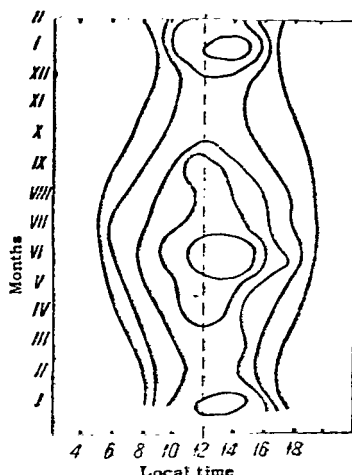


Figure 10. Isolines of  $\kappa = -\ln p$  for 1964 at Frequency of 2.2 MHz on the RWD's.

Shift of maximum in diurnal absorption variation. A shift of the maximum away from local noon has been observed on several occasions in analysis of the diurnal absorption curve [9]. The absorption maximum usually lags 20-40 minutes behind noon (Fig. 10). To analyze this effect in greater detail, it will be necessary to have the diurnal variation for the entire month, and not only for the three RWD's.

## CONCLUSIONS

1. The variation of the absorption frequencies was studied at 2.2 MHz at noon on each day and round-the-clock on the 1964-1967 RWD's.

2. The existence of the winter absorption anomaly at the latitude of Alma-Ata was confirmed. The winter anomaly was most pronounced during the year of the solar activity minimum (1964).

3. The widest absorption fluctuations are observed in winter. /122 The fluctuation had its smallest annual average value in 1965 (as compared with 1964 and 1966).

4. It was shown that the exponent  $n$  in the formula  $L \sim \cos \chi^n$ , as calculated for the RWD's, has a seasonal variation with maxima in the spring and fall. The hypothesis that the absorbing-region height is at 70-80 km in the spring and fall and descends to 60-70 km in summer is advanced [13]. Absorption can be expressed as follows as a function of sunspot numbers for 1965-1967:

$$L=L_0(1+aW),$$

where  $a = 0.0026$ .

A shift between  $L$  and  $W$  is noted during the years of maximum and minimum solar activity. Absorption lags behind solar activity by approximately a year.

## REFERENCES

1. Instruction Manual, 1956, No. 5. The Ionosphere, Vol. II, Publ. Comm. of CSAGI, London.
2. Gorbushina, G.N. Instruktsiya po izmereniyu pogloshcheniya radiovoln v ionosfere (Instructions for Measurement of Radio Absorption in the Ionosphere), Leningrad, AANII (Arctic and Antarctic Scientific Research Institute), 1959.
3. Instruction Manual, 1963, No. 4. The Ionosphere, Part 11, CJG-IQSY Committee, London.
4. Zachateyskaya, Ye.N. Results of Absorption Measurement at Alma-Ata. In: "Ionosfernyye issledovaniya" (Ionospheric Research), 1964, No. 13, 97.
5. Korinevskaya, N.A. and Molostov, G.F. Use of the SP-3 Ionospheric Station for Measurement of Radio Absorption. In: "Rezultaty nablyudeniya i issledovaniya v period MGSS" (Results of Observations and Research During the IQSY), No. 2, Moscow, "Nauka," 1966.
6. Taubenheim, J. Incoherency of Pulse Echoes and the Measurement of Ionospheric Absorption. J. Atmos. and Terr. Phys., 1960, 18, 147.
7. Svechnikov, A.M. Influence of the Sporadic E-Layer on Radio Absorption in the F2-Layer. In: "Ionosfernyye issledovaniya," 1964, No. 13, 85.
8. Umlauf, G. Some Ionospheric Results Obtained During the International Geophysical Year. Proc. of a Symposium at Brussels, 1960.
9. Al'pert, Ya.L. Rasprostraneniye radiovoln i ionosfera (Propagation of Radio Waves and the Ionosphere). Moscow, Izd-vo AN SSSR, 1960.
10. Zelenkova, I.A. and Zelenkov, V.Ye. Notes on Technique for Measurement of Radio-Wave Absorption in the Ionosphere Under Broken-Terrain Conditions. "Geomagnetizm i aeronomiya," 1968, No. 5, Vol. 8.
11. Raspredeleniye elektronnoy kontsentratsii v ionosfere i ekzosfere (Distribution of Electron Concentration in the Ionosphere and Exosphere). (Edited by K.I. Gringauz). Moscow, "Mir," 1964.
12. Sechrist, C.F. A Theory of the Winter Absorption Anomaly at Middle Latitudes, J. Atmos. and Terr. Phys., 1967, 29, 113.
13. Mitra, A.P. and Jain, V.C. Interpretation of the Observed Zenith Angle Dependence of Ionospheric Absorption, Journ. Geophys. Research, 1963, No. 9, 68, 1267.

VARIATIONS OF COSMIC RAYS ASSOCIATED WITH  
CHROMOSPHERIC FLARES ON THE SUN

/123

I.D. Kozin

ABSTRACT: Features of the cosmic-ray variations in the region of the geomagnetic pole and a smooth decrease in the intensity of cosmic rays as a result of increased solar activity are reported. A 66-day variation of the cosmic rays was registered, in agreement with the maximum frequency and power of solar chromospheric flares.

The Antarctic interior station "Vostok" is located in the immediate vicinity of the earth's South Geomagnetic Pole.

Data on the variations of cosmic rays obtained at the geomagnetic pole are of enormous interest: they make it possible to analyze the variations of the solar cosmic rays during periods of rising solar activity.

The cosmic-ray variations at a geomagnetic pole have singular features. First of all the primary radiation arriving at the pole is rich in low-energy particles, which are deflected from their original trajectory by the earth's magnetic field to form an observable latitude effect and compose a substantial component of the total flux. Cosmic-ray intensity reaches its maxima at the geomagnetic poles, and since the principal source generating the low-energy cosmic-ray protons is the sun, the phenomena of plasma ejection and corpuscular streams from its surface are most clearly in evidence at the geomagnetic poles.

It is known [1] that the cosmic-ray intensity decreases with increasing solar activity, and that the magnitude and frequency of the Forbush fall-offs at the solar activity minimum are largest at the geomagnetic poles [2]. The year 1966 is regarded as a period of solar-activity increase in its initial stage.

Over a seven-month interval, the intensity of the cosmic-ray neutron component dropped 7-8% (Fig. 1) as a result of the incipient solar-activity increase. The general negative correlation trend is beyond question. The effects of solar-activity variations appear in the cosmic-ray variations after a lag of 2-3 days; this is fully consistent with the propagation velocity of the solar corpuscular streams [3]. But how shall we explain the

/124

decrease in the registered cosmic-ray background intensity with rising solar activity? The current view is that the electromagnetic properties of the sun-earth space are changed by the increasing solar-wind flux as solar activity rises, with an increase in the resistance to penetration of galactic cosmic rays to the earth.

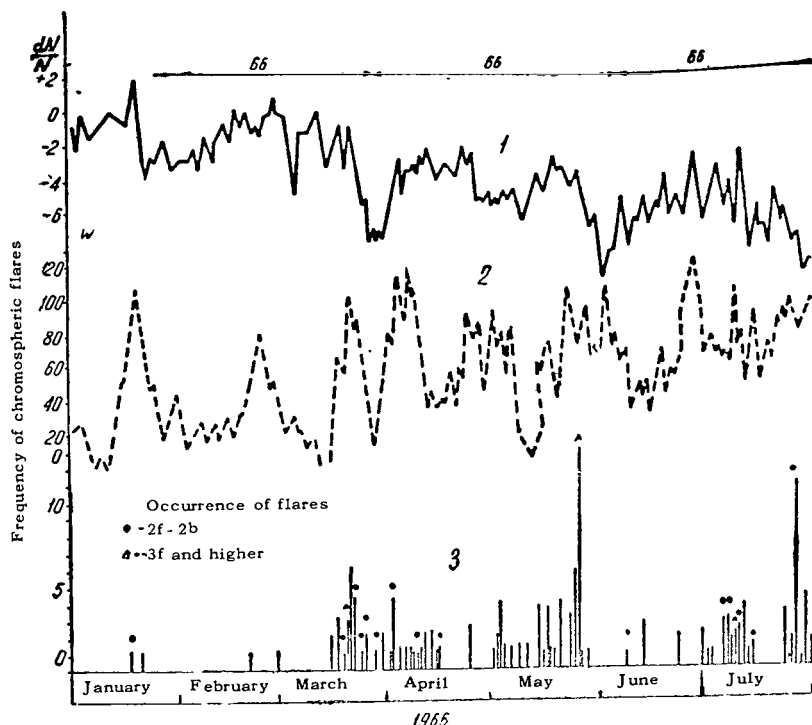


Figure 1. 1) Relative daily average intensities of cosmic-ray neutron component with correction  $\delta N/N$  introduced for the barometric effect; 2) solar activity in Wolf numbers  $W$ ; 3) frequency and power of chromospheric flares.

Conditions for optimum deceleration of the low-energy cosmic-ray component, which yields its energy to ionization of the lower inosphere, are created in the earth's atmosphere, and the effect of lowered registered-particle intensity is enhanced. This effect will be considered in greater detail in [4].

/125

The opinion has been advanced [5] that the general cosmic-radiation intensity background decreases during times of increased solar activity as a result of incomplete intensity recovery after the Forbush effects. It can be stated on the basis of "Vostok" data that the intensity decreases smoothly, and that although incomplete intensity recovery is observed after Forbush effects, it is more probably a result of addition of the smooth-decrease and



Forbush-effect phenomena. If the smooth intensity decrease is extrapolated with a moving average to a Forbush-type decrease, excluding the period of the Forbush decrease, the extension of the extrapolated line coincides with the unrecovered intensity after the Forbush effect. The diagram given in this paper is interesting in that the cosmic-ray intensity has a periodic variation with Forbush effects at the beginning and end of a 66-day period.

Obviously, the very small volume of experimental material makes it impossible to exclude an accidental origin for this variation. The analysis will be continued.

To ascertain the causes of this anomalous variation (Fig. 1), we have introduced a curve of the frequency and power of chromospheric flares on the sun. The diagram shows clearly that the flare maxima during this time occurred in the same intervals, and that the most powerful flares (2f-2b and higher) occur during the same periods. The literature had as yet made no reference to registration of a 66-day cosmic-ray variation, although periods of 21 to 23 days had been mentioned more than once [6, 7, 8]. The diagram (Fig. 1) of the chromospheric flares and the cosmic-ray neutron-component variations shows no distinct cycle with a 22-day period, but the appearance of the 66-day variation could be linked precisely during this time with surges in the power and numbers of chromospheric flares during every third 22-day period of the sun's rotation. If we assume that the power and numbers of chromospheric flares increase every 66 days and that the sun's period of rotation during this time was approximately 22 days, we might expect 22-day cosmic-ray variations with extreme values occurring every third period. If, on the other hand, the sun's period of rotation is 27 days, there will be departures from the 66-day variation. At this time, we observe a 66-day variation of the cosmic rays and the same sequence of chromospheric-flare maxima. /126

## CONCLUSIONS

1. The geomagnetic pole is a convenient station for observations of solar cosmic ray variations.
2. A 66-day variation of the cosmic rays has been detected; it requires confirmation and improvement on the basis of larger amounts of statistical material.
3. A distinct Forbush decrease in the intensity of cosmic rays is observed at the geomagnetic pole with increasing number and power of the solar chromospheric flares.

## REFERENCES

1. Dorman, L.I. Variatsii kosmicheskikh luchey i issledovaniye kosmosa (Variations of the Cosmic Rays and Space Research), Moscow, Izd-vo AN SSSR, 1963.
2. Dorman, L.I. Variatsii kosmicheskikh luchey (Variations of the Cosmic Rays), Moscow, Gostekhizdat, 1957.
3. Dorman, L.I. On the Nature of the Cosmic-Ray Intensity Variation During Magnetic Storms. Trudy Mezhdunarodnoy konferentsii po kosmicheskim lucham (Transactions of the International Conference on Cosmic Rays), Vol. IV, 1960.
4. Kozin, I.D. Variatsii kosmicheskikh luchey vo vremya pogloshcheniya tipa "PCA" (Cosmic-Ray Variations During "PCA"-Type Absorption), this collection, page 74.
5. Lockwood, J. Phys. Rev. 1958, 112, 1750.
6. Dorman, L.I. and Shatashvili, L.Kh. In: "Kosmicheskiye luchy" (Cosmic Rays), No. 7, Moscow, Izd-vo AN SSSR, 1965.
7. Dorman, L.I. and Shatashvili, L.Kh. In: "Kosmicheskiye luchy," No. 5, Moscow, 1963, page 88.
8. Dorman, L.I. and Shatashvili, L.Kh. In: "Kosmicheskiye luchy," No. 4, Moscow, Izd-vo AN SSSR, 1961, page 179.

Translated for the National Aeronautics and Space Administration by  
Scripta Technica, Inc. NASW-2036.



040 001 C1 U 13 720317 S00903DS  
DEPT OF THE AIR FORCE  
AF WEAPONS LAB (AFSC)  
TECH LIBRARY/WLOL/  
ATTN: E LOU BOWMAN, CHIEF  
KIRTLAND AFB NM 87117

POSTMASTER: If Undeliverable (Section 158  
Postal Manual) Do Not Return

*"The aeronautical and space activities of the United States shall be conducted so as to contribute . . . to the expansion of human knowledge of phenomena in the atmosphere and space. The Administration shall provide for the widest practicable and appropriate dissemination of information concerning its activities and the results thereof."*

— NATIONAL AERONAUTICS AND SPACE ACT OF 1958

## NASA SCIENTIFIC AND TECHNICAL PUBLICATIONS

**TECHNICAL REPORTS:** Scientific and technical information considered important, complete, and a lasting contribution to existing knowledge.

**TECHNICAL NOTES:** Information less broad in scope but nevertheless of importance as a contribution to existing knowledge.

**TECHNICAL MEMORANDUMS:** Information receiving limited distribution because of preliminary data, security classification, or other reasons.

**CONTRACTOR REPORTS:** Scientific and technical information generated under a NASA contract or grant and considered an important contribution to existing knowledge.

**TECHNICAL TRANSLATIONS:** Information published in a foreign language considered to merit NASA distribution in English.

**SPECIAL PUBLICATIONS:** Information derived from or of value to NASA activities. Publications include conference proceedings, monographs, data compilations, handbooks, sourcebooks, and special bibliographies.

**TECHNOLOGY UTILIZATION PUBLICATIONS:** Information on technology used by NASA that may be of particular interest in commercial and other non-aerospace applications. Publications include Tech Briefs, Technology Utilization Reports and Technology Surveys.

*Details on the availability of these publications may be obtained from:*

**SCIENTIFIC AND TECHNICAL INFORMATION OFFICE**

**NATIONAL AERONAUTICS AND SPACE ADMINISTRATION**

**Washington, D.C. 20546**